Progress in Materials Science 103 (2019) 425–483

Contents lists available at ScienceDirect

Progress in Materials Science

journal homepage: www.elsevier.com/locate/pmatsci

Structural architectures with toughening mechanisms in Nature: A review of the materials science of Type-I collagenous materials

Wen Yang[a,b,c,*], Marc A. Meyers[b,d], Robert O. Ritchie[c,e,*]

[a] Department of Materials, ETH Zurich, 8093 Zurich, Switzerland
[b] Materials Science and Engineering Program, University of California San Diego, La Jolla, CA 92093, USA
[c] Lawrence Berkeley National Laboratory, Berkeley, CA 94720, USA
[d] Department of Nanoengineering, University of California San Diego, La Jolla, CA 92093, USA
[e] Department of Materials Science and Engineering, University of California Berkeley, CA 94720, USA

ARTICLE INFO

Keywords:
Collagen
Bone
Toughness mechanisms
Biological
Bioinspired
Biomedical application

ABSTRACT

The structural constituents of tissues in organisms are composed primarily of minerals and proteins. Collagen is the most common protein used to construct such natural materials in vertebrates; among these structures, a wide variety of hierarchical architectures with structural and property gradients have evolved to induce desired combinations of stiffness, strength, ductility and toughness for a diverse range of mechanical functionalities. The soft collagen provides biological materials the ability to resist tensile tractions and to dissipate energy under mechanical deformation. Here we seek to understand the structure, deformation and toughening mechanisms of collagenous materials from the perspective of the hierarchical assembly of individual collagen molecules, fibrils, fibers, as well as the other nature-designed hierarchical structural elements. This review summarizes the structural designs of collagenous materials focusing on Type-I collagen, the most abundant extracellular protein that forms linear arrays, as well as examining its deformation and toughening mechanisms by illustrating how nature uses hierarchical structures and gradients, at nano-, micro- to macro-levels, to confer different functions to its organisms. The organization of collagen is discussed for different structures in order to illustrate the broad range of its functional and mechanical properties: specifically, skin, arteries, eye cornea, fish scales, bone, ligaments and tendons. We conclude by highlighting important developments in tissue engineering where synthetic and natural collagen has been incorporated into the architecture of the body. We trust that such insight may provide guidance for the design of the next-generation of synthetic structural materials with unprecedented functionality.

1. Introduction

Collagen plays a key structural role in biological materials. It is ubiquitous in natural organisms and the most common protein found in vertebrates, where it performs important structural functions. The etymology of collagen is, from the Greek: *kola* (glue) + *gen* (giving birth to). Collagen is, figuratively, the glue that holds the organisms together. However, its origin comes from the fact that glue was in the past made with boiled hides. For a broad description of collagen, the reader is referred to the excellent book edited by Fratzl and entitled, appropriately, *Collagen: Structure and Mechanics*.

* Corresponding authors at: University of California, San Diego, USA (W. Yang). Department of Materials Science and Engineering, University of California Berkeley, CA 94720, USA (R.O. Ritchie).
E-mail addresses: wyang8207@gmail.com, wey005@eng.ucsd.edu (W. Yang), roritchie@lbl.gov (R.O. Ritchie).

https://doi.org/10.1016/j.pmatsci.2019.01.002
Received 13 May 2018; Received in revised form 8 January 2019; Accepted 8 January 2019
Available online 10 January 2019
0079-6425/

Approximately 25–35% of the proteins (which account for 15–17% of their weight) are collagen, the principal structural material in the human body together with hydroxyapatite (7% by weight). Depending on the structural function and location in the organism, collagen can take a number of configurations (~28) and is classified into Types I, II, III… until XXVIII. Collagen can be divided into fibrillar (forming fibers) and non-fibrillar. The former are Types I, II, III, V, XI, XXIV and XXVII while the latter include a number of these:

- FACIT (Fibril Associated Collagen with Interrupted Triple Helices): Types IX, XII, XIV, XIX, XXI. Collagenous domains are interrupted by non-collagenous domains.
- Basement membrane collagen: Type IV. It forms under the cavities of the epithelium lining and the surface of organs (skin, *etc.*) and the endothelium in the interior of blood vessels. They are composed of thin sheets (40–50 nm thick) which play a role in molecular filtration.
- MACIT (Membrane Associated Collagen with Interrupted Triple Helices) Types XIII, XVII.
- Transmembrane collagens. Type IV. They span cell surfaces, hair, placenta.
- Type V: Cell surfaces, placenta.

Although there are approximately twenty-eight different types of collagen, Type I collagen is by far the most common and important structurally, being present in skin, tendons and ligaments, veins and arteries, organs, and bone. With its long molecules, it is particularly important as it provides the basis for the tensile strength and toughness of many biological materials. Indeed, Type I collagen is one of the principal structural elements of numerous natural materials including skin [1–4], tendon [5,6], cartilage [7,8], bone [9–11], and fish scales [12–14]. It has been nicknamed “the steel of biological materials” because of its ubiquity and versatility. As we will show, the mechanisms by which collagen can induce specific mechanical properties are many and varied. In some biological materials, it is as simple as purely organic collagen with other proteins in the matrix forming as curved fibers which, on unravelling, straightening and sliding apart enable the creation of large strains; in other materials, it is the collagen combining with inorganic phases architected at different levels to form various complex hierarchical structures that can provide specific mechanical property functions to the organisms, such as the formation of tough subsurface regions beneath hard surface layers to protect against external penetration.

1.1. Hierarchical structure and the network of the collagen fibrillar system

Collagen is a nano- to micro-scale hierarchical structural material. Fig. 1.1 illustrates the hierarchical structure of a typical straight Type I collagen fiber with and without mineral. The left hand of the figure shows an overview of the hierarchy in the structure with its length-scales. On the right hand, details are provided to illustrate the information on non-mineralized and mineralized collagen fibers at these different levels. Type I collagen is a fibrous protein composed of two α_1 and one α_2 peptide chains; each chain has a repetitive amino acid sequence [19,20] shown at the lower middle of Fig. 1.1. The principal amino acids in Type I collagen are glycine, proline and alanine. The long amino acid sequence allows three polypeptide chains with possible hydrogen bonds (H-bonds) as connections to form a triple helical structure, called tropocollagen or collagen molecule, with three domains including $-NH_2$ non-triple-helix terminal (N-terminal), triple-helix, and $-COOH$ non-triple-helix terminal (C-terminal) [18,20]. The molecules are ~300 nm long with a diameter of 1.5 nm and can self-assemble into collagen fibrils (diameter ~100 nm) with an overlap of 27 nm and a gap space of 40 nm; in this way, a characteristic *d*-spacing of 67 nm is formed (Fig. 1.1). This assembly is enabled by a peculiar head-to tail bonding of molecules. Inorganic phases can also take part in this generation process; in particular, nanoscale hydroxyapatite (HAP) crystals, (shown at the lower right in Fig. 1.1) with typical dimensions of 50 × 25 × 3 nm (shown by the transmission electron micrograph in Fig. 1.1), can fill the gap regions between the mineralized collagen fibrils. In bone, the HAP crystals also form in an intra- and inter-fibrillar pattern, as discussed in Section 2.2. To continue this hierarchical building process, several thousand (~4000) collagen fibrils can twist or pack together to form a collagen fiber. The scanning electron micrograph in Fig. 1.1 (right upper image) depicts a typical collagen fiber with the atomic force micrograph below showing the surface morphology of the collagen fibrils with their distinct 67 nm *d*-spacing.

The staggered arrangement of collagen molecules shown in Fig. 1.1 is only feasible in a plane. In three-dimensional space, the collagen molecules have to form a different configuration to maximize their bonding. This is the microfibril which contains five collagen molecules and is known as quarter staggering. The microfibril has a diameter of ~3.5–4 nm. Fig. 1.2b provides a better view using the electron density map of a collagen microfibril. The five individual molecules are not aligned with the axis of the microfibril but form a right-handed helicoid [23]. It was also found that the microfibrils interdigitate in an ordered fashion. The atomistic model and analysis developed by Gautieri et al., [21] is shown in Fig. 1.2a. In the cross-sectional view (Fig. 1.2a), five molecules are marked. The sequence helps to explain the formation of the *d*-spacing. Fig. 1.2a also shows a base molecule in red and four adjoining molecules with different staggers, which form one microfibril. The characteristic *d*-spacing of collagen appears in the way that the microfibrils are assembled (Fig. 1.2).

According to Alexander et al., [22], the interdigitation of microfibrils may explain the presence of continuous gap channels in the fibril structure, formed by an alignment of gap spaces in the neighboring microfibrils. This interdigitation may also explain why it has not been possible to separate the microfibrils, in contrast to the fibrils that are clearly bonded more tightly and form spaghetti-like structures with ample sliding between them. Fig. 1.2c shows a tri-dimensional sketch of a microfibril. The five molecules are marked 0, 1.4, 1/2, ¾ and 1, indicating the quarter stagger (300/67 = ~4.5). We believe that the helical arrangement accommodates the difference.

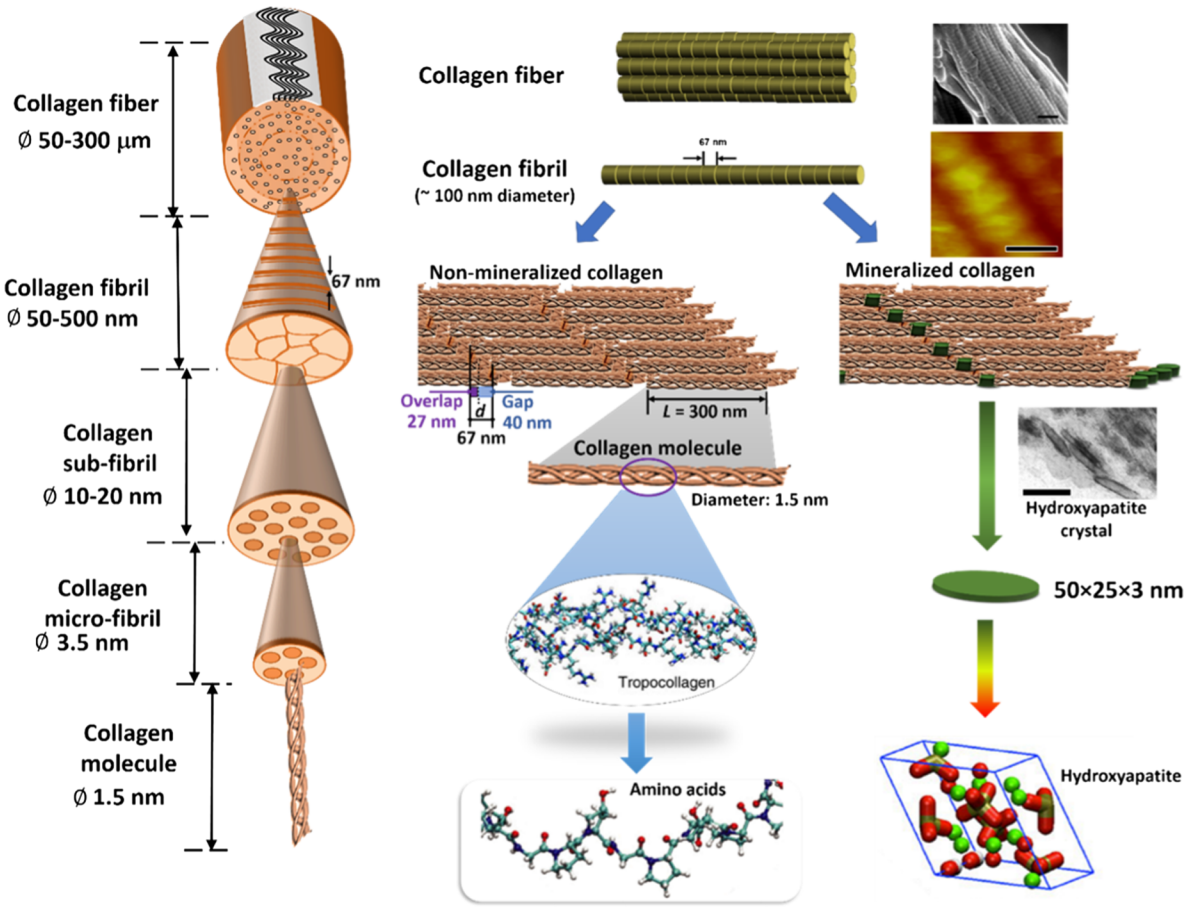

Fig. 1.1. Hierarchical structure of a collagen fiber. The left-hand side shows the hierarchy of the collagen fiber with length-scales. On the right-hand side, a more detailed illustration at each level of hierarchy is explained. In the Figure, SEM image of a collagen fiber (scale bar: 500 nm), AFM image of a collagen fibril (scale bar: 100 nm), and TEM image of hydroxyapatite (scale bar: 50 nm) is taken from Refs. [14–16], respectively; the sequence level in nanoscale of tropocollagen and hydroxyapatite is taken from Ref. [17], and the picture of amino acids is taken from Ref. [18]. For mineralized collagen, in addition to the volume in the gaps, there is a considerable amount of mineral between parallel collagen fibrils, *e.g.*, bone comprises some 40–70 wt% hydroxyapatite (HAP).

The deposition of the inorganic phase within the collagen fibril is apparent from the cryo transmission electron microscopy (TEM) image in Fig. 1.3 [24], which shows mineralized collagen fibrils with bands, labeled a-e, of the repetitive *d*-spacing in the structure of each collagen fibril. After the mineralization procedure, amorphous calcium phosphate surrounds and enters the collagen fibril along the a-bands (Fig. 1.3a–c) which span both the overlap and gap regions (Fig. 1.3d–f) at the C-terminal of the collagen fibril. Analysis of the cryo-TEM images indicates that the mineral crystals are distributed evenly between the gap and overlap regions with a preference for the *d*-band in gap region. However, the gap region corresponds to only 40/300 (gap zone/collagen molecule length) = 0.13 of the overall volume, and therefore in more highly mineralized bone crystals (and amorphous), HAP has to deposit intra-and inter-fibrillarly. The mineral phase deposited within the collagen fibrils significantly enhances the stiffness of collagenous materials and further provides for compressive strength; the mineral is also exceedingly brittle but does not degrade the toughness of the bone because its nanoscale size makes it essentially insensitive to fracture [25,26]. The entire collagenous structure is held together by interfibrillar proteoglycan connections which comprise either chondroitin or dermochondan sulphate bridges (Fig. 1.4a); specific links between the collagen fibrils are shown in Fig. 1.4b [27].

1.2. Mechanical behavior of nonmineralized/mineralized collagen at nano- and micro-scales

1.2.1. Triple helical tropocollagen molecules

The deformation of a single collagen molecule involves molecular stretching and unwinding due first by entropic and then by energetic mechanisms including the breaking of hydrogen bonds. Based on the structure of collagen, computational modeling [18,21] predicts that the fundamental deformation mechanisms in individual collagen molecules involve molecular stretching with concomitant breaking of H-bonds. Fig. 1.5 shows the tensile force-strain curve, up to 40% strain, for an individual collagen molecule indicating the number of H-bonds involved while being stretched. During the initial stages of deformation, the number of the H-bonds

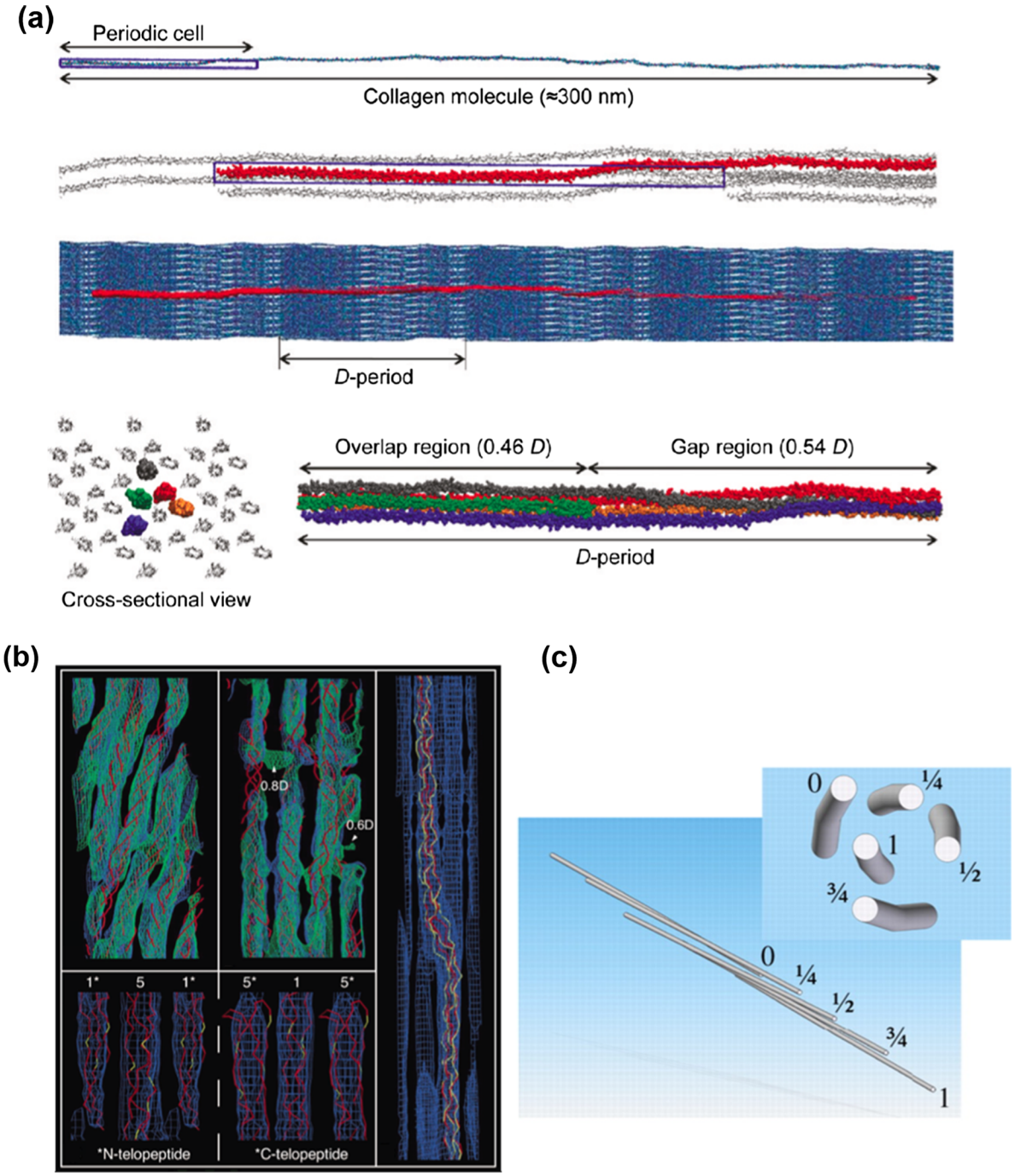

Fig. 1.2. Structural arrangement of the collagen microfibril. (a) Atomistic model of the collagen microfibril [21]. (b) Electron density maps showing the molecular structure and its packing arrangement. Note that the first two maps (in green) have been compressed five times along the direction parallel to the *x*-axis for clarity. (c) Microfibril shown in lateral view and in top-bottom view (insert). The five collagen molecules are staggered as indicated: 0, ¼, ½, ¾, 1 [22].

remains around 30, with the collagen molecule rotating so that it does not carry much load and the strains are limited to less than ~10%; subsequently, the collagen molecules tend to straighten with H-bond breakage, until at 25% strain, the number of the H-bonds involved is reduced by roughly a half. Beyond this point, the backbone of the molecule stretches and no additional H-bonds break. The breaking of the H-bonds enables intermolecular sliding of the collagen chains which provides the basis for large permanent strains to be accommodated in the collagen without catastrophic failure [28].

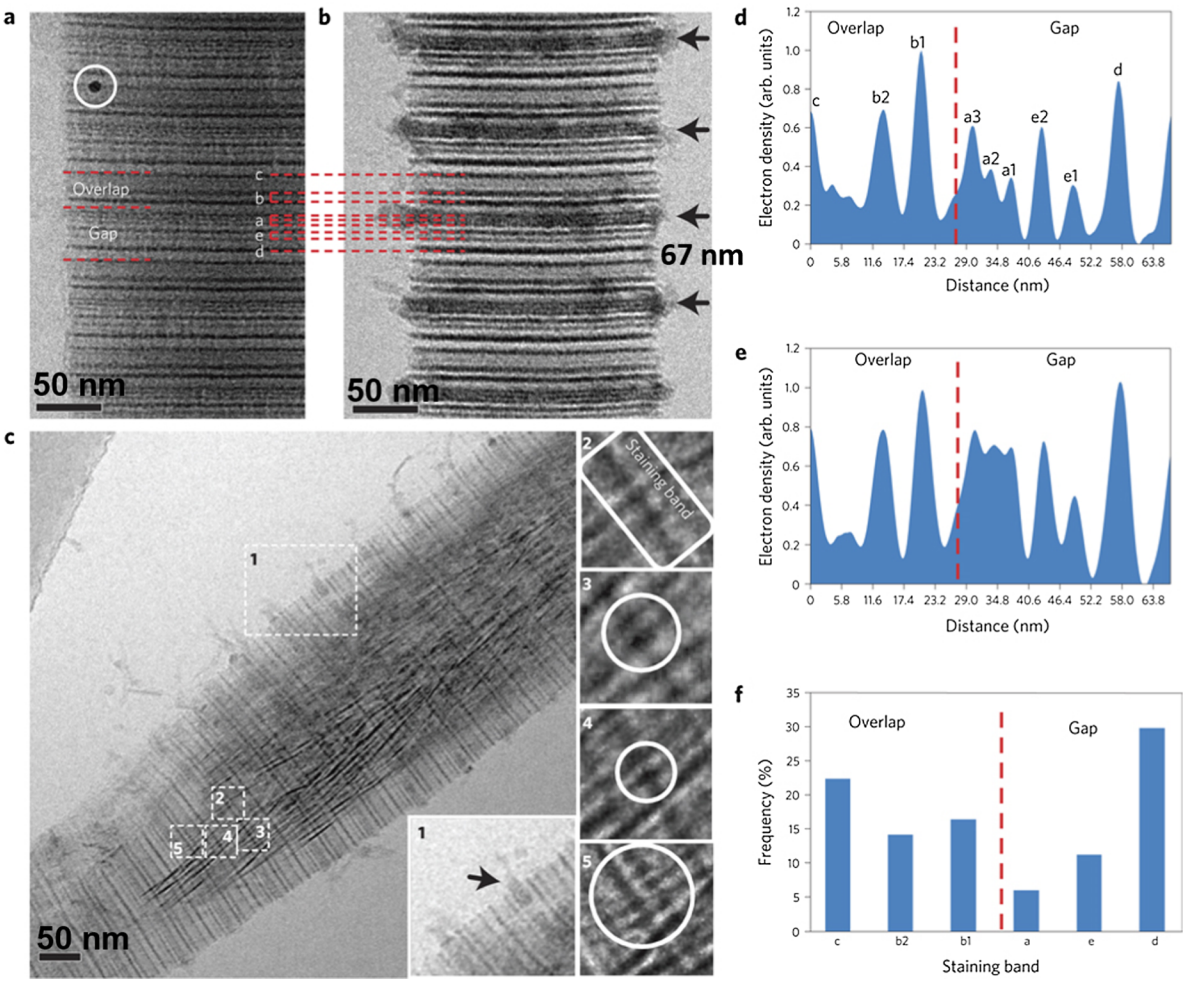

Fig. 1.3. Comparison by cryo-TEM of non-mineralized and mineralized collagen [24]. (a) Cryo-TEM of stained, non-mineralized collagen fibril, overlap (27 nm) and gap (40 nm) regions are shown (b) Cryo-TEM of stained mineralized collagen. The arrows show the stained bands, typical a-, b-, c-, d-, e-bands are labeled in (a) and (b), (c) Cryo-TEM of stained mineralized collagen. Apatite crystals penetrate into fibril structure (a-bands) shown by arrow in inset 1, and can nucleate on bands (insets 2 and 3). (d) and (e) Variation of mineralized and non-mineralized collagen (a) and (b); (f) number of crystals nucleating per band. Dashed vertical lines in (d), (e) and (f) represent the boundary between gap and overlap zones.

1.2.2. Non-mineralized collagen fibrils

Several researchers have modeled the mechanical behavior of the non-mineralized collagen (under generally tensile loading) using hyperelastic macroscopic models based on strain energy, mathematical fits, as well as structurally and physically-based observations; these have been summarized in the review by Sherman et al. [29]. The structural models and deformation of single collagen molecules include containing rigid corner models (in-plane zig-zag shaped beams with fixed apexes of infinite rigidity [30,31], sinusoidal models containing the elastic components of matrix fiber interactions [32,33], helical models assuming fiber inextensibility and leading to an infinite stiffness at full extension [34,35], sequential loading models which only consider the stiffness on the fully strengthened fibers [36], and a recent circular model assuming that fibrils are circular segments of various radii and degrees of curvature based on direct observations of collagen under load [4]. Additionally, the viscoelasticity in the collagen structures (*e.g.*, using Maxwell, Kelvin and Standard models) has been considered by Meyers and Chen [37] to model the sliding between collagen fibrils, *i.e.*, the fibrillar sliding which, for example, is a prime mechanism of inelasticity in bone.

Additionally, it is of note that several experimental studies have been conducted on single collagen fibrils. Fig. 1.6a shows the stress-strain curve of collagen fibrils determined using atomic force microscopy (AFM). The fibril was glued at its ends onto a glass surface and to the tip of AFM cantilever. Using this procedure, collagen fibrils immersed in phosphate-buffered saline (PBS) solution were stretched by the AFM cantilever vertically at various strain rates [38,41]; the results indicated that the elastic modulus of the fibril can be increased by ~30% for two orders of magnitude increase in strain rate. These properties are also extremely sensitive to the presence of a moist environment with the modulus increasing from 0.2–0.5 GPa to 5 ± 2 GPa when the PBS solution was removed [42]. This increase in stiffness with dehydration is also evident at the structural level. As described in Section 4.1, this has an impact at the macroscale on collagenous materials such as skin; specifically, dehydrated skin has a mechanical response that is

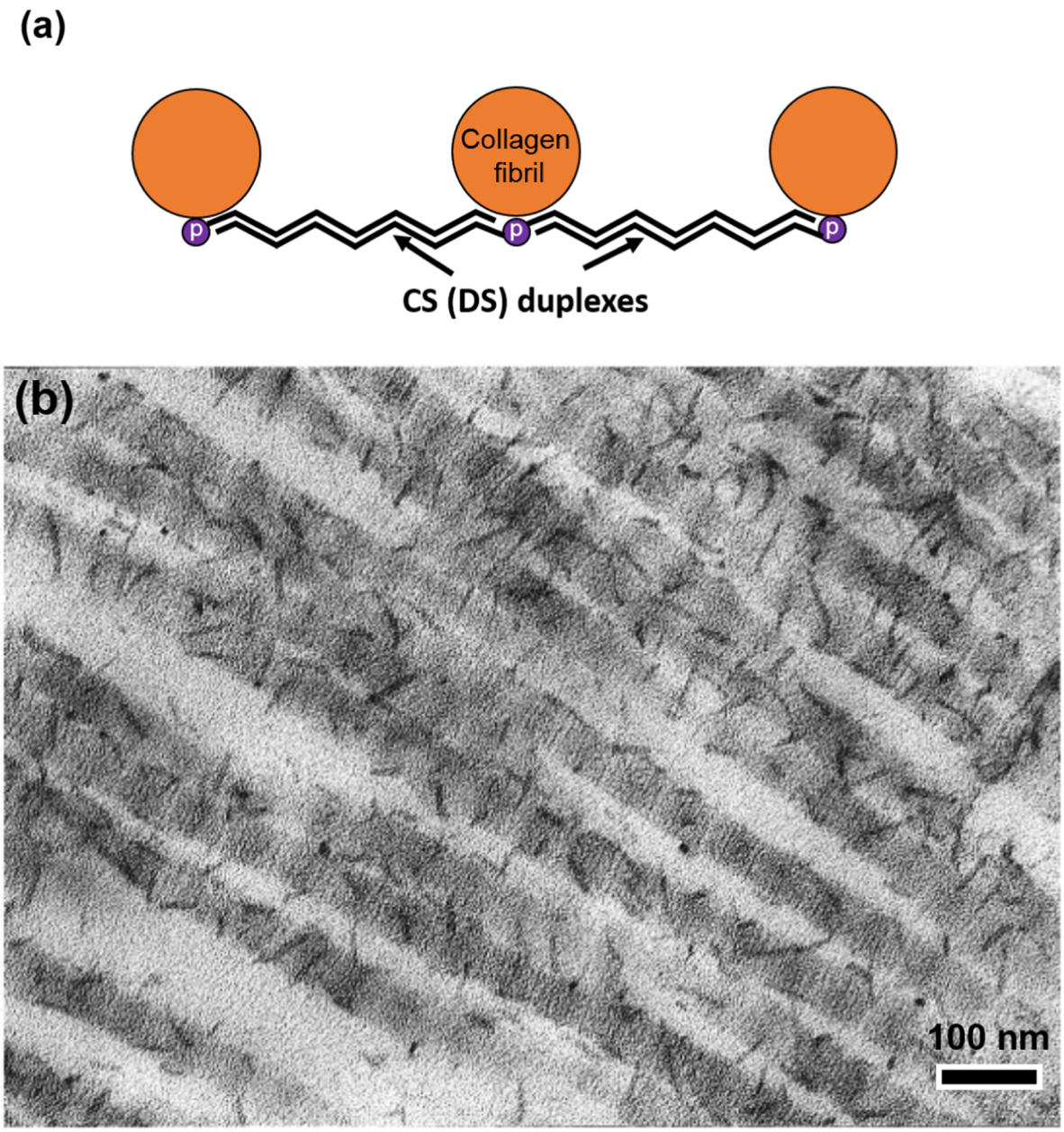

Fig. 1.4. Interfibrillar proteoglycan bridges in ECM of collagen [27]. (a) Structure of the interfibrillar bridges composed of proteoglycans (PG) → AGAG⇔AGAG ← protein ((p) in the figure) ← PG; chondroitin or dermochondan sulphates (CS or DS) form the bridges and links between collagen fibrils. (b) Collagen fibrils and the interfibrillar bridges of the rabbit corneal stroma appeared after treatment with glutaraldehyde and 0.1 M NaOH. (a) was reproduced from Ref. [27].

dramatically different from that of hydrated skin.

The tensile behavior of hydrated single collagen fibrils has also been examined by Eppell et al. [39] who isolated single fibrils from a sea cucumber using micro-electro-mechanical (MEMS) testing. As shown in Fig. 1.6b–d, fibrils A and B, with respective gauge lengths of 20 and 5 μm, were seen to display a similar secant elastic modulus (400–500 MPa) at the beginning and start to increase to ~930 MPa, although due to its shorter gauge length, fibril B achieved almost a factor of two larger strain with considerable stiffening at the strain of 0.3. When these single collagen fibrils were loaded cyclically, their modulus decreased after a large number of cycles (~300–30,000 cycles); after 5 mins of cyclic loading (at ~7% of strain) at increasing frequencies, the modulus of the collagen fibrils was reduced somewhat but remained at 550–590 MPa [39].

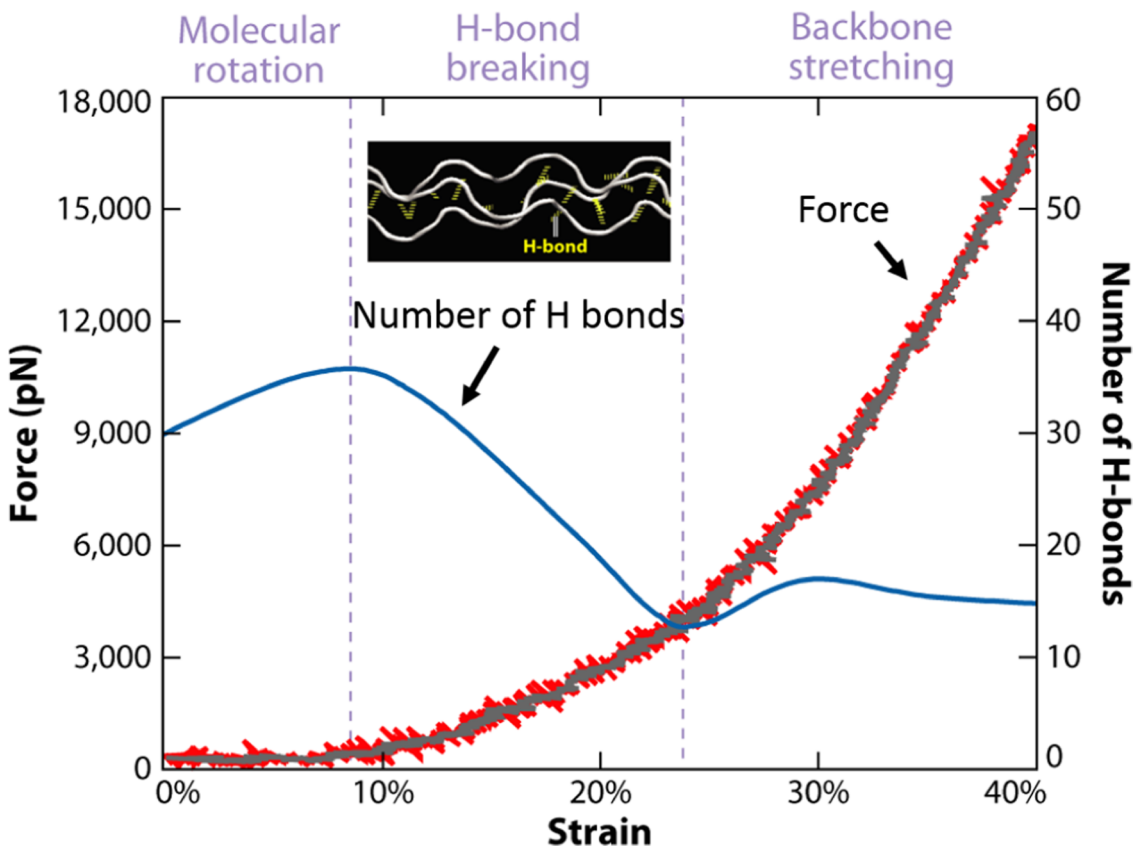

Fig. 1.5. Mechanical behavior of the tropocollagen molecule modeled by molecular dynamics [21,28]. In the first stage of deformation (strain < 0.1), the tropocollagen straightens; the number of H-bonds remains constant at ~ 30, corresponding to approximately one H-bond for each amino acid triplet. In the second stage, tropocollagen is straightened and H-bonds gradually break (up to a strain ~ 0.25). In the third stage, the number of H bonds remains constant at ~ 15. The backbone is stretched with no additional H-bond breakage.

1.2.3. Mineralized collagen fibrils

The mechanical properties of collagen fibrils are markedly changed by the presence of mineral crystals; indeed, Nair et al., [17] indicated how the mineral content (0–40%) can affect the mechanical behavior of collagen fibrils using *in silico* models. This is shown in Fig. 1.7a and b which illustrates the distribution of hydroxyproline along the collagen fibril axis; the data show that the maximum amount of HAP mineral is found in the gap region between 30 and 50 nm, consistent with the experimental studies of Nudelman et al. [24] (illustrated in Section 1.1). Stress-strain and modulus-strain curves (Fig. 1.7d and e) confirm that the presence of such mineral enhances both the strength and stiffness of a collagen fibril at a specific strain, although the characteristic J-shape of the stress-strain curve becomes less evident with higher mineral content. Buehler [43] explained these differences between non-mineralized and mineralized collagen fibrils using a combined molecular dynamics simulation and theoretical analysis (Fig. 1.8). Specifically, the HAP crystals naturally play a pivotal role in developing high strength and stiffness in mineralized collagen fibrils, which are nevertheless still able to sustain large degrees of deformation. Without the mineral, plastic deformation in pure collagen fibrils starts at very low ($\sim 5\%$) strains and shows continuous softening after $\sim 7\%$ strain. In contrast, mineralized collagen fibrils display $\sim 25\%$ higher stiffness, $\sim 30\%$ higher yield strength with minimal softening delayed to a much higher ($\sim 45\%$) strain (Fig. 1.8a). In images from the model (Fig. 1.8b and c), fibrillary yielding is characterized by intermolecular slip. Without the mineral present, slip initiates between tropocollagen molecules with lower material density (red circle in Fig. 1.8b), and further reduces the density as it leads to the formation of nanoscale voids which eventually result in final failure. With the mineral present, however, slip initiates at the interface between the hydroxyapatite particles and tropocollagen molecules, which enables a large regime of dissipative deformation after the onset of yielding; moreover, a large stress can be maintained due to additional resistance to slip at the interface between mineral and tropocollagen molecules. It should be mentioned that the collagen-HAP composite is structured at the nanometer scale, consistent with the high tensile strength observed.

1.2.4. Collagen fibers

A collagen fiber may contain dozens or hundreds of collagen fibrils with hydrogen bonds. The presence of water molecules may contribute to the sliding between the collagen fibrils in a collagen fiber. The relevant mechanisms include sliding, bond breaking and bond reformation result in an increase of the strain within the collagen fiber. Consistent with this sliding hypothesis, Fig. 1.9a shows

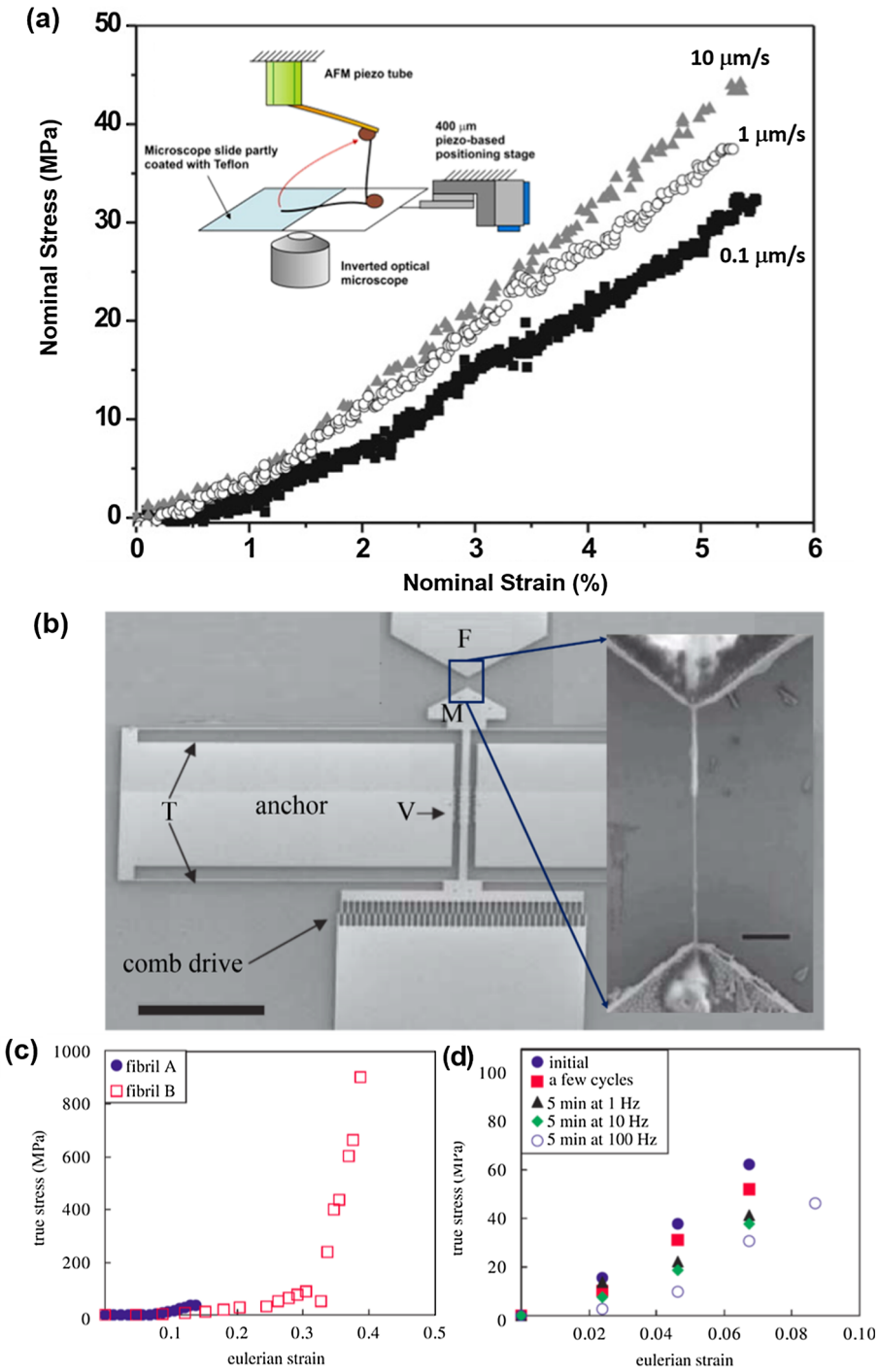

Fig. 1.6. Mechanical response of collagen fibrils (a) in phosphate buffered saline solution measured using atomic force microscopy (adapted and modified from Yang et al., [38]), (b–d) using a MEMS testing machine [39,40]. (a) The picture on the upper left represents the experimental setup. Epoxy was glued on the two ends of the collagen fibrils. A 400-μm piezo-based positioning stage connected to the sample holder was used to generate large strains in the fibril. Considerable strain-rate sensitivity was observed; (b) MEMS mechanical testing platform with the enlarged collagen fibril picture set in the platform, (c) Calculated stress-strain curves using SEM images from two different angles to determine cross sectional dimensions; gauge lengths of fibrils A and B are 5 μm and 20 μm, respectively. (d) Stress–strain curve of a fibril measured before and after cycling at frequencies given in the plot. Stiffness was found to decrease with cyclic loading. Measured moduli were: 0.93 GPa (initial), 0.78 GPa (few cycles), 0.59 GPa (5 min at 1 Hz), 0.55 GPa (5 min at 10 Hz), and 0.55 GPa (5 min at 100 Hz).

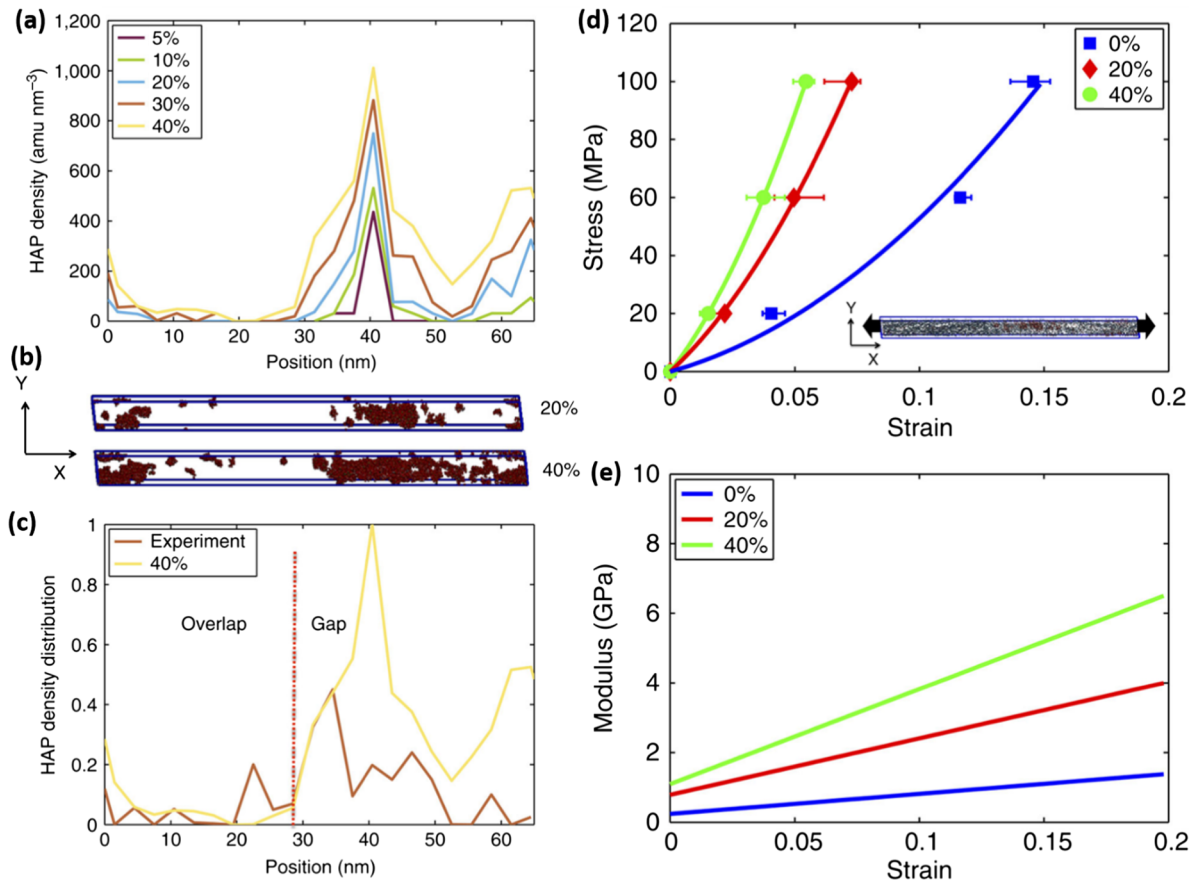

Fig. 1.7. Mineral distribution in the collagen fibrils and their mechanical behavior [17]. (a) Variation in HAP along the collagen fibril axis. Most HAP is located in the gap region (between 30 and 50 nm). (b) Spatial distribution of the HAP along the gap + overlap regions for 20 and 40% mineral density. (c) Normalized HAP density distribution along the fibril axis for the 40% case and comparison with experimental results from Nudelman et al. [24], confirming that the maximum deposition is indeed in the gap region. (d) Stress-strain plots for a non-mineralized collagen fibril (0%), 20% and 40% mineral-density; inserted picture is the fibril unit cell with mineral content, with the error bars in (b) computed from the maximum and minimum values of the periodic box length along the *x*-direction at equilibrium, (e) Elastic modulus *vs.* strain for 0, 20 and 40% mineral density; the modulus can be seen to increase with mineral content.

the experimental stress-strain curve for a collagen fiber as compared to that for a single collagen molecule and a collagen fibril [5,44]. The curve for the fiber shows a more pronounced J-shape curve which is indicative of significant sliding between collagen fibrils; this provides the fiber with a higher strain and energy dissipation when pulled in tension. Tendon is a good example of an organ consisting of collagen fibers. Rigozzi et al. [40] examined the change in *d*-spacing in tendon using atomic force microscopy (AFM) and found that the length of the *d*-spacing increased, whereas its variability decreased, with increasing total strain. It has become accepted that during the simple stretching of collagen fibers, several active mechanisms participate including sliding between fibrils at the micro-level, stretching of individual collagen molecules and fibrils, sliding between collagen molecules with associated breaking of H-bonds, and possible bridging from the nano-scale links between collagen fibrils (Fig. 1.5).

2. Structural architecture of collagenous materials

Collagen fibers organize themselves into different hierarchical structures according to their specific functions. In this review, we use several examples, namely arteries, cornea and stroma, skin, tendon, bone and fish scales, which display different structures as well as varying degrees of mineralization, to illustrate the toughening mechanisms and functions of these biological collagenous materials.

2.1. Arteries

Arteries and veins are the most important cardiovascular system in the body. Arteries, carrying oxygenated nutrient-rich blood from the lungs to the confines of the body, with veins returning the depleted (venous) blood, comprise the circulatory system. This circulatory system has puzzled physicians since antiquity; indeed, most theories were incorrect until 1628, when William Harvey, the

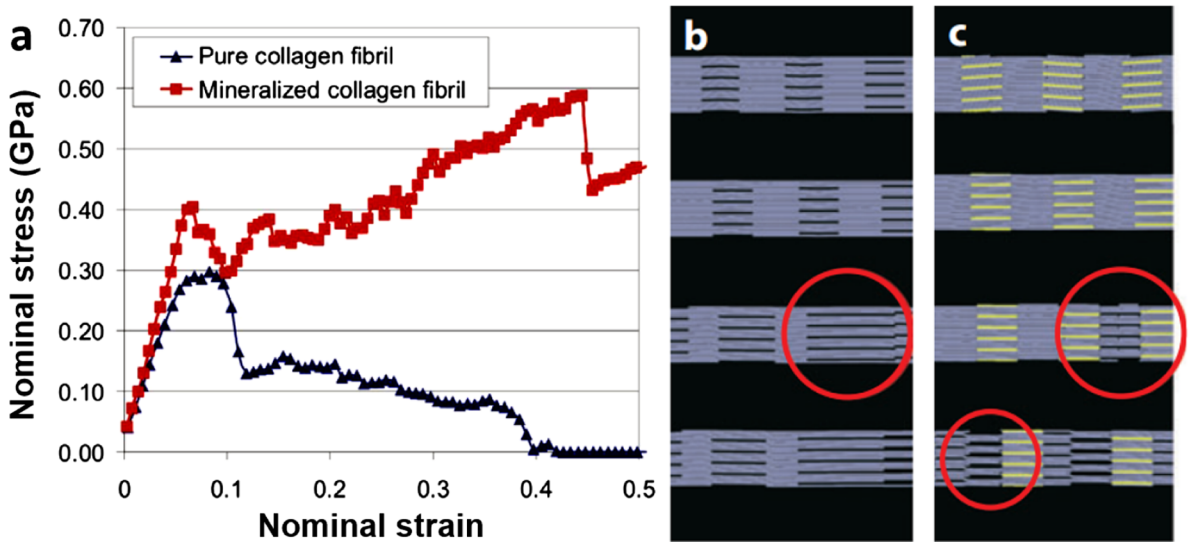

Fig. 1.8. Molecular dynamics simulation of the tensile behavior of the collagen fibril, which illustrates the toughening mechanisms between the non-mineralized and mineralized collagen fibrils while they are stretched [43]. (a) Stress-strain response of a mineralized *vs.* an unmineralized collagen fibril, revealing significant effects of mineral crystals in the collagen fibril during their mechanical response. (b and c) Deformation response of (b) collagen and (c) mineralized collagen fibrils. Slip occurs by intermolecular sliding. In mineralized fibrils, slip takes place at the interface between mineral particles and tropocollagen molecules. Repeated occurrence of slip (*red circles*) generates nanoscale voids and reduces the density.

English physician, published his results solving the mystery of the arterial and venous systems. Although he did not uncover capillaries, he reasoned that a communication between the two systems must exist. Though published in 1628, it is interesting that, in 1242, an Arab physician, Ibn al-Nafis had already provided this explanation.

Fig. 2.1a shows in schematic fashion the arterial (in red) and venous (in blue) systems; the sequence of artery-arteriole-capillary-venule-vein can be seen [45]. It is also evident that the structure of arteries and veins is different; specifically, arteries must sustain higher pressures from the heart as the blood is pumped through the body. This results in differences in the sizes of the walls. Both arteries and veins have characteristic layers known as tunica intima, media and adventitia. The arteries close to the heart have a larger diameter and are more elastic; the smaller ones show a more pronounced viscoelasticity and have a greater muscle content [46].

The principal load-carrying component of arteries and veins is collagen, which is arranged helically in the media and adventitia layers as shown in Fig. 2.1a [45]. The arrangement of collagen varies from layer to layer. In the innermost layer, the intima, collagen fibers have a dispersed orientation. The intima acts primarily as a barrier between circulating blood and the thrombogenic subendothelial tissue to control hemostasis; it is very thin, but thickens and hardens with arteriosclerosis. In the media, collagen fibers form a tri-dimensional network together with muscle and elastin. These are organized into concentric lamellae with ~10 μm thickness. The orientation of the collagen in the lamellae is helical with a small pitch, with alternating rotation directions. This is essential to ensure that no rotation takes place with pressurization. The adventitia also contains collagen organized in a helical pattern. Similar to skin (as described in Section 2.3), these collagen fibers form a tri-dimensional network and are curved.

2.2. Eye cornea and sclera

The cornea contains an outstanding arrangement of collagen fibers which have two functions: to resist the intraocular fluid pressure and to ensure transparency. Collagen is the primary structural component of the cornea which has a thickness of ~500 μm; the stroma makes up about 90% of the cornea. The collagen fibers in the stroma are staggered in layers (lamellae) with an approximate thickness of 2–4 μm each (Fig 2.2a); these layers are arranged in a somewhat orthogonal manner. Measurements made by Meek [47] show that 66% of the fibers are contained in a Maltese cross pattern, as shown in Figs. 2.2b and 2.3; the boundaries are within angles of ± 22.5° to the horizontal and vertical axes. The resultant structure is thus anisotropic. There are significant differences in the collagen fiber diameters and separation between the cornea and other organs; they have a smaller diameter (~25–30 μm) and are spaced in a regular pattern within the ground substance (proteoglycans) in the cornea (Figs. 2.2a). Their spacing is ~60 μm [48]. Collagen makes up approximately 15% of the cornea, with other proteins corresponding to 8%, the remainder being water. Rayleigh scattering decreases as the scattering center size decreases and therefore the smaller collagen fibrils and their separation by the proteoglycans play an important role. Apparently, the refractive index of the ground substance and collagen are close. The current thinking [47,48] on cornea transparency is that the collagen has short range ordering in its arrangement, which is essential to its transparency.

The intraocular pressure p varies from individual to individual and is in the range 1.5–4 kPa. The stress on the collagen lamellae,

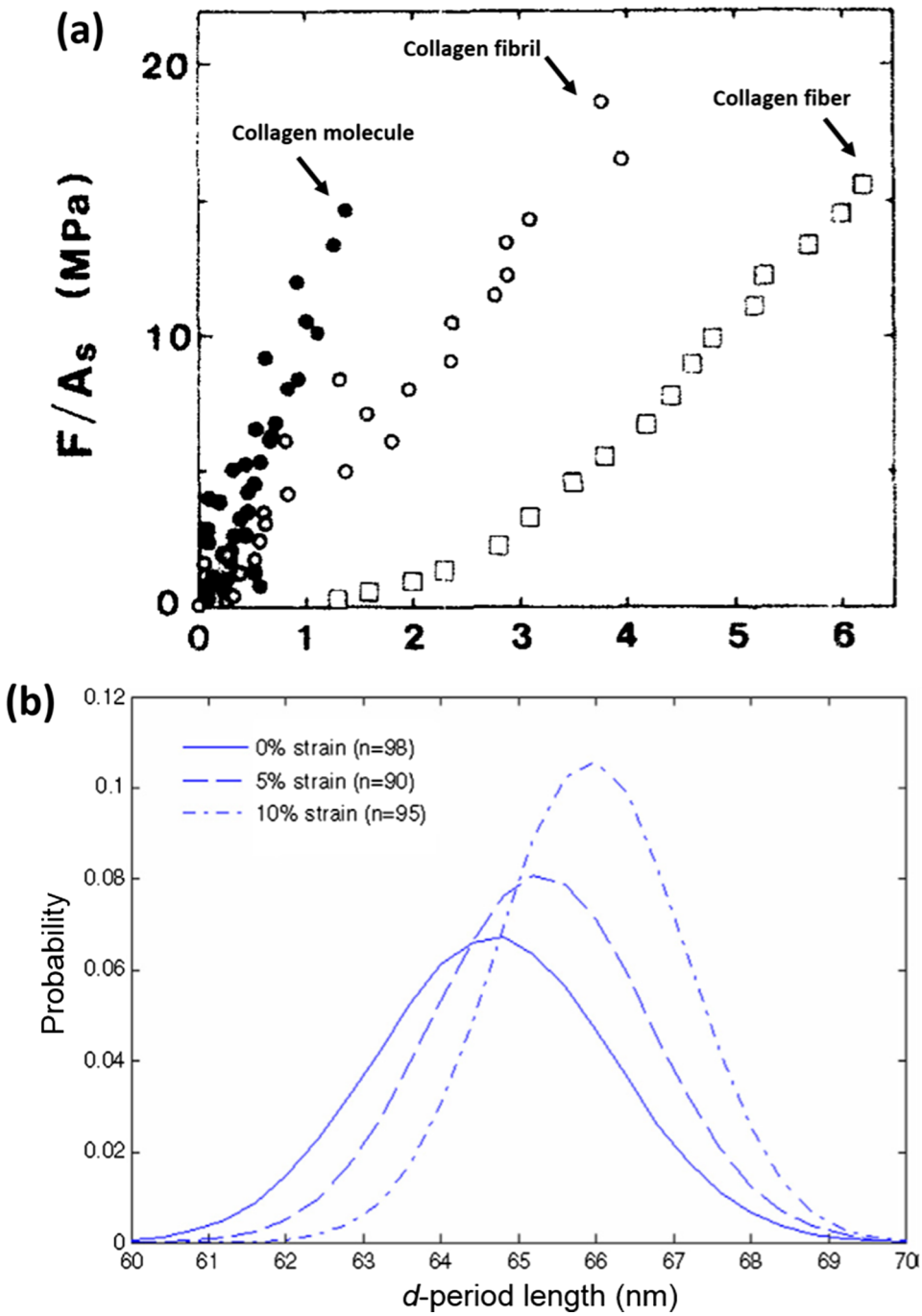

Fig. 1.9. Comparison of stress-strain curves for a collagen molecule, collagen fibril and a tendon (collagen fiber) [6,44]. (b) Probability distribution of collagen fibril *d*-spacing as a function of the measured strain on the tendon (= 0, 5, and 10%). The *d*-spacing increases with increasing total strain of the tendon, as the distribution narrows [40].

calculated from Eq. (1), is much lower than their strength:

$$\sigma_{max} = \frac{pr}{2t}, \tag{1}$$

where t is the stroma thickness (~500 μm) and r is the radius of the cornea (~7 mm). For a pressure of 4 kPa, the stress is equal to 28 kPa. The maximum pressure that the cornea can withstand is 3 MPa, *i.e.*, three orders of magnitude higher; this maximum pressure corresponds to a tensile stress of 36 MPa, which compatible with other keratins.

The sclera, on the other hand, is thicker and opaque. The arrangement of collagen is not as regular and other components

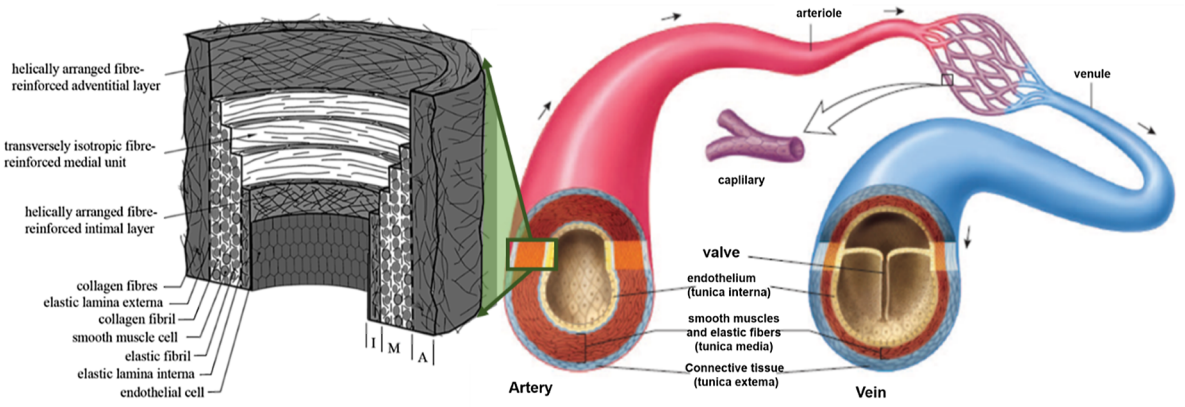

Fig. 2.1. Schematic drawing of the hierarchical structures of arterial (in red) and venous systems, with enriched blood flowing from arteries to arterioles to capillaries, the collagenous architecture of the artery wall is shown [45].

contribute to opacity.

Fig. 2.3 shows TEM micrographs of the collagen fibrils in the cornea (a and c) and sclera (b) [49,50]. The arrangement of the layers in the cornea is much more regular, as is the spacing of the fibrils. As mentioned above, this is essential for transparency in the visible light spectrum. Fig. 2.3d shows the corresponding array of the fibrils in the stroma with the average distance between them in the inset; their transmittance of light in the visible spectrum (400–1000 nm) is shown in Fig. 2.3e.

2.3. Skin and tendon

Skin, as the "outer layer" of the human body, has exceptional tear resistance to ensure that the internal organs remain intact. Additionally, it is multi-functional in that it provides for temperature regulation, camouflage, thermal energy collection, protection from the environment, and further houses a host of embedded sensors [51]. Along with elastin. Type I collagen is the main structural component of skin, existing primarily in the dermis layer and affording mechanical resistance to extension. A schematic illustration of skin, shown for that of a rabbit in Fig. 2.4a, indicates that it comprises three layers, namely the epidermis, dermis and endodermis.

As can be seen in the scanning electron microscopy (SEM) image in Fig. 2.5a [3], the dermis layer contains curvy collagen fibers, with diameters of ~5–10 μm, arranged in random orientations. Some types of the skin [56], such as chicken neck skin, also show a woven structure with effectively two orientations of collagen fibers, as seen in the dermis layer in Fig. 2.5b; the double arrow line shows one orientation of the collagen fibers (which are wider, roughly 20–30 μm in diameter, than in rabbit skin), with the other direction orientated approximately out of plane of the paper. Additionally, several collagen fibers form into ~100 μm sized bundles (or fascicles), a structural characteristic similar to that in tendons.

The structure of porcine skin is fairly similar to that of rabbit skin, with perhaps greater complexity. Fig. 2.5c shows a TEM micrograph of the porcine skin parallel to the surface. The wavy nature of the collagen is evident, with a wavelength of ~10 μm and amplitude of ~3 μm. There seems to be a tri-dimensionality to the structure, with fibers weaving in and out of the foil plane. The 67 nm *d*-spacing can be seen in collagen fibrils close to parallel to the foil, whereas elliptical and circular sections show fibrils that traverse the foil. These fibrils are grouped in fibers with a diameter of ~2 μm. This tri-dimensional arrangement provides the dermis with a weave-like pattern which is thought to enhance the recovery of its original shape. After extension to failure, the original waviness of the collagen fibers disappears (Fig. 2.5d), and is replaced by much smaller irregularities undoubtedly due to spring-back after fracture.

Frogs and toads (semi-aquatic) are members of the class Amphibia, quite different from reptiles. Their skin structure in some cases is very complex, having to perform functions that are quite unique. They breathe through their ventral skin and absorb water directly through it. Some frogs and toads have poison glands in their skin. The collagen arrangement of frog skin stratum compactum of *Bufo marinus* has been determined through TEM by Schwinger et al. [57] and consists of an orthogonal pattern of collagen fibers, shown in Fig. 2.6. The tela subcutanea contains numerous elastin fibers, marked by arrows in Fig. 2.6c, in addition to the wavy pattern of collagen fibrils.

The tendon is a tissue that connects bone and muscle; its structure is shown in Fig. 2.4c [52]. Collagen fibers in tendon have a diameter of ~1–20 μm and are slightly crimped and twisted, form fascicles with a diameter of ~50–300 μm, the crimps occurring roughly every 300 μm [58]. The interfascicular matrix surrounding the fibers is highly cellular and contains proteoglycans, glycoproteins and elastin [53], which are likely to regulate the fascicle sliding [54].

There is clearly a relationship between the structure of skin (Fig. 2.5a–d) and that of the tendon (Fig. 2.7a–d), in terms of the collagen morphology generated during the development of collagen fibrils in tendon and the ligament in the early fetal (Fig. 2.7a), late fetal (Fig. 2.7b) and mature periods (Fig. 2.7c and d) [60]. Specifically, at the early stage of fetal development, the collagen fibers show a similar morphology to skin with very curvy shape in random orientations (Fig. 2.7a); at the late fetal development, the fibers start to separate into fibrils but still maintain their marked curvature with a clearer orientation (Fig. 2.7b), whereas in mature rat

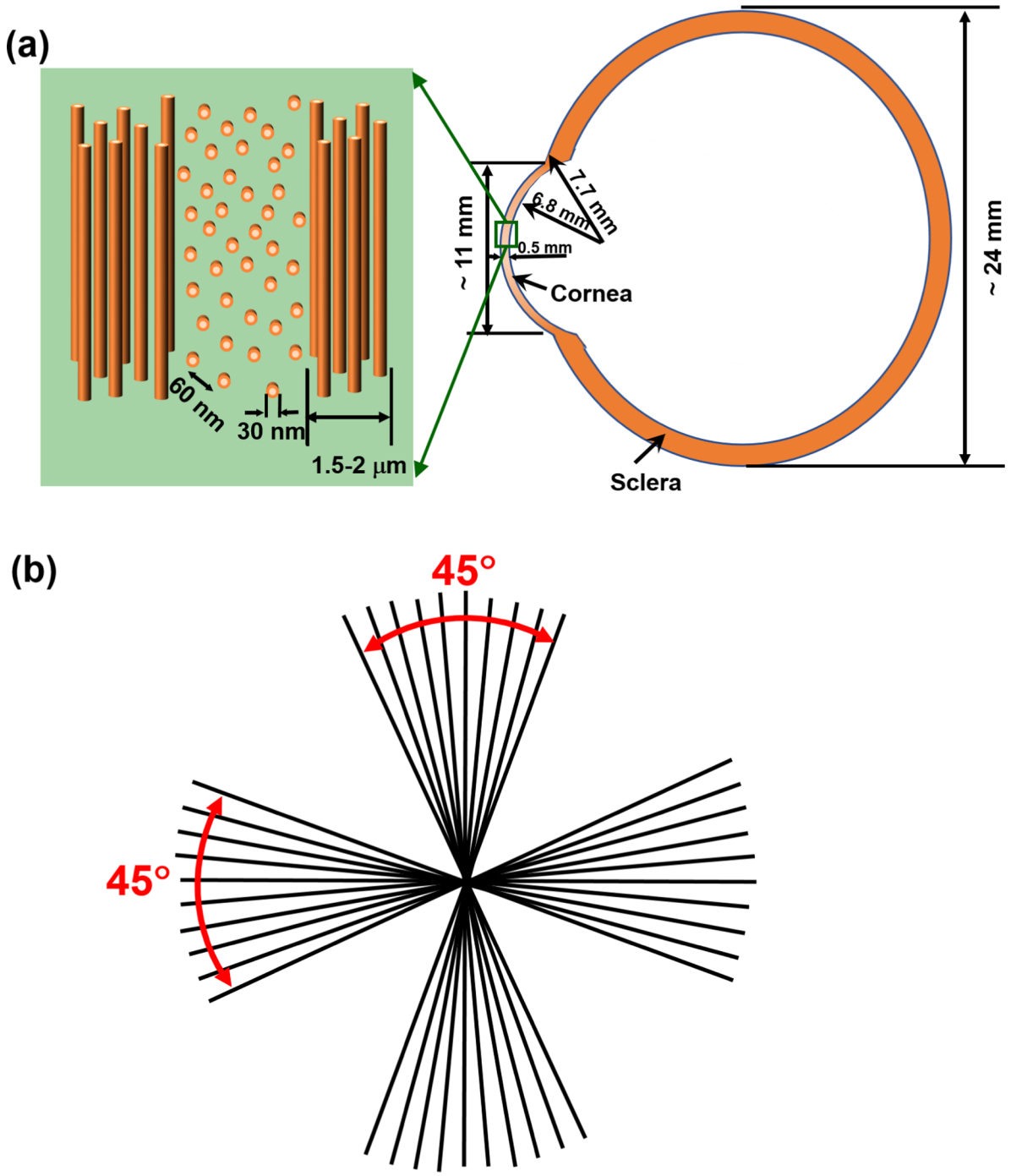

Fig. 2.2. Human eye. (a) Schematic of the cross section of the human eye with details of cornea. Note that stroma is comprised of lamellae of collagen fibrils with characteristic diameter of 30 nm and spacing of 60 nm with short-range order enabling transmissivity of visible light in the 400–700 nm spectrum; (b) Lamellae are arranged in two principal orientations shown by the Maltese cross pattern; 66% of collagen fibrils are within the region defined by 45° angles.

tendon, the collagen fibrils are straight, interweaved with some degree of overlap (Fig. 2.7c). TEM studies indicate that there can be a wide variation in the diameters of collagen fibers in tendon [59]. The interfascicular matrix, imaged by TEM in the upper right inset in Fig. 2.7d, shows the *d*-spacing of collagen fibrils aligned with the long axis of tendon. On straining, all the collagen fibrils are stretched with increasing *d*-spacing values up to 2–3% strain. At larger global strains, part of the fibrils relax back to their unstressed lengths while the rest continue to elongate to a strain of 4–5% [61]. Similar to tendon, the collagen fibrils in skin can be stretched

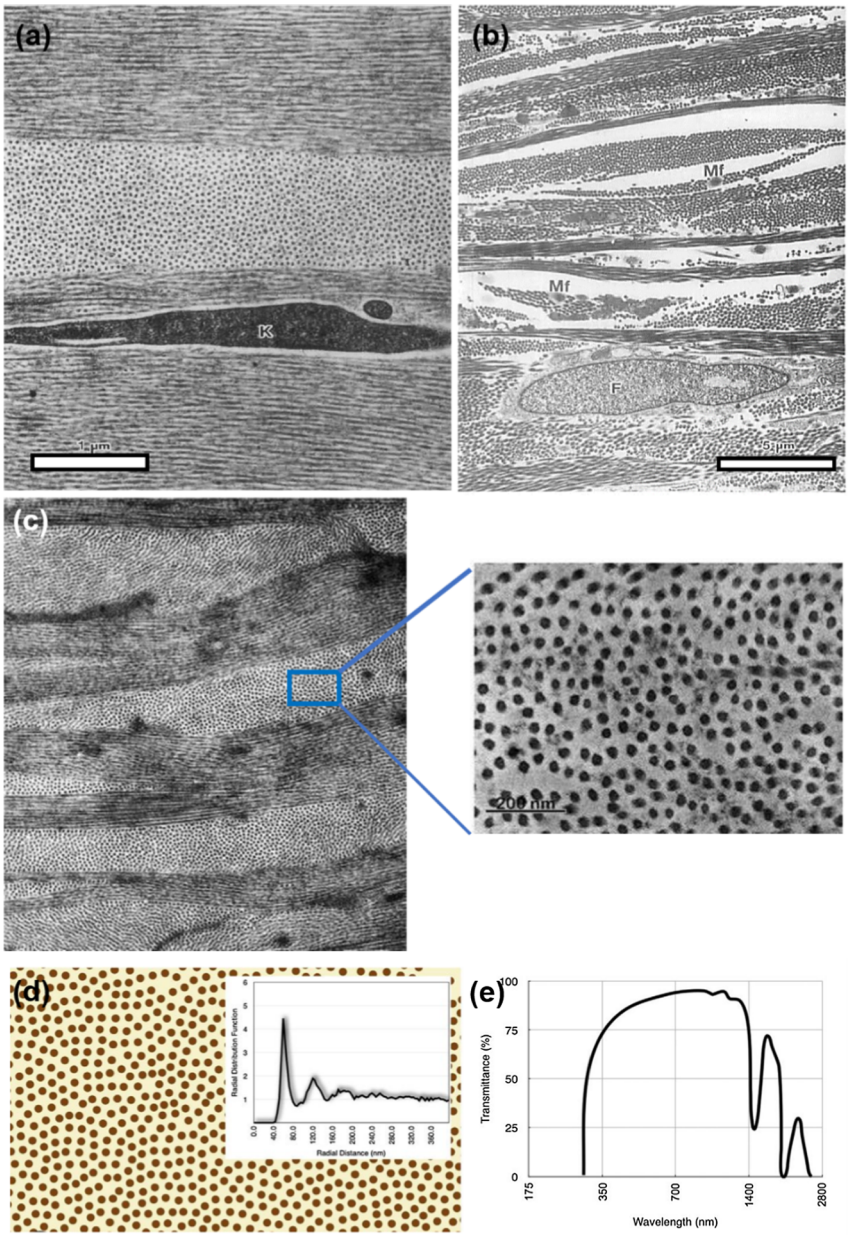

Fig. 2.3. Cornea and sclera of the human eye. (a) Well-arranged collagen fibrils with a uniform diameter in the cornea and (b) collagen fibers parallel formed in lamellar bundles in sclera [49] (c) Cross section of cornea stroma of wild type mouse showing collagen lamellae; detail showing regular size and spacing of lamellae that is responsible for transparency [50]. (d) Spacing of collagen fibrils in human stroma; the radial distance, calculated from the observed spacing, is shown in inset. Maximum spacing of collagen fibrils ~60 nm. (e) Transmittance of light as a function of wavelength for human cornea. Note that below a wavelength of 300 nm, transmittance drops to zero. Maximum transmittance corresponds to wavelength of visible light (400 to 700 nm).

with increasing strains of roughly 4%, without including the strain required to straighten the fibrils [3]. Accordingly, the local strain of the curved collagen fibrils in skin can be much higher than that in tendon due to such straightening mechanisms.

Tendons (connecting bone to muscle) and ligaments (connecting bone to bone) have an important structural function and are essential components of the muscle-skeletal system of vertebrates. Whereas skin is subjected to biaxial stresses in most circumstances (except in foreign object impact and penetration where there is a third direction of stress application), tendons and ligaments are primarily subjected to uniaxial tension. This results in a different, uniaxially arranged, architecture that is shown in Fig. 2.8a. The hierarchy progresses from molecules to microfibrils to fibrils and fibers, in an analogous manner to other Type I collagens. However, the fibers organize into fascicles, which are crimped to provide the necessary increase in stiffness with extension. Fascicles, in turn, form the tendons and ligaments. This crimped structure can be seen in Fig. 2.8b for both patellar and Achilles' tendons. In both cases,

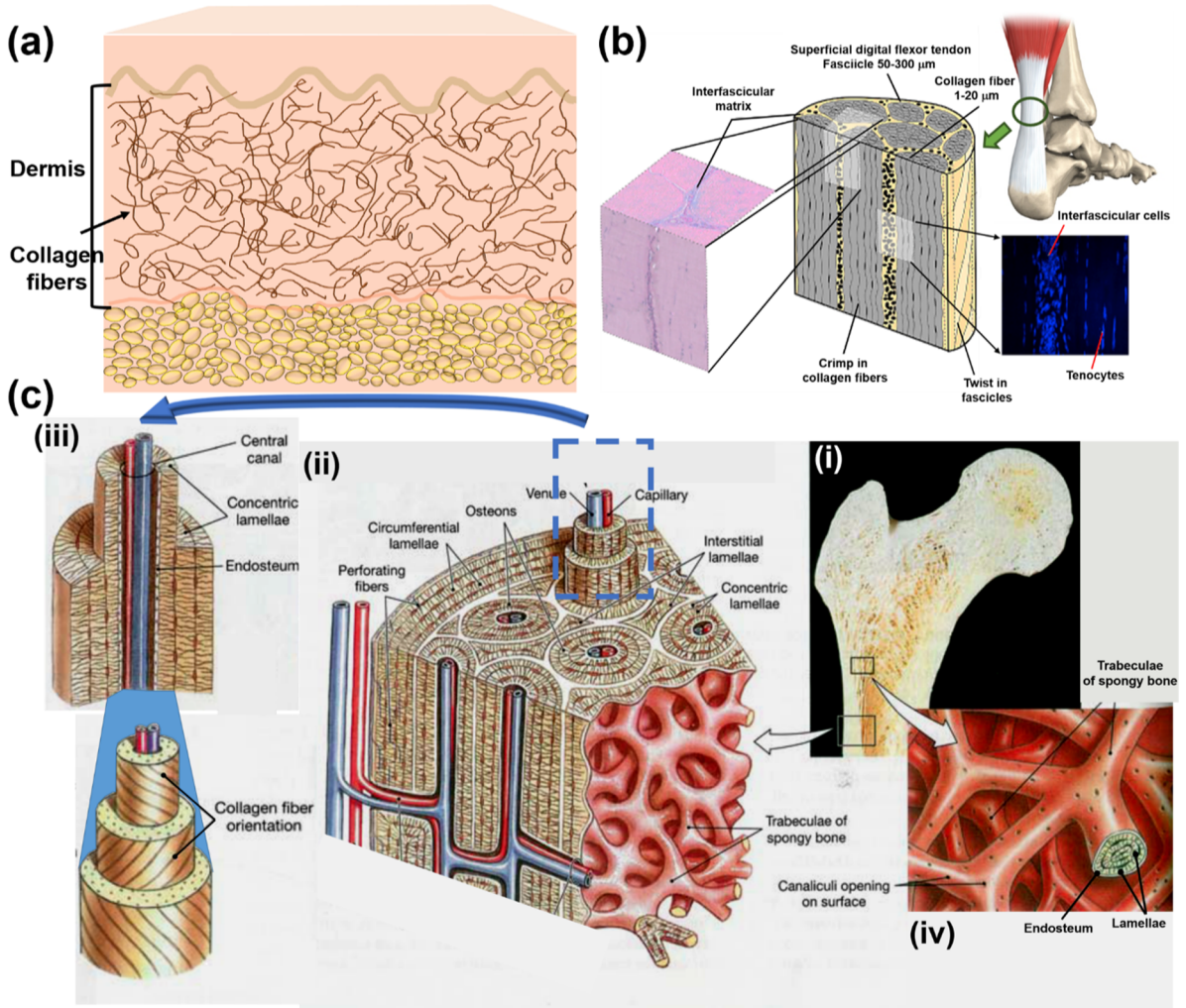

Fig. 2.4. Hierarchical structures of skin, tendon and bone. Schematic drawing of the hierarchical structures of (a) rabbit skin, with curved collagen fibers mainly existing in dermis layer and formed in random orientations. (b) Tendon [52], with fascicles, the largest sub-unit of the tendon of diameter of 50–300 μm, which are bundles of collagen fibers (diameter of 1–20 μm) surrounded by the interfascicular matrix. The collagen fibers are slightly crimped and twisted in fascicles. The interfascicular matrix is highly cellular and contains proteoglycans, glycoproteins, and elastin [53], which are likely to modulate the fascicle sliding [54]. (c) Cortical bone [55] contains osteons with concentric lamellae of collagen fibers around and interstitial lamellae between them. Trabeculae in the spongy bone are composed of lamellae of collagen fibers.

it comprises a coordinated zig-zag pattern that, on straightening, exerts an increasing resistance to external loads. The patellar tendon, however, has less of a crimped structure, with a larger occluded angle, than that of the Achilles' tendon.

2.4. Structural components of mineralized collagenous materials: Bone and fish scales

Bone is also a mineralized collagenous material. It has low density ($\sim$2000 kg/m^3), which can be significantly decreased in the trabecular configuration. Specifically, it is a layered material with a complex hierarchical structure [55] characterized by spongy (trabecular) region inside and compact (cortical) bone as a circumferential outer layer, which is covered by a periosteum membrane on the outer surface with penetrating Sharpey's (collagen) fibers. Within compact bone, there are osteons, which are functional units, through which bone can remodel, with a diameter of $\sim$200–300 μm [11]; these osteonal structures hold blood vessels inside a central (Haversian) canal with capillaries and venules. Compact (cortical) bone is made of several structural lamellae; those close to the periosteum membrane are called circumferential lamellae, those found in the osteons are called concentric lamellae, whereas those between the osteons are named interstitial lamellae. These lamellae, which display different orientations of collagen fibers, provide a major contribution to the excellent mechanical properties of bone.

Spongy (or trabecular) bone fills the interior of the bone and has an open cell porous structure with lamellar mineralized collagen as the cell struts covered by endosteum (the boundary between the compact bone and spongy bone). It comprises some 20% of the total bone mass but nevertheless displays almost ten times the surface area of the compact bone [64].

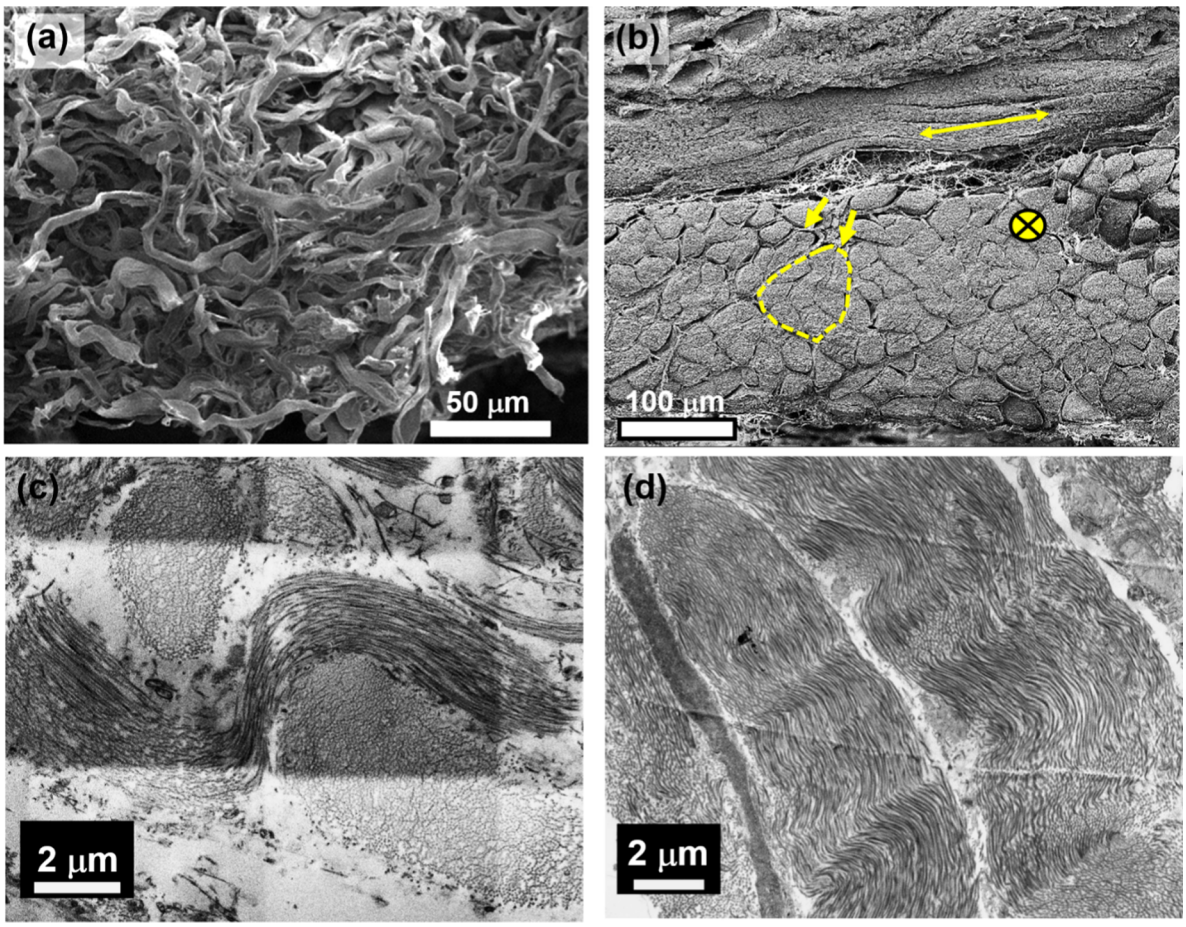

Fig. 2.5. Collagen arrangement in rabbit and piscine skin. (a) Random arrangement of collagen fibers in rabbit skin, the diameter of the collagen fiber is ~5–10 μm [3]. (b) The collagen fibers are arranged roughly in two orientations, one is shown by the double solid line arrows, the other is shown by the direction entering into the paper, shown by ⊗. The diameter of the collagen fiber is ~20–30 μm; the inter-fascicular matrix is shown by the dashed line circle and the arrows. (c) and (d) SEM images of collagen fibrils in piscine skin in (c) original (undeformed) state and in (d) stretched (deformed) state.

At the nanometer/molecular level, bone can be considered as an interpenetrating composite, with both the collagen and mineral forming a continuum [65,66]. The size and structure of the HAP mineral platelets in bone has been established by Weiner and Price [67] and Schwarcz et al. [68] to be on the order of 40 × 50 × 3–5 nm. Specifically, there are three locations where HAP platelets have been observed:

1. *Intermolecular HAP:* Intermolecular HAP was first hypothesized by Landis *et al.* [69]) to be located in the gaps between the collagen molecules (Fig. 2.3a), with a size of ~40 nm in length and a diameter of ~1.5 nm. These gaps comprise a volume percentage of up to 14% (40 nm/340 nm). However, it is difficult to envisage a platelet since only one of the dimensions satisfies the requirements. Rather, such intermolecular HAP is better described in the form of needles. Fig. 2.9a (right) shows the traditional depiction of these needles; their actual proportion is shown in Fig. 2.9a (left) with a typical length-to-diameter ratio of ~30. According to this model, the HAP nucleates in the gaps between molecules and grows from there.
2. *Intrafibrillar HAP:* Intrafibrillar HAP was proposed by Alexander et al. [22] and refers to the placement of HAP platelets around collagen molecules, as shown in Fig. 2.9c. The mineral platelets create a continuous arrangement intrafibrillarly in a 3-D network between the collagen molecules.
3. *Interfibrillar HAP:* This form of HAP can locate in the interstices between the fibers (Fig. 2.9b). The interstices occupy a volume percentage of ~18%, readily calculated considering an idealized array of cylinders in a closest packing arrangement. The fibrils have a diameter of ~100 nm, and if one considers six sides, one has platelets with a lateral dimension of 50 nm, corresponding to actual measurements. Schwarcz et al. [68] provide strong support for this class of HAP; indeed, this work advocates that interfibrillar HAP provides a continuous network. Fig. 2.9d and e shows computed tomography (CT) images produced by scanning transmission electron microscopy that present clear evidence for interfibrillar HAP. Such HAP, shown in cross section in green in Fig. 2.9d, surrounds the holes which correspond to the collagen fibrils. There is no clear evidence of HAP inside them, most being

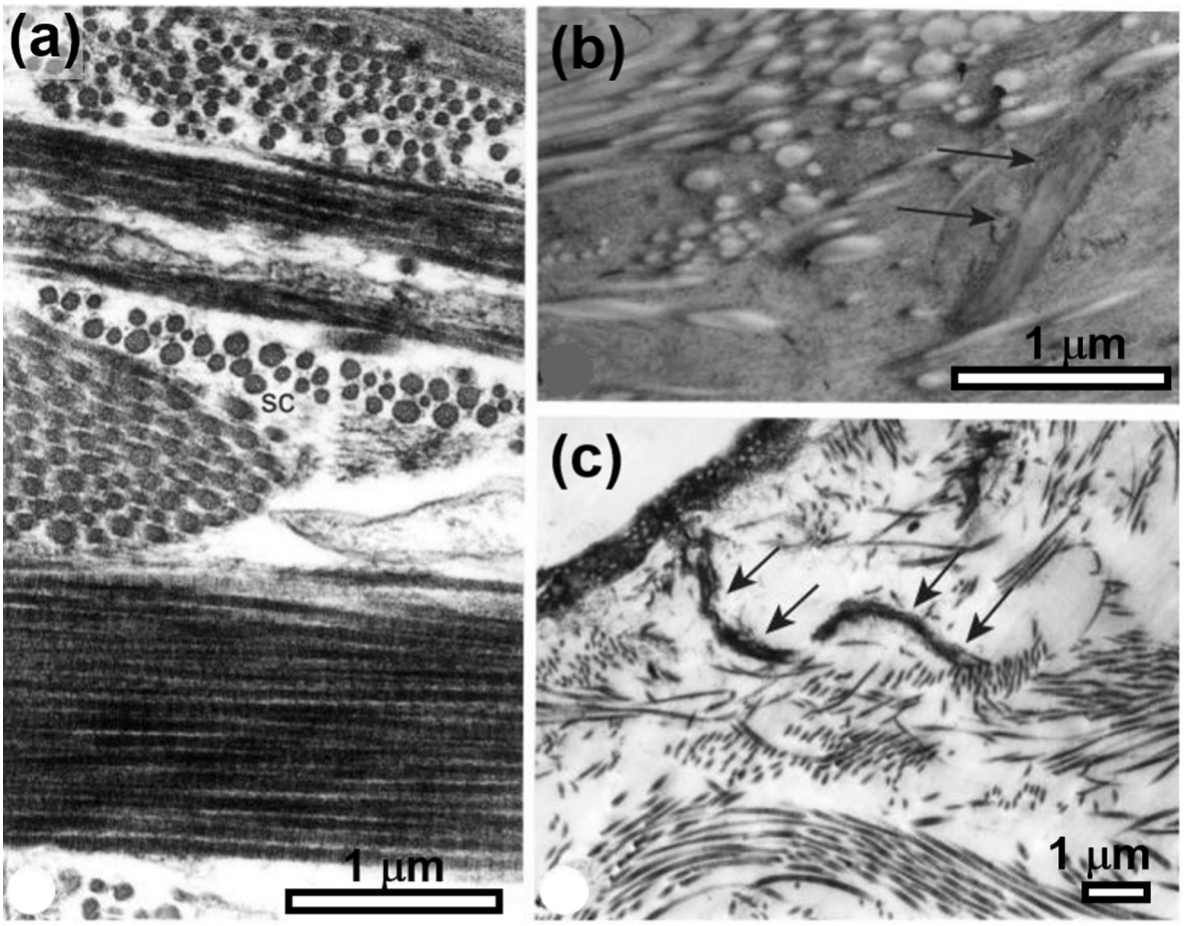

Fig. 2.6. Collagen arrangement in stratum compactum and tela subcutanea. (a) Criss-cross arrangement of collagen layers in the stratum compactum (sc) of Bufo marinus. (b) Transmission electron micrograph of a small elastic fiber (arrows) between collagen fibers. (c) Transmission electron micrograph of the tela subcutanea with numerous elastin fibers (arrows). [57]

located between the fibrils. The CT picture of the longitudinal section in Fig. 2.9d shows some banding characteristic of collagen, supporting the hypothesis of intermolecular HAP.

4. *Osteonal HAP*: At a coarser scale, the boundaries of the osteons, termed the cement lines, are generally more mineralized in the form of osteonal HAP. Such mineralized cement lines can provide additional stiffness yet are locations where incipient cracks in compact bone tends to deflect along. This in turn provides a dual function; it provides for significant extrinsic toughening for cracks propagating in the transverse (breaking) orientation, yet at the same time lowers the longitudinal toughness of bone (for this reason, bone is invariably easier to split that to break) [72].

Recently, Reznikov et al. [71] studied the continuity for the mineral phase of the bone (Fig. 2.9f) by using three-dimensional electron tomography imaging and high-resolution two-dimensional electron microscopy. These authors demonstrated that bone mineral is hierarchically assembled beginning at the nanoscale: needle-shaped mineral units merge laterally to form platelets, and these are further organized into stacks of roughly parallel platelets. The platelets aligned at the collagen fibrils (Fig. 2.9f) and span adjacent fibrils as continuous, cross-fibrillar mineralization.

Another example of highly mineralized collagenous materials are ganoid fish scales [13,14], for example, in the alligator gar fish. Ganoid scales are one of several types of fish scales, that also include placoid, cosmoid and elasmoid (cycloid and ctenoid) scales [73]. Placoid are typical scales of sharks and rays. They have a surface structure that generates small-scale vorticity in water, thereby decreasing drag; their core consists of pulp which is surrounded by dentine and an outer vitrodentine layer. Cosmoid scales are similar to placoid scales and likely evolved from the fusion of them; they have dentin, vitrodentine and a tissue complex known as cosmine with interconnected canals and flask-shaped cavities, but lack a pulp core. The elasmoid class consists of two kinds of scales, cycloid and ctenoid. They have similar shapes, but cycloid scales have a smooth surface while ctenoid scales have a comb-like outer surface. Ganoid scales are modified cosmoid scales which are also rhombic, rigid and jointed articulating scales of two layers. They are composed of a thin surface layer of ganoine, akin in hardness to tooth enamel, riding on a softer but tougher bony foundation. These are the hardest scales in fish and are characteristic of the alligator gar and Senegal bichir.

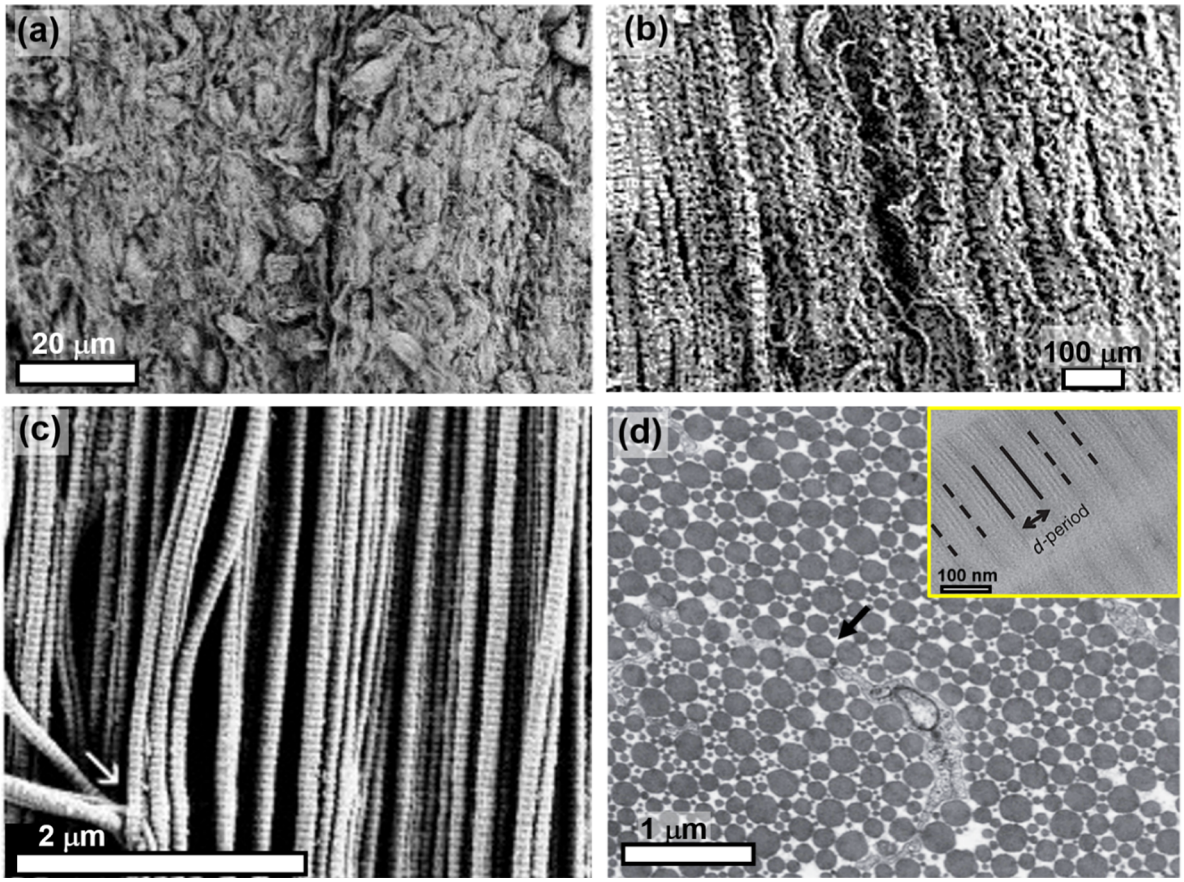

Fig. 2.7. Collagen fibers and fibrils in tendon. (a) Organization and structure of collagen fibrils from the bovine tendon and ligament during early fetal development. (b) Collagen fibril morphology in patella tendon during late development. (c) Collagen fibril organization and morphology in mature rat tendon; the arrow shows the fibril overlap and interweaving, (d) tendon sectioned transversely to the long axis of the tissue showing fibrils as circles; the top-right inserted figure shows the *d*-spacings of collagen fibrils from the side view of the long axis of the tendon [59]. (Figures were taken from Provenzano and Vanderby [60]).

The adult alligator gar ganoid scale has a maximum thickness of ~4.5–5 mm at the center and a length of ~30–40 mm along the rhombus' long diagonal [14]. The aspect ratio (equal to total length/thickness) is ~8.7 and the degree of imbrication (equal to exposed length/total length) is typically 0.78. The scale is comprised of two layers: an outer ganoine layer and an inner bone layer, as shown in Fig. 2.10a. Ganoine is a hard layer with a thickness in adult fish of about 600 μm; it covers ~40–70% of the fish scale surface in the center and contains hydroxyapatite rods with a width of ~40 nm. The inner bone layer, which is typically thicker than ~3 mm, is composed of ~65 wt% mineral and ~35 wt% collagen; it contains various sizes of tubules, some of which contain collagen fibers inside. The largest tubules (~200 μm in diameter) are usually found at the center of the scale where the ganoine is not fully covered. The width of other tubules in bone layer averages ~3 μm with a spacing of ~5 μm at the inner surface close to the fish skin (shown in Fig. 2.11a). Many of the tubules contain collagen fibers which extend approximately through the thickness direction with a bending curvature shown in Fig. 2.11b. The mineral not only exists in the collagen fibrils but also attaches to the collagen fibrils (Fig. 2.11c). For a better understanding of the structure of alligator gar scale, both the deproteinized and demineralized scales and their morphologies are shown in Fig. 2.11d, e and f, respectively. The mineral exists in the interfibrillar matrix (Fig. 2.11d) and shows a porous structure which may have been originally filled with protein. The deproteinized "collagen" fiber comprises nanoscale mineral sheets in different orientations complying with the fibril shape of collagen, indicating that the mineral is intimately connected to collagen. The sheets have dimensions of ~75 × 25 × 3 nm (Fig. 2.8e). Fig. 2.8f shows a deproteinized collagen fibril with a clear *d*-spacing of 67 nm. Considering the surfaces of the mineralized (Fig. 2.11c), deproteinized (Fig. 2.11e) and demineralized collagen fibrils (Fig. 2.8f), it is clear that the mineral tends to fill the gaps along the collagen fibrils. Without the mineral, the collagen matrix of the gar scale would be very elastic, with a high tear resistance similar to skin, and difficult to fracture in bending. The presence of the mineral decreases the elasticity but provides a higher compressive strength, thereby enhancing its penetration resistance to an attack by the teeth of predator.

The arapaima fish is approximately the same size as the alligator gar; however, its scales are much larger (50–120 mm in size) and more flexible than those of the alligator gar. They are elasmoid scales and have two layers: a highly mineralized layer which contains ~55 wt% mineral with a thickness of ~400 μm, and a collagen layer (~85 wt% collagen) with thickness of ~1 mm. The aspect ratio

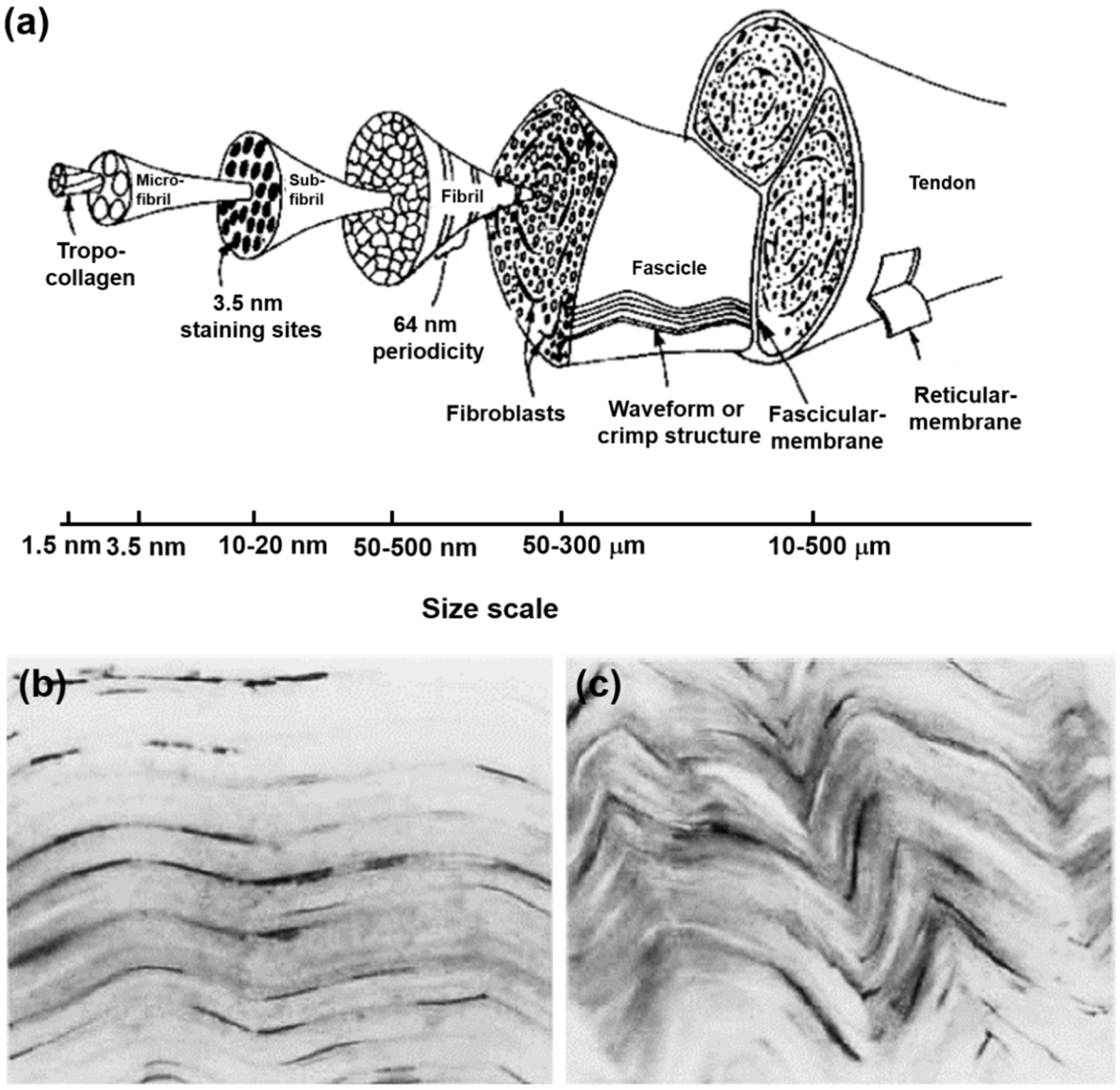

Fig. 2.8. The tendon. (a) Hierarchical structure of tendon showing crimped fibers in the fascicle (modified from Weiss et al., [62]) and SEM pictures of the (b) patellar tendon, and (c) Achilles' tendon [63].

of arapaima scale is ~50, much higher than that of the alligator gar scale, which enables the scales to flex when the fish bends; the degree of imbrication is 0.4 [15], lower than that of the alligator gar.

The outer mineral layer shows a pattern of ridges on the surface which characterizes the morphology of the surface (Fig. 2.10b). The inner collagen layer has a layered, Bouligand-type (twisted plywood) structure (shown in Fig. 2.12a and b) [15,75]. This structure is named after Yves Bouligand who was the first to describe this twisted plywood structure [76], where each layer is rotated with respect to the one directly adjacent to it. In this manner, a helicoidal ("spiral staircase") structure is produced that can be found in many different species; arthropod exoskeletons and layers in osteons are prime examples. In arapaima fish scale, the orientation of the collagen fibers varies from layer to layer, with each layer being ~50 μm thick. Fig. 2.12b shows that the collagen layers, labeled A–E, have included angles of α_1, α_2, α_3, α_4 forming a Bouligand-type hierarchical structure. After deproteinization, some pores, with a diameter of 2–5 μm, are revealed in this structure. The mineral shows a variation in orientation around the pores, marked by the arrows in Fig. 2.12c and d. In Fig. 2.12c, three orientations of collagen are shown by the arrows around the pores; these pores may have the function of tuning the orientations of fibrils by producing the continuous orientation changes for the fibrils in adjacent layers. The width of the mineral channels for collagen fibrils is ~150 nm while the collagen fibrils in a demineralized sample have a width of 120 nm; thus, they can fit well within the mineral channels. From the demineralized sample, protein linking can be observed from the tear between one fibril from the other (shown in Fig. 2.12f), implying that the collagen fibrils do not simply stack on each other, but are tightly connected by protein links and minerals. This configuration is akin to that in bone, shown in schematic fashion

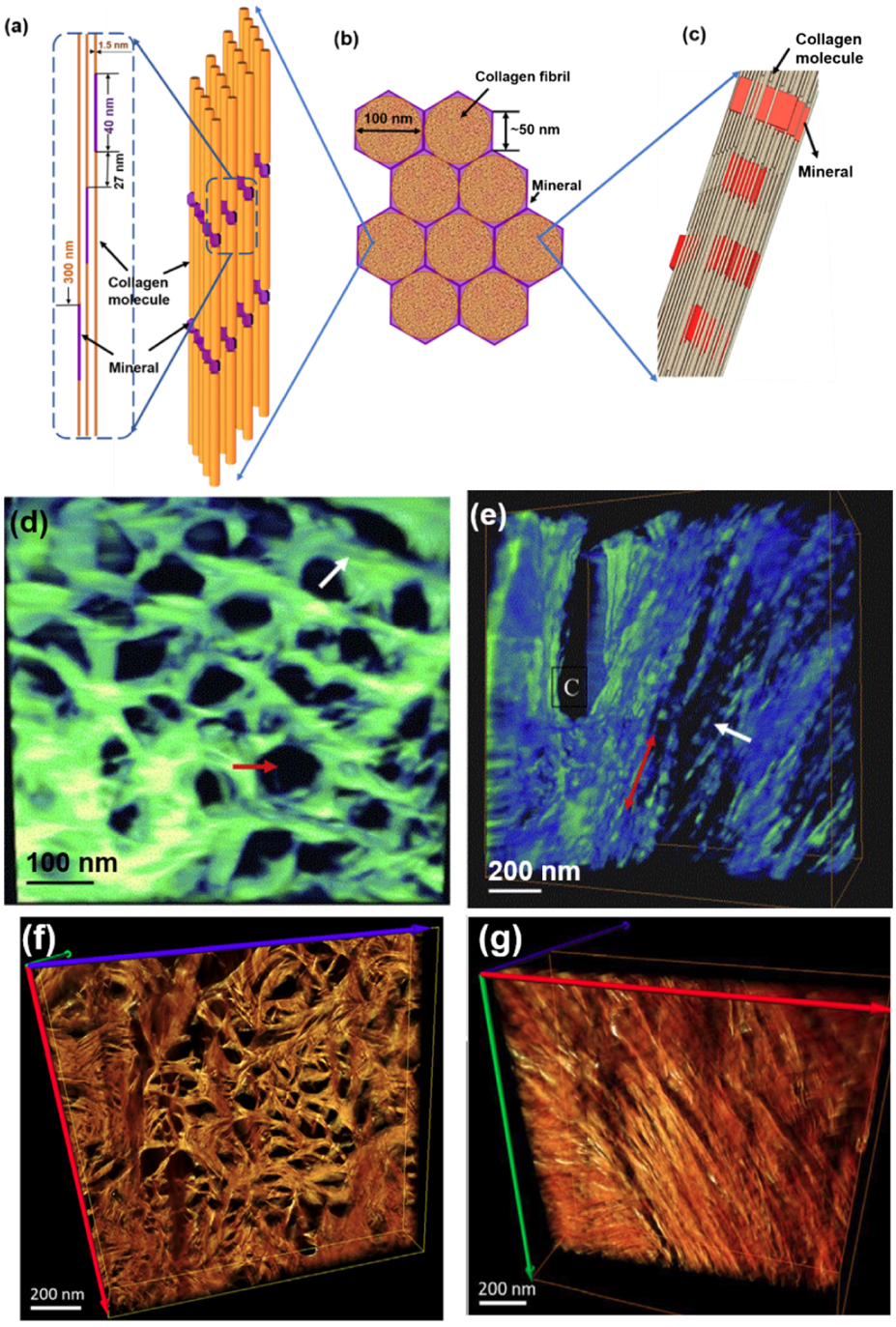

Fig. 2.9. The distribution of the mineral in the collagen fibers in bone. (a) Mineral filling in the gap of the head-to tail collagen molecules, the left picture of (a) shows the dimensional ratio of the collagen and mineral, (b) the collagen molecules forming the collagen fibrils which further with the mineral matrix constitute the part of one collagen fiber, (c) model from Alexander et al. [22] claims a continuous 3-D mineral arrangement with the collagen molecules, (d–e) tomography revealing HAP (green and blue) surrounding empty (collagen) holes in an interfibrillar fashion [70], (d) cross-section; (e) longitudinal section. (f–g) STEM tomogram in different projections of a FIB-milled specimen of mature human lamellar bone [71]. Note that there is no evidence of intrafibrillar HAP. The longitudinal section shows some banding of 67 nm, attributed to intermolecular mineralization.

in Fig. 2.9. The fibrils are embedded in a continuous HAP network and the dimensions of the HAP crystals are governed by the sizes of the interstices in the collagen structure.

Another similar hierarchical structure existing in elasmoid fish scales, *e.g.*, in the coelacanth fish, is the double Bouligand structure, first studied by Giraud et al. [77] and recently reviewed by Quan et al. [78] with new detailed findings on the interbundle

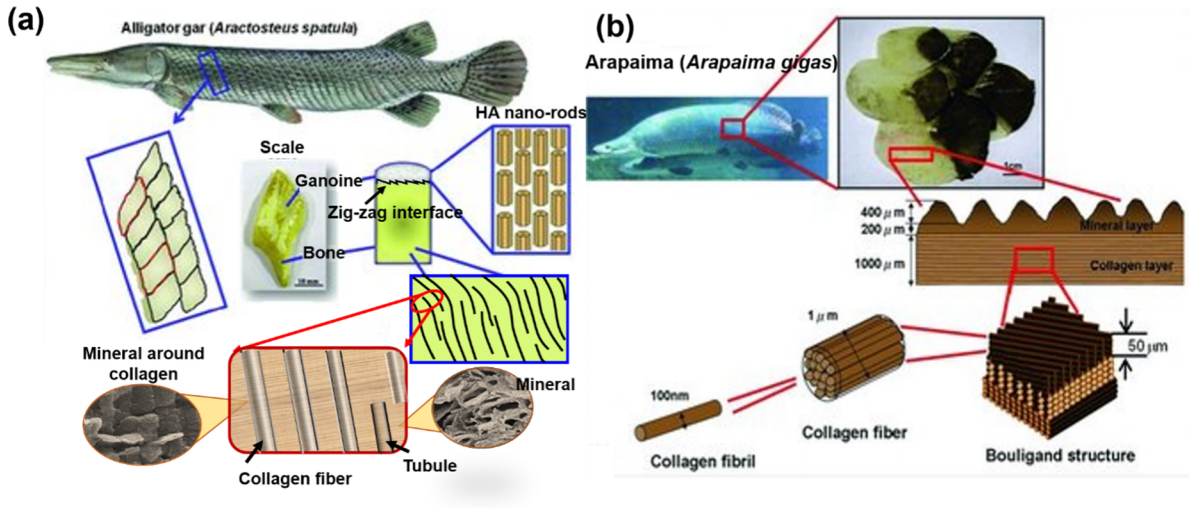

Fig. 2.10. Schematic illustrations of the hierarchical structures of fish scales. (a) alligator gar scale (reproduced from Refs. [14,74]) contains a ganoine layer with mineral rods aligning towards the outer surface and bone structure for the inner layer. Tubules and mineralized collagen fibers are aligned approximately in the thickness direction, the mineral shapes sheets around collagen fibrils and mineral around tubules are formed perpendicular to them. (b) Arapaima scale (adapted from Refs. [14,74]), where the scale has the outer mineral layer and inner collagen layer with a Bouligand-type structure.

fibrils and toughening mechanisms. Fig. 2.13a and b compares the architectures of the single and double-twisted Bouligand structures. Instead of a simple twisted plywood structure, the double Bouligand structure uses the orthogonal bilayer as a unit, shown in the inset image in Fig. 2.13c, to further form the twisted plywood structure (Fig. 2.13). The spaces between the fiber bundles are filled with fibrils perpendicular to the laminate structure, mainly along the thickness direction (Fig. 2.13d), which are referred to as interbundle fibrils. These features are loosely packed and tend to align around the fiber bundles to ensure the further constraint of the structural elements. Fig. 2.13e shows the round fiber bundles with the interbundle fibrils in random orientations (Fig. 2.13f).

3. Mechanical response of architectured mineralized/non-mineralized collagenous layers

3.1. Comparison between the mechanical responses based on nature-designed architectures

The various architectural structures in natural collagenous materials can generate a variety of deformation and toughening mechanisms which can lead to a wide range of mechanical functionalities. The tensile response of several collagenous materials is presented in Fig. 3.1; both mineralized materials (compact bone, cancellous bone, arapaima fish scales and alligator gar scales) and non-mineralized/demineralized materials (rabbit, chicken, demineralized arapaima fish scale and demineralized bone) are compared. Simplified sketches of the structure of these materials are shown on the right-hand of the Figure, together with the tension direction along which they were loaded. The tensile stress-strain curves indicate the uniaxial tensile properties of the collagen layers (without the outer mineral layers for the fish scales) for the different hierarchical structures. The curves for the non-mineralized collagenous materials (Fig. 3.1b) show the well-known J-curve shape, with the stiffness increasing with strain; in contrast, the mineralized tissues exhibit linear behavior.

When an artery (structure shown in Fig. 2.1) is pressurized, the collagen fibers tend to straighten, which was deduced from the small-angle X-ray scattering measurements of Holzapfel [46]. The mechanical behavior of arteries is shown in Fig. 3.2a for both the longitudinal and circumferential directions. If the externally imposed displacement (plotted on the abscissa) was completely accommodated by the stretching of the collagen fibrils, the strain due to the *d*-spacing (plotted on the ordinate) would be the same as the one from the external displacement. This is not the case though as the strain in the *d*-spacing is only 10% of the external applied displacement. Yang et al. [3] observed the same effect for rabbit skin and attributed the difference to collagen fiber straightening, reorientation and sliding.

Fig. 3.2b shows the characteristic J-curve behavior of artery. The range of physiological loading can be seen to be much lower than the maximum strength. Beyond a critical stress, marked at the point I, the deformation becomes permanent. This is related to the decrease in the slope and is accompanied by a marked increase in hysteresis (difference between loading and unloading paths), which corresponds to viscoelasticity. Both true (marked “material”) and engineering stress and strains are shown in Fig. 3.2b. Interestingly, upon loading to point III are reloading, the unloading is still essentially elastic, with a minimum of viscoelasticity (small hysteresis). This suggests that the artery has a response akin to work hardening, as the collagen fibrils undergo permanent reorientation in the first cycle.

The helical winding of the fibers creates a “Chinese fingertrap” effect by which the circumferential expansion by internal pressurization produces a reduction in length (negative stretch) in the longitudinal direction. This is shown in the calculated results

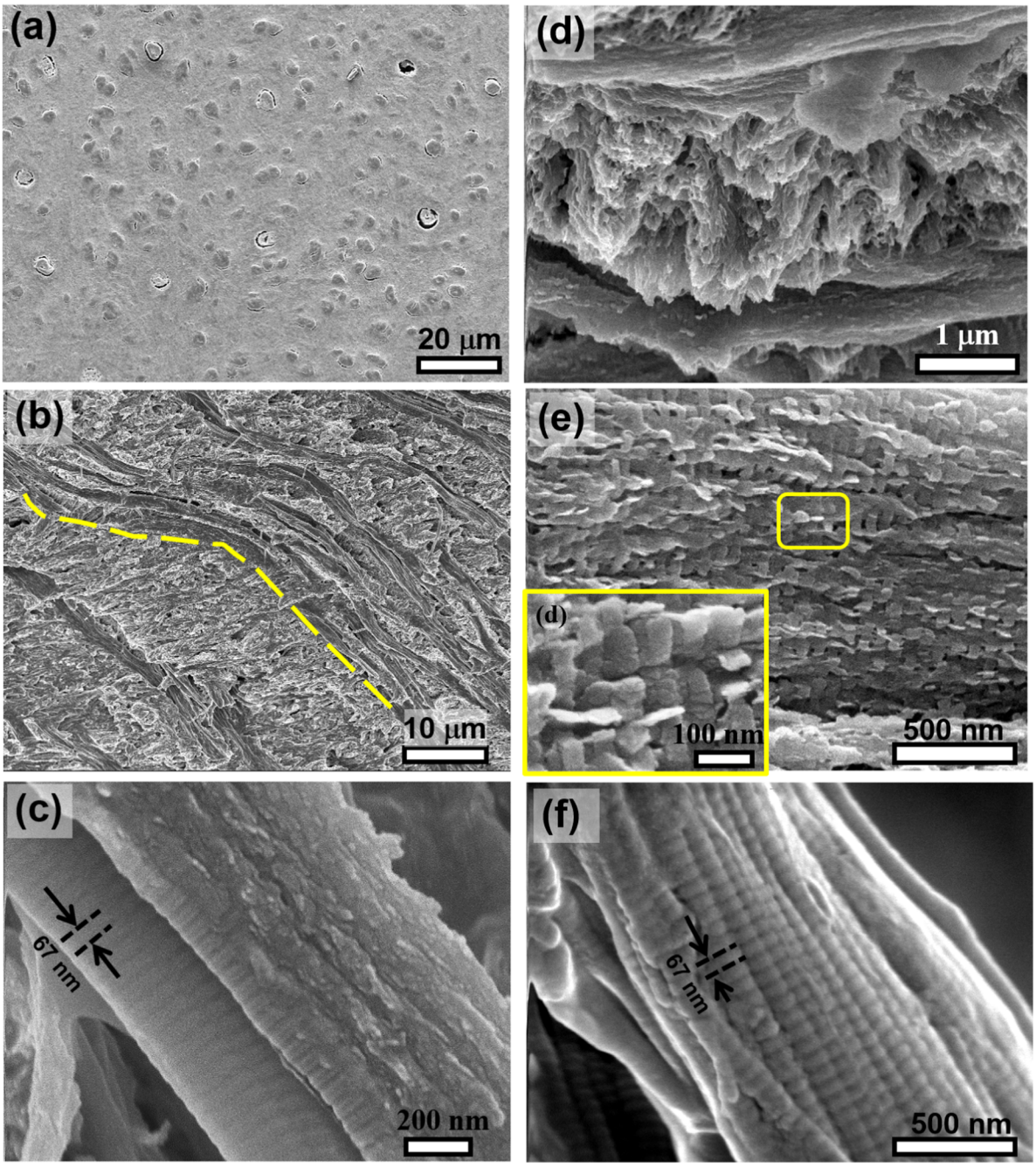

Fig. 2.11. The structure of bony layer of alligator gar fish scale. (a) Top view of sectioned collagen fibers and tubules of polished gar scale, (b) curved trajectory of collagen fibers through the thickness of the bony layer, (c) collagen fibrils with mineral matrix, (d) deproteinized gar scale, (e) deproteinized collagen fiber, the mineral plates around collagen fibrils showing different orientation to align the cylindrical shape of collagen; higher magnification of the mineral plates with dimensions of ~75 × 25 × 3 nm shown in the inserted picture at the left bottom; (f) demineralized collagen fiber with *d*-spacing of 67 nm. Note the obvious "deeper" gap regions (shown by dashed lines) in demineralized collagen fibers by comparison to the gaps in the mineralized collagen fiber in (c). Images in (a), (b) and (f) are from Ref. [73].

shown in Fig. 3.2c. The pressure causes a positive stretch in the circumferential direction and an equivalent negative stretch in the longitudinal direction. Three distributions of fibers are modeled by a dispersion parameter κ: $\kappa = 0$, corresponding to perfectly aligned fibers, $\kappa = 0.33$, corresponding to isotropic orientation of the fibers, and $\kappa = 0.23$, an intermediate case. The angle γ of the fibers with the circumferential direction is also varied: $\gamma \sim 40^\circ$, 50° and 60°. For $\kappa = 0.33$, there is no effect of γ and the longitudinal shrinkage (axial stretch ratio ~1) is modest. On the contrary, for $\kappa = 0$ the longitudinal stretch is the lowest (0.4 to 0.7).

For mineralized collagenous materials, compact bone with 33–43 vol% mineral content (Table 3.1) displays the highest strength

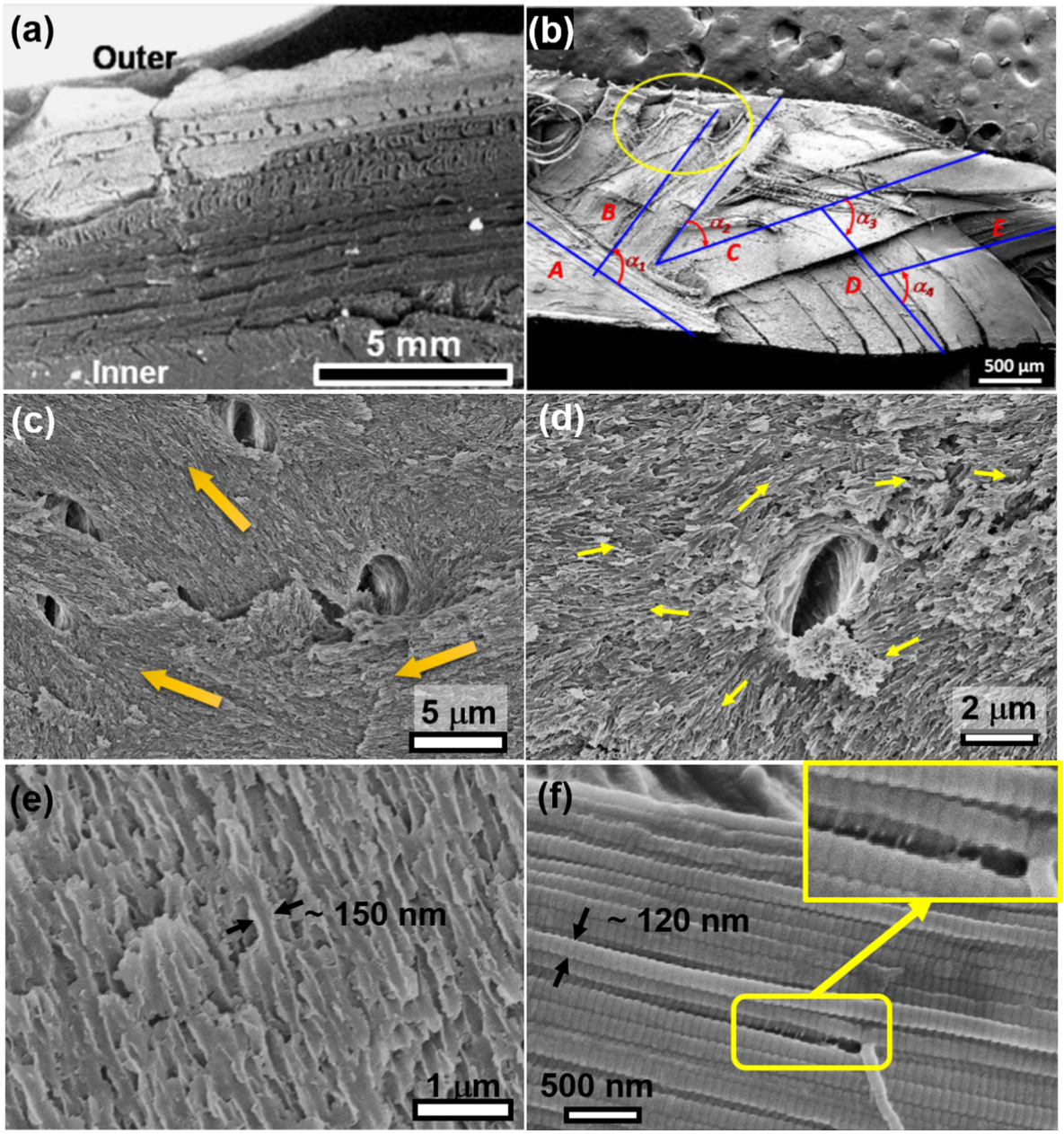

Fig. 2.12. Structure of arapaima fish scale. Arapaima scale has two layers, an outer mineral layer and an inner collagen layer: (a) the collagen layer contains several sub-layers with staircase orientations of collagen, termed the Bouligand structure, (b) the exposed surface of the scale after tearing shows different orientations of collagen fibers [15], (c) the deproteinized collagen layer shows porous structure with different orientations of mineral which indicate the orientation of the mineralized collagen fibers, (d) the pores tune the orientation of the mineral, (e) the mineral shows a morphology of crevices, i.e., tunnels with a width of ~150 nm corresponding to the collagen fibril diameter, (f) one orientation of straight demineralized collagen fibrils with the diameter of 120 nm; one fibril was pulled out and the links between the fibrils are enlarged and shown in the picture on the right top side.

along the longitudinal direction where it shows an extended plastic region; this can dissipate most energy and confers the highest (intrinsic) toughness. However, bone in the transverse direction is not designed for tensile behavior and displays a far lower toughness [72,79]. Among the collagenous materials, the alligator gar scale (mineral content: 64–67%) with the tubules through the thickness is the stiffest. Typically, in the hydrated state, the water molecules act as a "plasticizer" since hydrogen cross-link bonds form between the collagen and water molecules. Thus, the tensile response of wet gar scale displays evidence of significant "plasticity", while the hydrogen cross-links form between the collagen molecules in the dry scales [14]. The consequences of these toughening mechanisms to the mechanical behavior of collagenous materials are described in further detail in Section 4. The

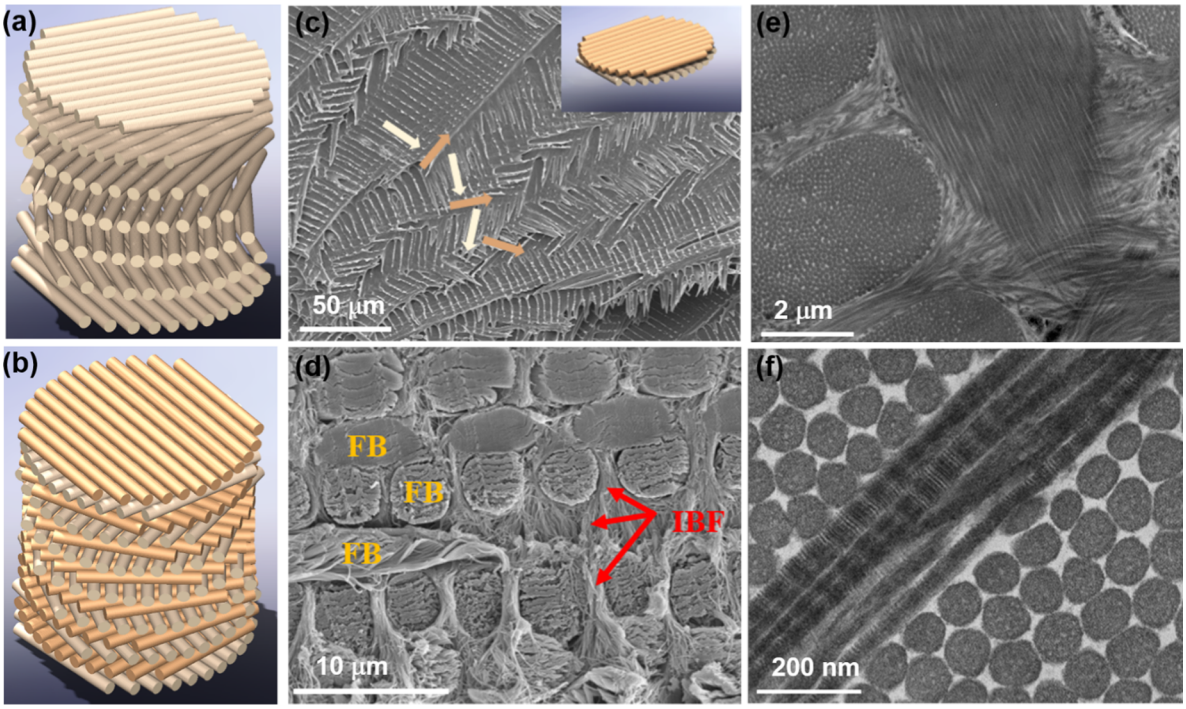

Fig. 2.13. Double Bouligand structure of coelacanth fish scales. Comparison of schematic drawings of the (a) single Bouligand and (b) double Bouligand structures, (c-e) SEM images of the double Bouligand structure in the coelacanth fish scale with the special inter-bundle fibrils, (f) TEM image of the interbundle fibrils with the fiber bundles (only circular cross-sections can be seen) [78].

arapaima fish scale, with its Bouligand-type structure having only ~15 wt% mineral content, displays a lower modulus which is close to that of the compact bone. Cancellous bone shows very low tensile ductility as it is designed for compression loading in a sandwich-like configuration; this is also discussed in more detail in Section 5. Rather than the linear response of the mineralized materials, the non-mineralized collagenous materials all display J-shape stress-strain curves with three regions (toe, heel and linear), as shown in Fig. 3.1b. The details of the J-shape at the start of the stress-strain curves will be discussed further in Section 4.1 through the example of skin. Even after demineralization, the natural armor of fish scales or the protective support of bone [81], with their well-organized hierarchical structure of straight collagen fibers, still show better tensile behavior than skin with curved collagen fibers. On the other hand, skin displays a much higher maximum strain because of the straightening of the curved collagen fibers and more sliding between the hydrated collagen fibrils under tensile loading. Both rabbit and chicken skin are expected to show a higher strength and lower maximum strain in the direction of Langer's lines.[1] However, with a multiple alignment of collagen fibers, rabbit skin fails with higher energy dissipation than the chicken skin with its woven structure [3]. Pig and human skin have similar characteristics; the maximum stress and strain are around 20–40 MPa and 0.4, respectively. These examples serve to show how nature can optimize structural architectures in many different organisms to develop specific mechanical functionalities.

3.2. *Toughness measurements of some collagenous materials*

A necessary property of the collagenous materials with the function of protection and support is the fracture toughness, which defines the resistance of structures containing flaws to crack and/or catastrophic fracture under imposed loading. Measurements of the toughness of some collagenous materials [14,72,97–99] are described below, with a focus on bone with its lamellar structure, alligator gar scales with their tubular through-thickness structure, and teleost fish scales with their Bouligand-type structures.

Koester et al. [72] examined the toughness of human cortical bone by investigating how small cracks (tens to hundreds of micrometers in size) behave as compared to long (millimeter-dimensions) in terms with how they interact with its hierarchical structure. Fig. 3.3 shows the crack-resistance or R-curves for such small (Fig. 3.3a) and larger cracks (Fig. 3.3b). The experiments were conducted by propagating cracks in the longitudinal and transverse directions using both *ex situ* testing in Hanks' Balanced Salt Solution (HBSS) and *in situ* testing in a moist environment inside the environmental scanning electron microscopy (ESEM). From this work, it was deduced that bone principally derives its toughness in two distinct ways: (i) intrinsic toughening at nano-scale by generating plasticity through such mechanisms as fibrillar sliding (which promotes ductility and the crack-initiation toughness) and (ii) extrinsic toughening at much coarser micro-scales to generate crack-tip shielding via such mechanisms as crack deflection and

[1] Langer's lines, correspond to the natural orientation of collagen fibers in the dermis of skin and determine its stiffer direction.

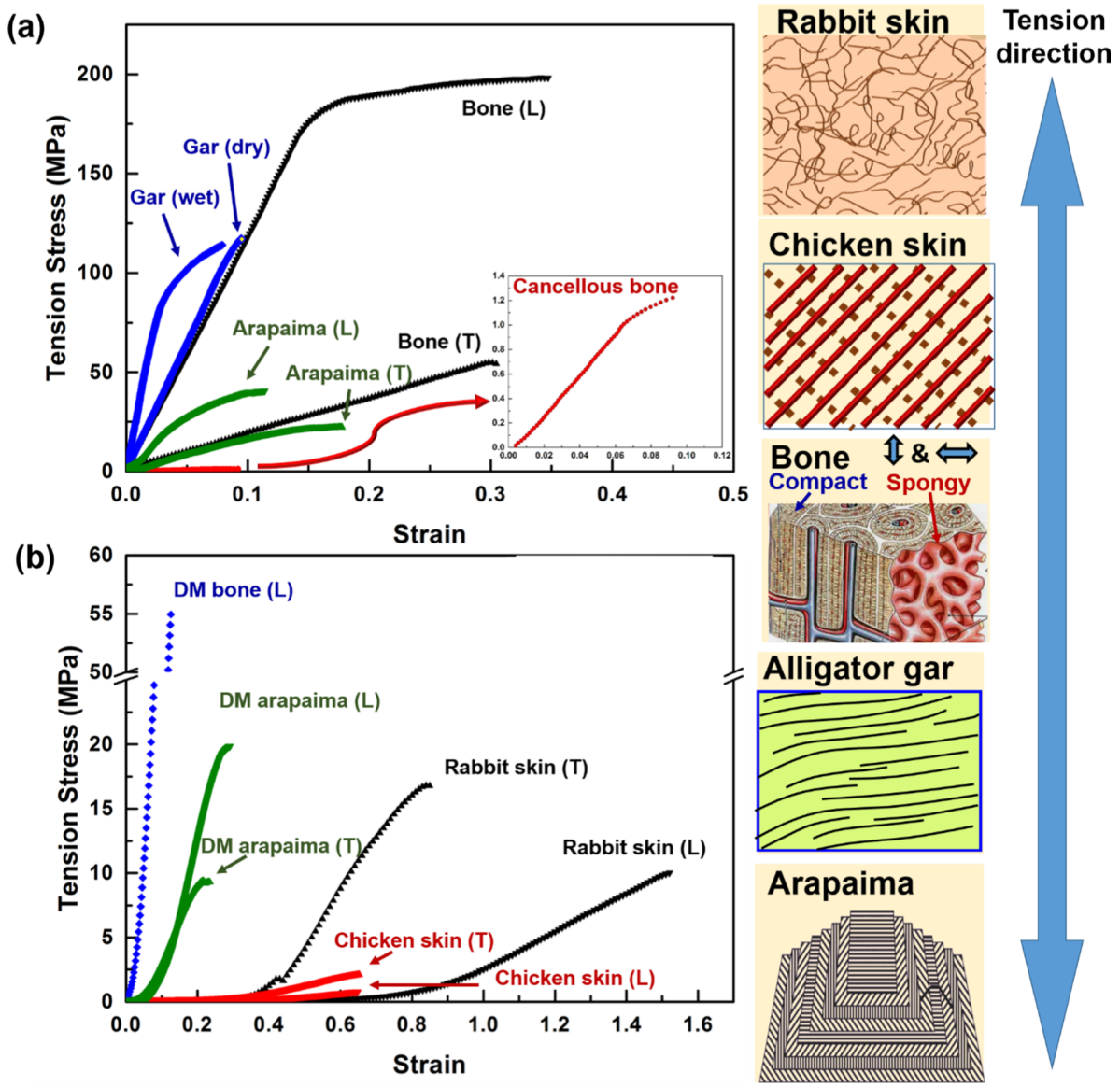

Fig. 3.1. Uniaxial tensile stress-strain curves of collagenous materials. (a) Tensile stress-strain curves of mineralized collagenous structures including lamellar compact bone in the longitudinal and transverse directions [79], porous cancellous bone (right bottom inserted plot [80]), dry and wet bony layer of the gar scale [14], Bouligand-type collagen layer of arapaima scales [73], (b) tensile stress-strain curves of non-mineralized collagenous structures including random orientations of collagen fibers in rabbit skin [3], two perpendicular orientations of collagen fibers in chicken skin, demineralized (DM) lamellar compact bone [81] and DM Bouligand-type structural collagen fiber in arapaima scales.

bridging (to promote crack-growth toughness, principally by how the path of the crack interacts with the bone-matrix structure). Due to extensive crack deflection along the mineralized cement-line boundaries of the osteons, resistance to crack growth increases much more rapidly in the transverse direction than in the longitudinal direction and can result in crack-growth toughness values exceeding 20 MPa·m$^{1/2}$. Indeed, it was found that after ~500 μm of crack extension, the driving force for crack propagation was more than five times higher in the transverse (breaking) direction than in the longitudinal (splitting) direction owing to major crack deflections and twists, principally along the cement lines.

Another type of collagenous bone structure is the bony layer of ganoid fish scales, such as alligator gar scale; its structure is shown in Fig. 2.1e. Instead of the osteons, there are tubules with diameters of ~6.5 μm aligned along the thickness direction in the inner layer, some of which are filled with collagen fibers (shown in Fig. 2.1e). Yang et al. [14] studied this tissue in detail and focused on crack propagation through, between and across, the tubules under hydrated and dehydrated conditions, as shown by the inset pictures in Fig. 3.4. Resistance to crack growth was found to be highest when the crack attempted to propagate across the tubules as well as the collagen fibers, similar to the situation in bone where cracks attempt to propagate across the osteons, *i.e.*, nominally perpendicular to the cement lines. The tubules filled with collagen might be slightly angled/tilted to the crack propagation front,

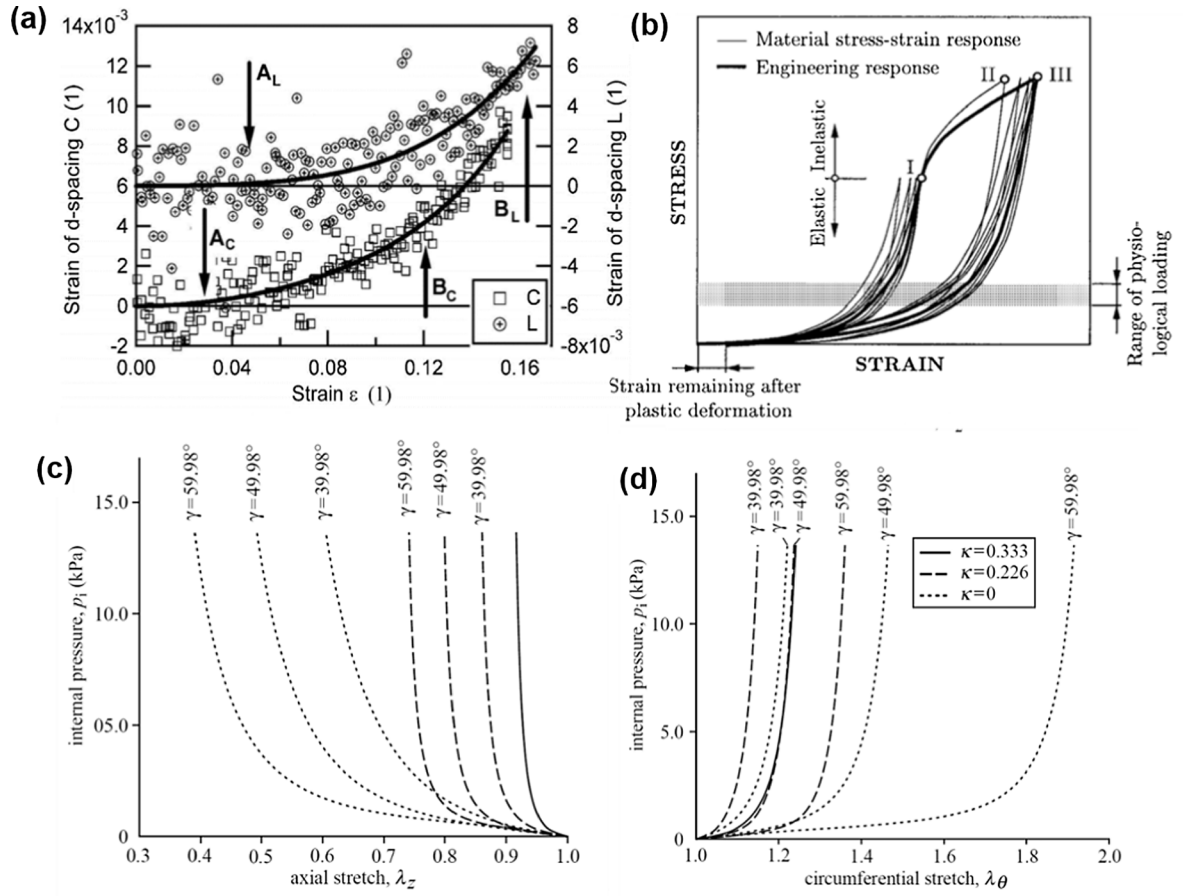

Fig. 3.2. (a) Measurements of the collagen *d*-spacing in human aortas. Increase in the *d*-spacing of collagen in human aortas is shown as function of the tensile strain under externally applied stretching in the longitudinal and circumferential directions, as determined using SAXS [82]; (b–d) Mechanical behavior of the healthy elastic artery. (b) Schematic diagram of typical uniaxial stress-strain curves for circumferential arterial strips (from the media layer) in passive condition: cyclic loading and unloading, associated with stress-softening effects [45], (c and d) the response of the artery in the axial and circumferential directions, while applying internal pressure with different arrangement of collagen, as a function of the parameters of γ and κ for the model developed by Gasser et al. [83].

which can lead to the difference in resistance to crack growth, as shown by changes in the slope of the fracture toughness crack-resistance R-curves.

Dastjerdi and Barthelat [97] designed a method to measure the toughness of teleost fish scale which also displays a Bouligand-type structure. With the low mineral content, the collagen fibrils are pulled out at the tip of the notch during tensile testing, as shown in Fig. 3.5a. Due to the blunting, defibrillation and massive inelastic deformation, it is believed that the inelastic region spreads across the entire scale ahead of the notch before or shortly after crack propagation occurs, making the numerical measurements of the toughness of the scale somewhat questionable. As the crack opens, the fibers stretch and also continue to delaminate from the crack face as shown by the insert picture in Fig. 3.5b. Using the so-called Kendall model [100], a delaminated fiber angle θ as a function of non-dimensional parameter $J_i/E_f\, d$ was calculated; the geometry is shown in insert. θ, J_i, E_f and d represent the angle of the delaminated fiber from the scale, toughness of the interface (between fibers), modulus of fiber and the assumed square cross-section side, respectively. Stiff fibers and weak interfaces (low $J_i/E_f d$) lead to long delamination distance but small delamination angle with little deformation in the fiber. However, a fish scale with soft collagen fibers (low mineral content) bonded by tough interfaces can lead to a high delamination angle but short delamination distance which means that under a large crack opening, the fibers still have a large distance to develop full delamination [97]. Although this is a clever means to measure the toughness of such flexible collagenous fish scales, the loading rig imparts unrealistic constraints on the loading system, thereby making the toughness results quantitatively somewhat artificial. This testing geometry is shown in Fig. 3.5a. However, the experiments clearly demonstrate that the Bouligand structure enhances the stiffness by impeding the crack from propagating, as shown by the schematic diagram in Fig. 3.5b and the nonlinear-elastic fracture toughness J_c values in Fig. 3.5. An improved technique with less constraints on the upper and lower surfaces, applied to the scales of arapaima fish scales. With such improved grips, the fish scales can be constrained to be rotated in the same plane with a free-rotating fixture (Fig. 3.6a).

Besides toughness measurements, the tear resistance of elasmoid carp scales along with the effects of the location of the scales and

Table 3.1
Mechanical properties of some collagenous materials.

Collagenous materials	Structure	Loading direction	Mineral content	Young's modulus (GPa)	Strength (MPa)	tCrack-initiation toughness (MPa·m$^{1/2}$)
Rabbit skin	Random aligned collagen		None	0–0.05 [3]	8–17 [3]	–
Chicken skin	Waven		None	0–0.008	0.5–2	–
Compact bone	Lamellar mineralized collagen	Longitudinal Transverse	86–97% [84]	11–12 [79] 2.5 [79]	140–250 [79] 25–50 [79]	2.0–7.0 [85–91] 6.5 [89]
Whole femurs	Shaft of the femur	Transverse (bending)		3.44 ± 0.68 [91]	158 ± 23 [91]	2.16–2.89 [91]
DM compact bone	DM lamellar collagen		None	0.21–0.75 [81,92–95]	7–55 [81,92–95]	–
Alligator gar fish scale	Collagen fibers aligning along thickness approximately	Perpendicular to collagen	64–67%	1.8–3.1 (dry) [14] 1.9–3.8 (Wet) [14]	72–132 (dry) [14] 85–120 (wet) [14]	2.5–5 [14] 2.2–6 [14]
Arapaima fish scale (entire scale)	Bouligand structure + mineral layer	Longitudinal Transverse	44–60%	0.86 ± 0.32 [15] 0.21 ± 0.02 [15]	23.6 ± 7.2 [15] 14.2 ± 1.1 [15]	– –
Arapaima (collagen layer)	Bouligand structure	Longitudinal Transverse	15%	0.47 ± 0.25 [15] 0.21 ± 0.03 [15]	36.9 ± 7.4 [15] 21.8 ± 2.4 [15]	– –
DM collagen layer of arapaima scale	Bouligand structure	Longitudinal Transverse	none	1.1–1.4 0.6–1.1	18–21 8–13	–
Striped bass scale Collagen layer of striped bass scale		0, 45, 90°	— —	0.7 [96] 0.45	44 62	3.2–3.5* [97] 4.2* [97]

* Data was calculated using the mode I *K-J* equivalence relationship: $K_c = (J_c \cdot E)^{1/2}$.

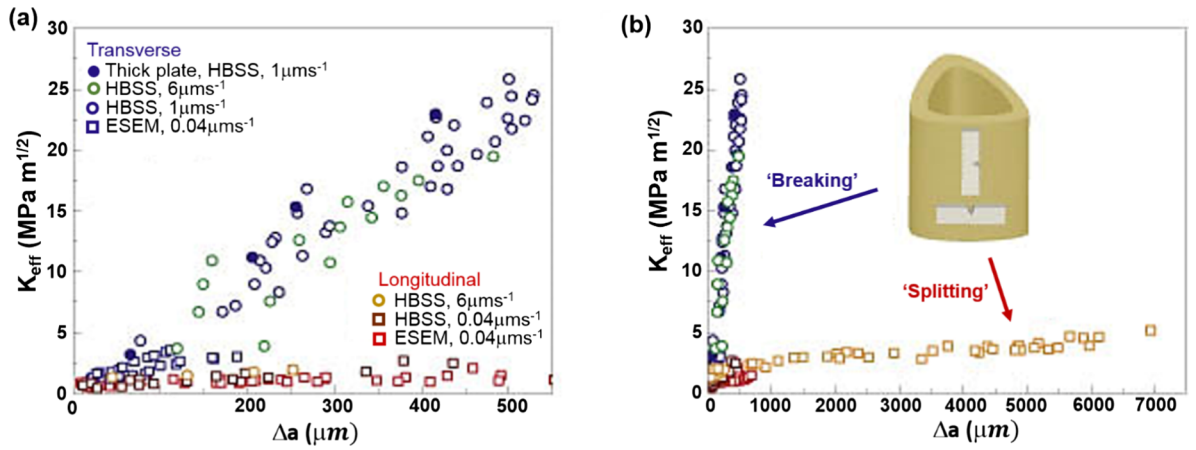

Fig. 3.3. Toughness of human bone as a function of crack growth Δa; showing R-curve response (increase in fracture toughness with subcritical crack extension Δ*a*) for the transverse and longitudinal orientations (a) for physiologically-short crack lengths (Δ*a* < 550 μm) and (b) for longer cracks (Δ*a* < 7000 μm). Both *in situ* results, obtained from the tests in an environmental SEM, and *ex situ* results, obtained from testing in Hanks' Balanced Salt Solution (HBSS), are included in the plots; individual displacement rates are a given in the top left-hand side. The inset shows the orientation of the samples from the humerus. It is apparent that bone is markedly tougher in the transverse ("breaking") direction, as compared to the longitudinal ("splitting") direction [72].

temperature has been documented studied by Murcia et al., [101]. The scales close to the fish head required significantly greater energy to tear than the ones on the middle and tail of the fish (Fig. 3.6b). This high fracture toughness is a hallmark of the Bouligand structure. It is very difficult for a crack to propagate through the structure because each layer is anisotropic with a different directional crack resistance.

As described in Section 2, the coelacanth fish scale comprising a double-twisted Bouligand structure with interbundle fibrils shows quite different crack-resistance mechanisms, with the interbundle fibrils tending to constrain the fibers in different orientations under load [78]. Fig. 3.7 shows the evolution of fiber rearrangement during the propagation of a crack, which involves adaptation structural reorientation under load. Initially, the crack tip opens and blunts readily, but with further loading, collagen fiber (bundle) tend to rotate leading eventually to pull-out and delamination of the fibers.

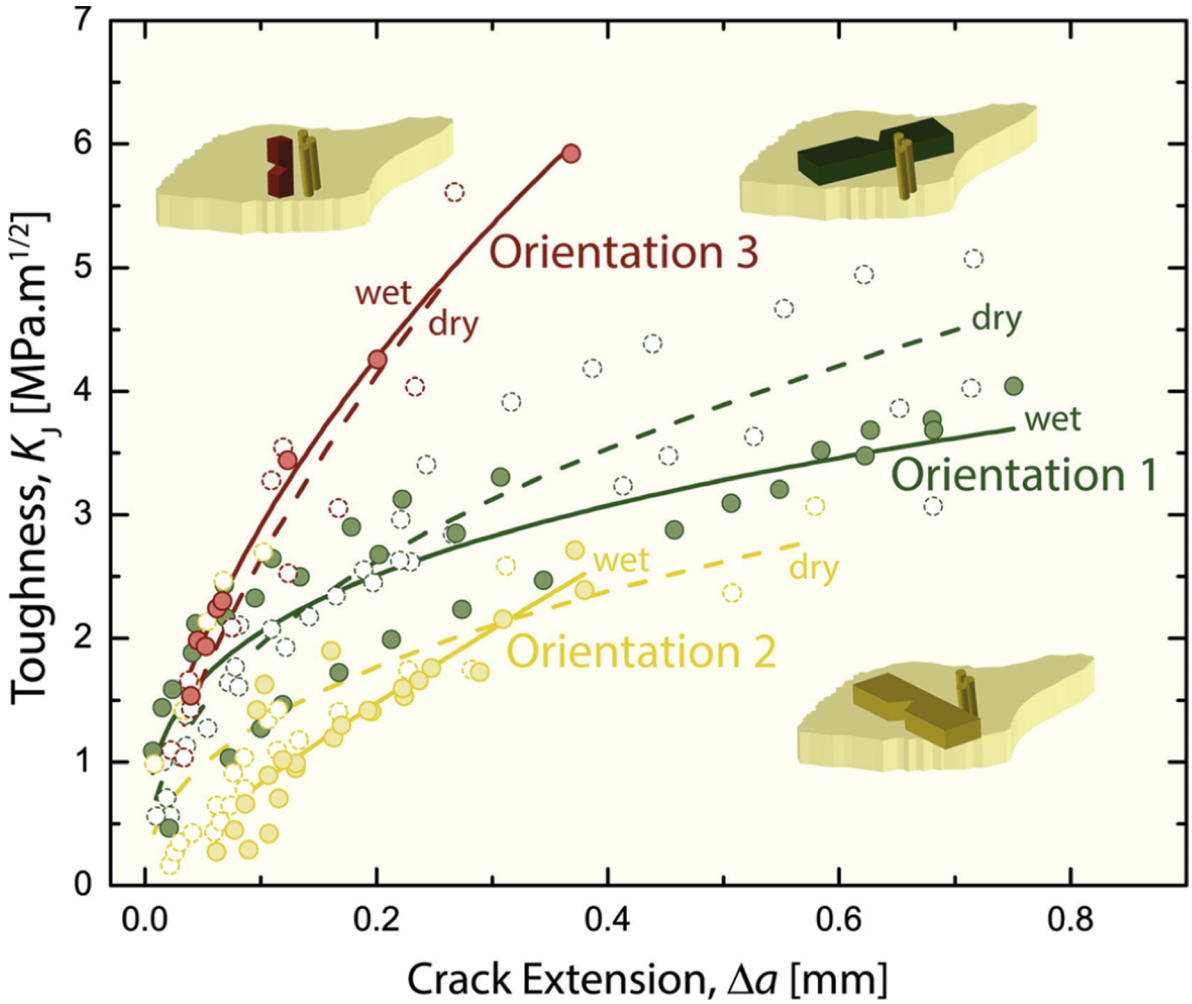

Fig. 3.4. Fracture toughness of alligator gar fish scales; tested on notched three-point bending samples in the environmental scanning electron microscopy exhibiting increasing crack-resistance behavior with increasing Δa (R-curve behavior). R-curves show the fracture resistance in terms of fracture toughness, as a function of crack extension. Testing of the scales was performed both in moist (water) and dry (weak vacuum) environments with three different directions of crack orientation with respect to the scale's structure [14].

3.3. Summary of mechanical properties of collagenous materials

Table 3.1 summarizes the mechanical properties of these natural collagenous materials, with the importance of mineral content highlighted by demineralizing some of the specimens. Among the mineralized collagenous materials, the toughness of bone (*e.g.*, compact bone and the boney layer in gar scale) is similar to that of the fish scale of the striped bass with its Bouligand structure, although bone displays a much higher modulus (2–12 GPa) than that of the Bouligand structure (0.2–0.7 GPa). In these natural materials, the structure with the higher mineral content will invariably be stiffer and stronger. Interestingly though, in the absence of their mineral content, the demineralized arapaima and striped bass fish scale samples exhibit higher strength than demineralized bone and skin, which suggests that their collagenous Bouligand structure is crucial to the development of their damage-tolerant mechanical properties. The toughness *vs*. modulus Ashby plot for biological materials, shown in Fig. 3.8 [97], confirms that the highly mineralized collagenous materials, such as bone and gar fish scales, show a higher modulus, although increasing the orientations of collagen fibers within a structure appears to confer even higher toughness in such materials.

4. Toughening mechanisms in architectured collagenous materials

We have shown above that by varying mineral content, collagenous materials can have different hardness, elastic modulus, and toughness/tear resistance, which is the process used in nature to confer specific mechanical functionality. For example, in skin and tendons, internal energy dissipaters are employed as a means of absorption; the inner layers of many fish scales tend to be less mineralized than the more mineralized outer surface to provide resistance to penetration from predator attacks supported by a softer,

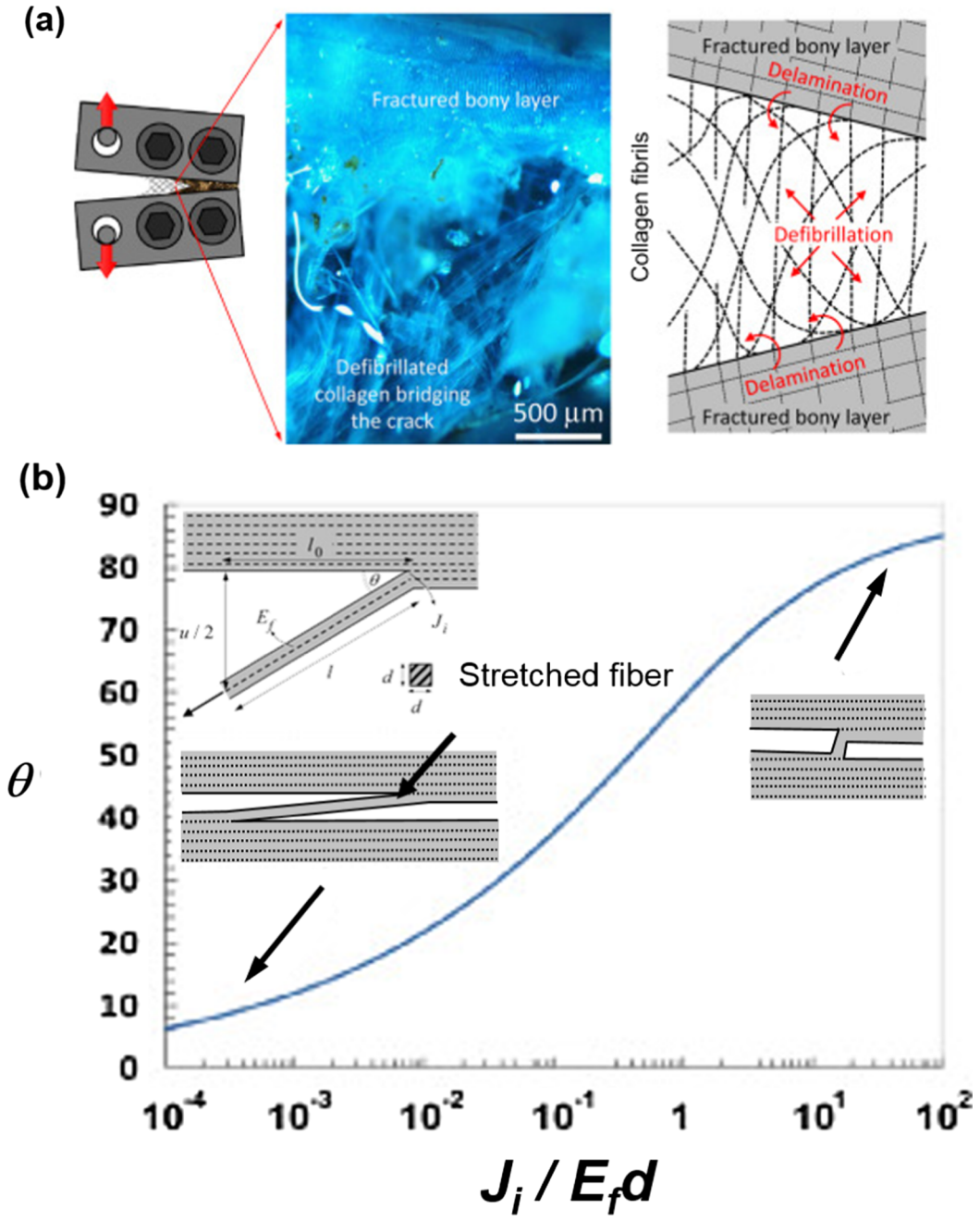

Fig. 3.5. Toughness behavior of teleost fish scales. (a) Toughness tests on the teleost scales, the optical image shows the fractured bony layer with the fibers defibrated and delaminated; the schematic drawing on the right shows the pattern of the defibrillation and delamination during crack opening. (b) Delaminated fiber angle as a function of non-dimensional toughness parameter $J_i/E_f\,d$; the top left inserted picture shows the diagram used to develop the mechanical model [97]. J_i is the nonlinear elastic fracture toughness of the interface between the layers, E_f is the modulus of the fiber, d is the size (diameter) of the fiber, and θ is the angle that the fiber was pulled away from the original position, l and l_o indicate the length of the fiber and the reflected length of the fiber on the layers, respectively.

tougher inner layer that absorbs the extra energy through deformation. All these various mechanical functions are the result of hierarchical collagenous constructions of varying shape, size, form, and degree of mineralization, which elicit different toughening mechanisms. These mechanisms provide a fascinating palette for engineers to design new synthetic materials with broad combinations of mechanical properties. Here we illustrate some of the more potent toughening mechanisms active in collagenous materials.

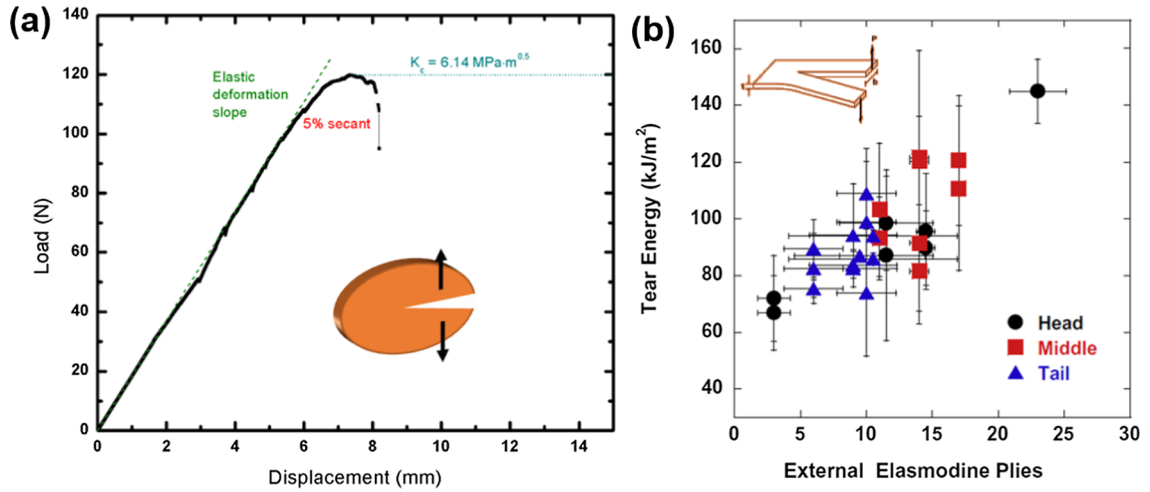

Fig. 3.6. Fracture behavior of fish scales. (a) Fracture toughness of the arapaima fish scale (courtesy H.C. Quan) and (b) tear resistance of carp scale (*cyprinus carpio*) [101].

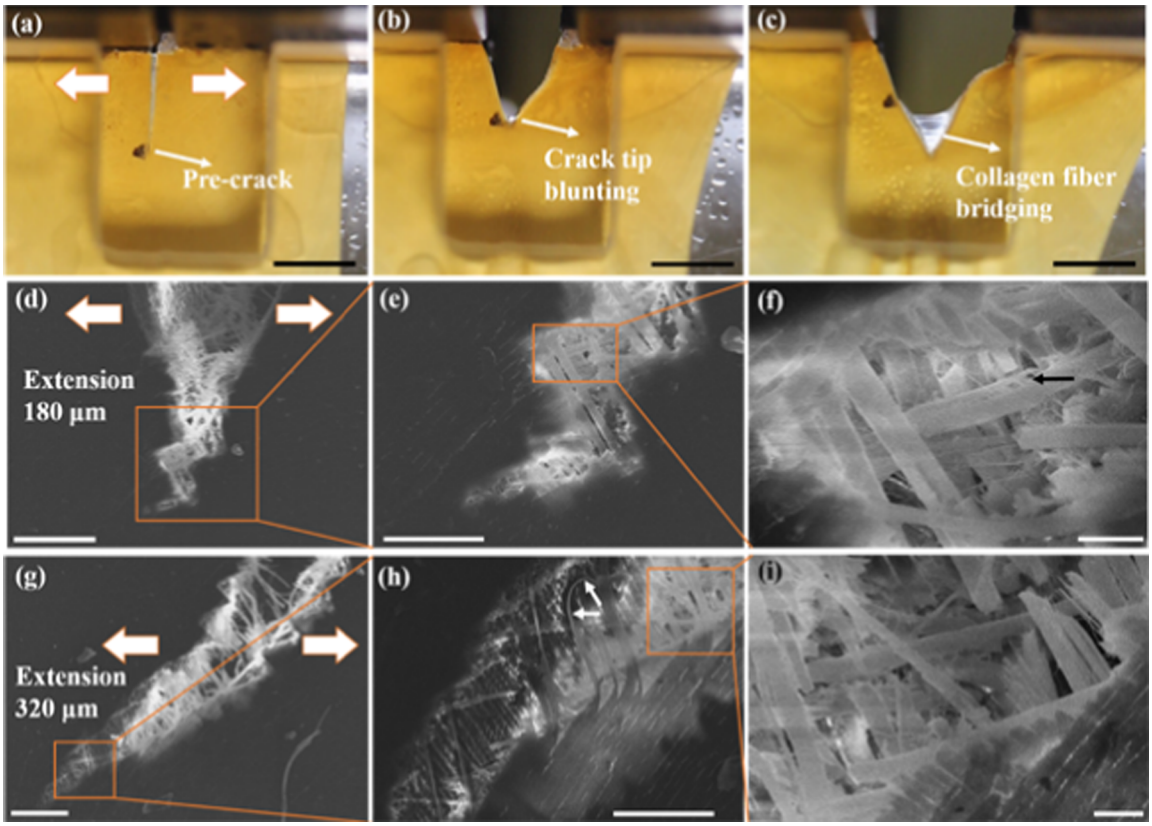

Fig. 3.7. *In situ* sequence of images during the loading of a pre-cracked sample of a coelacanth fish scale. (a–c) observation of the crack opening by optical microscopy, detailed structure on the crack tip and crack propagation observed by *in situ* SEM at crack extensions of 180 μm (d–f) and 320 μm (g–i) [78].

4.1. Skin: Rabbit, chicken, frog, rhinoceros, pig, and human

Yang et al. [3] mechanistically quantified the extreme tear resistance of skin and identified the underlying structural features which lead to the sophisticated failure mechanisms. The structural change of the skin under stretching was examined by the small-angle X-ray scattering (SAXS) in X-ray synchrotron beamline experiments. A typical tensile stress-strain curve of rabbit skin is shown in Fig. 4.1e representing the toe, heel, linear and failure stages (shown by dashed line); the black square data points are examined by

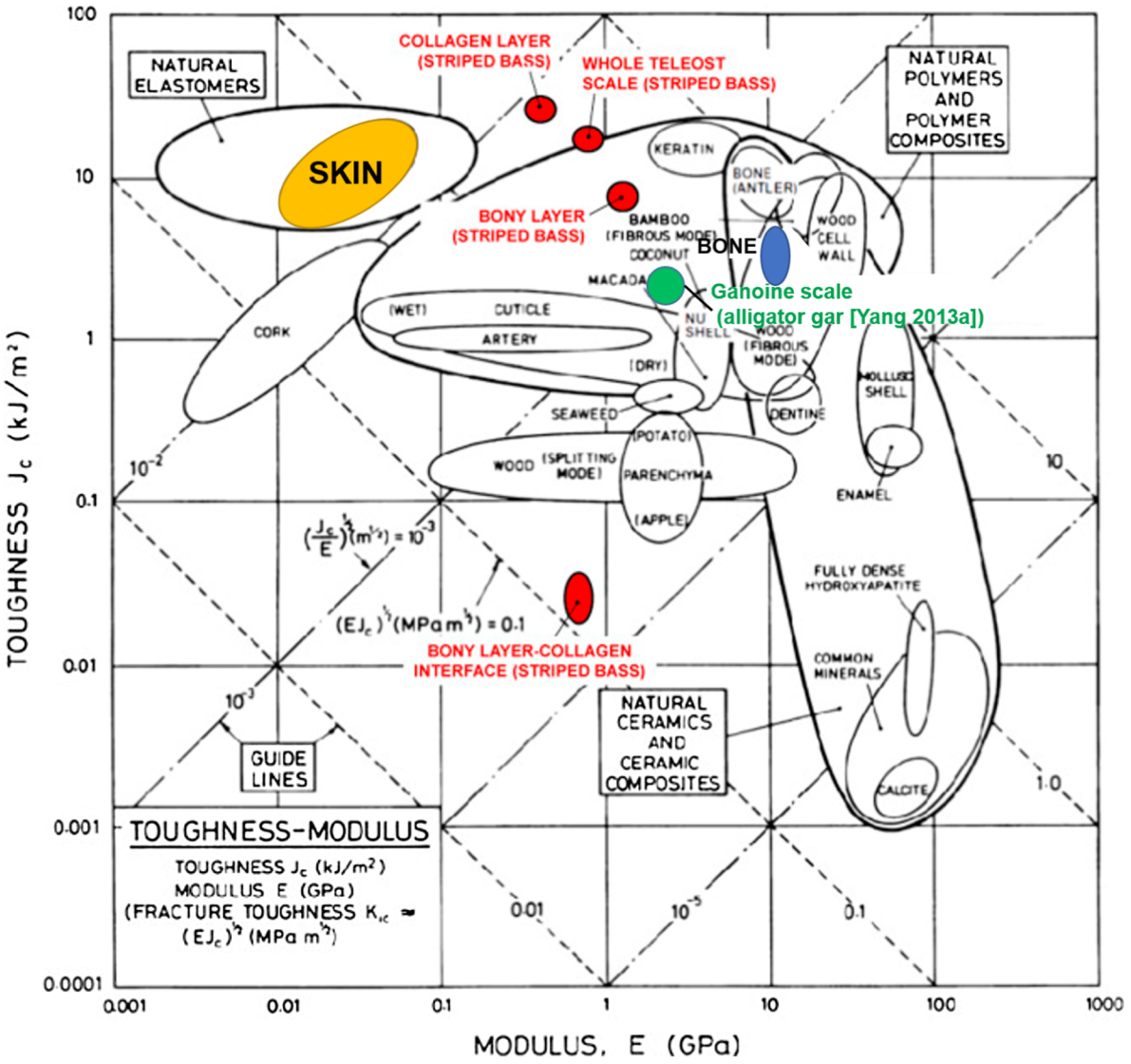

Fig. 3.8. Toughness-elastic modulus Ashby plot for biological (natural) materials. The properties of skin (yellow), bone (blue), gar scale (green), and the striped bass (red) are shown in the chart (modified from Ref. [97]). Different collagenous materials display different mechanical properties depending upon their multiple length-scale structures which induce different mechanisms of elasticity and plasticity, leading to differing stiffness, strength, ductility and toughness.

X-rays, with four of the data points selected and shown in Fig. 4.1a–d. The arcs in diffraction patterns show the orientations of collagen fibrils with the images of the sample during tensile testing in the top-right corners. Detailed analysis of the variation in SAXS peak intensity, orientation angle, *d*-spacing and full-width-at-half-maximum (FWHM) from the four SAXS patterns (Fig. 4.1a–d) are shown in Fig. 4.1f and g. The collagen fibrils rotate towards the tensile direction with gradually increased intensity (which means more collagen fibrils align in the tension direction) until the maximum stress is reached (Fig. 4.1f); it is possible to measure the local strains because as the collagen fibrils get stretched the *d*-spacing is increased. In the linear stage (III), the collagen fibril extends to a strain of 0.037 (from 64.5 to 66.9 nm); however, in this stage, the total (global) strain in the skin is an order of magnitude higher (~0.5) meaning that deformation must be occurring primarily by mechanisms of inter- and intra-fibrillar sliding to accommodate the imposed strain. Fig. 4.2 shows the schematic images of the phenomena occurring in the skin at different stages during its stretching, as analyzed from the SAXS data. Several mechanisms participate while the skin being stretched including rotation (Fig. 4.2a), straightening (Fig. 4.2b) as well as stretching, sliding and delamination (Fig. 4.2c) of the initially curvy collagen fibrils. The delamination of collagen fibrils is consistent with the SAXS peaks becoming broader. The FWHM increases (Fig. 4.1g) owing to defects introduced into the previously well-ordered fibrils. At the end of the test (Stage IV in Fig. 4.1f and g), an increasing proportion of collagen fibrils have fractured and curled back (in Fig. 4.2d) with a decreasing *d*-spacing, due to fracture of the collagen fibrils, which then increases again due to their relaxation and recovery. These multiple mechanisms of collagen including fibril straightening,

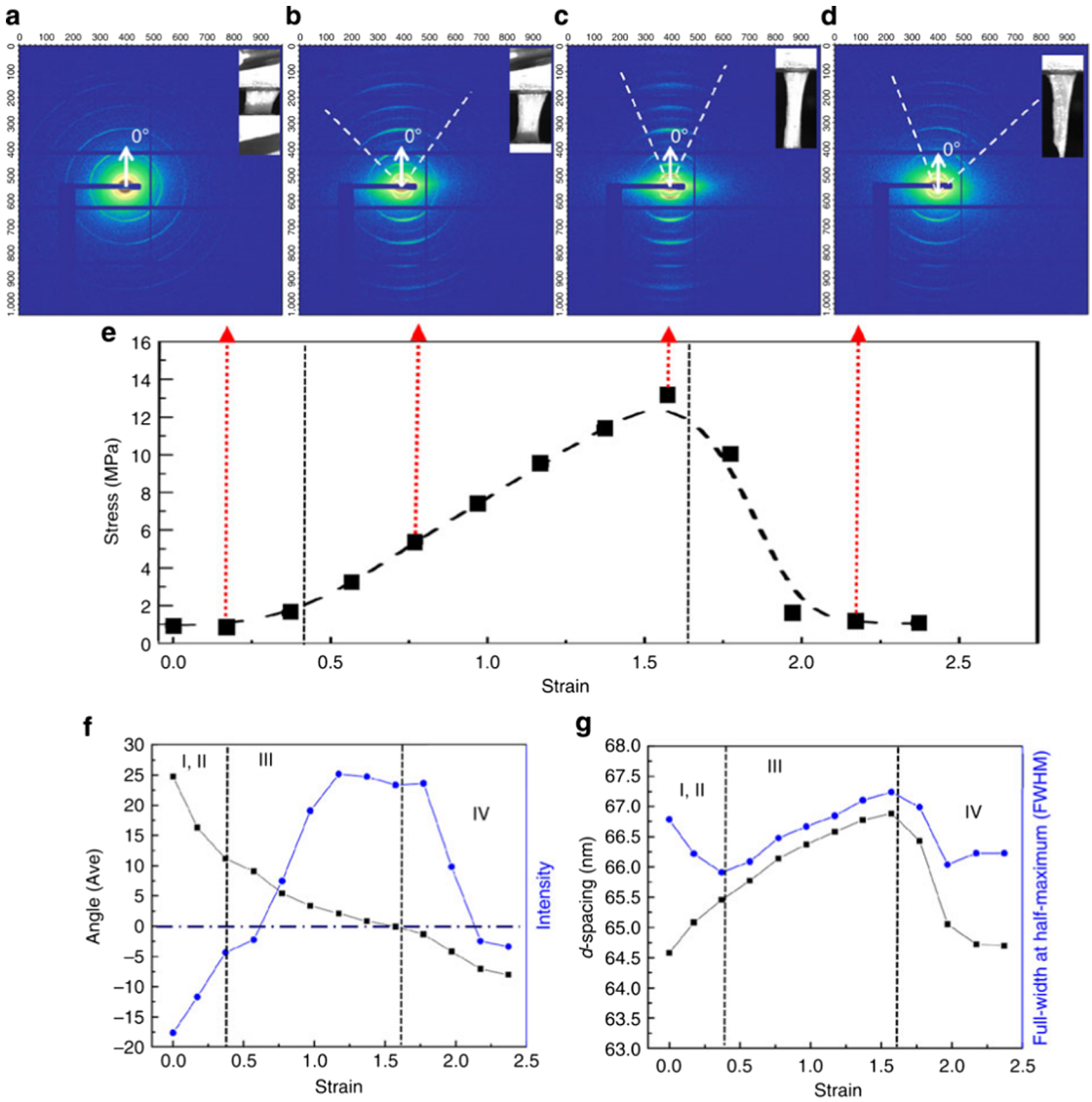

Fig. 4.1. Small angle X-ray scattering patterns of rabbit skin, taken during *in situ* uniaxial tensile testing, showing the variation in the intensity, orientation (angle), *d*-spacing (stretching) and full-width-at-half-maximum (FWHM) of the collagen fibrils with strain in the skin [3]. (a–d) Diffraction patterns: the position and the radius of the first arcs from the center show the orientations (angle range) and the stretching of the fibrils, images of the sample shown at top-right corners, (a) collagen fibrils randomly oriented to tensile axis result in constant intensity of diffraction pattern, forming continuous circles, (b) fibrils gradually align in tension direction, (c) fibrils aligned along tensile axis, (d) fibrils fractured and relaxed. (e) Tensile test curve with 13 data points (black dots); four stages of deformation were identified. (f) The orientation of the collagen fibrils (measured from the tensile axis) *versus* intensity of fibrils (blue dots) as a function of strain, and (g) *d*-spacing (black dots) and full-width half-maximum (FWHM) (blue dots) of fibrils as a function of strain.

reorienting, stretching, and delaminating provide a particularly potent sequence for toughening, specifically energy absorbing, mechanisms which serve to induce the remarkable tear resistance, and hence toughness, of skin.

Similar to the property change of dehydrated collagen fibril described in Section 1.2, when the skin gets dehydrated, its stiffness dramatically increases [3]. Water molecules between the collagen enable the smooth sliding between the collagen fibrils and increase the elasticity and ductility (Fig. 4.3). The loss of the water content makes skin a rubber-like material; as such, without the water molecules, the direct sliding between collagen fibrils becomes highly limited.

A summary of the tensile stress-strain plots is shown in Fig. 4.4. Since the tensile property of the skin varies according to the location and orientation of the samples in the body, scatter-band curves are shown to reveal the property trends of the skin from different animals [3,56,102,103]. Interestingly, despite the orientations and locations of the skin samples taken from the animals' bodies, we find that the stiffness and strength of the skin are higher as the size of the animals increases. This is probably associated with body weight since the skin is the largest organ to protect the internal organs in the bodies.

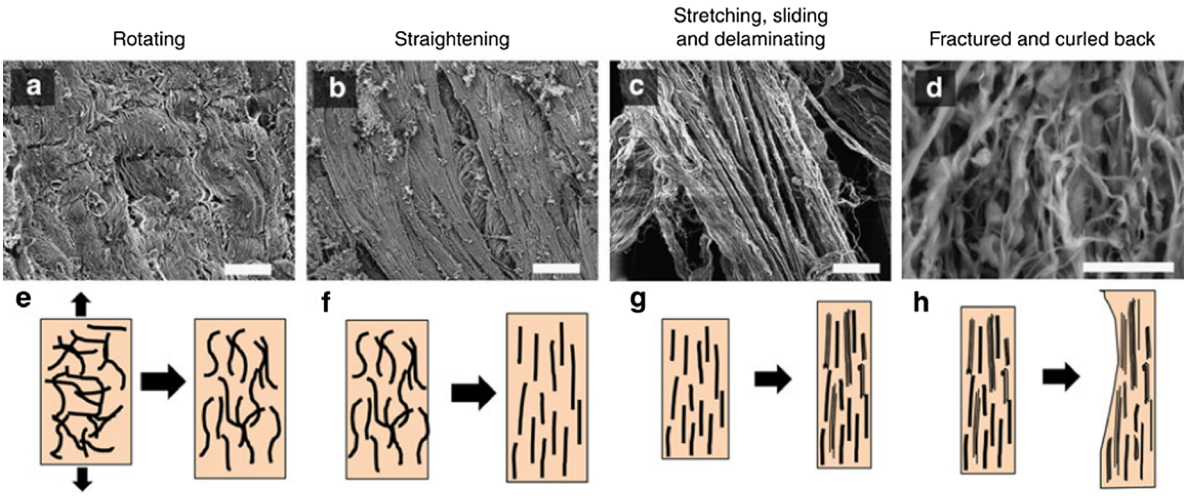

Fig. 4.2. Tensile deformation of rabbit skin. SEM images (a–d) and schematic drawings (e–h) of the four mechanisms of deformation during tensile loading of rabbit skin; black arrows in (e) represent the direction of tension testing. (a and e) Curved collagen fibrils are oriented along the tensile axis; (b and f) collagen fibrils straighten, larger and larger amount of the fibrils reorient and align with the tensile axis; (c and g) collagen fibrils stretch, slide, delaminate and reorientate completely with the tensile axis; (d and h) collagen fibrils fractured and curl back. Scale bars in (a–d): 20, 20, 20, 50 μm, respectively [3].

4.2. Tendon and ligaments

The stress-strain response of a ligament is shown in Fig. 4.5 [104]. There are four recognized stages: toe, heel, linear and failure, which are marked in plot. Tendons have similar response with the maximum strain determined by the crimping structure. The mechanical response of skin is also similar, except that the strength is considerably higher in ligaments by virtue of the alignment of the collagen fibers. All fibers are stretched and aligned in the tension direction, in contrast to skin and elasmoid scale, where only a fraction of the collagen fibers is aligned with the tensile direction and significant rotation, shear and sliding take place. Fig. 4.5c shows how the organization of the collagen fibers is destroyed in an anterior cruciate ligament upon failure; the fibers separate and, once failure occurs, spring back into a disorganized arrangement.

4.3. Bone and ganoid (bony) fish scales

As described in Section 2, bone has numerous structural features which can contribute to its toughness; these include the osteons, mineralized collagen fibers, mineral at several hierarchical levels, and even the process of microcracking as a mechanism of inelasticity. Deformation of the mineralized collagen fibrils toughens bone tissue by forming plastic zones around crack-like defects [11]; such deformation involves the stretching and sliding of collagen fibrils (fibrillar sliding) and is one prime origin of plasticity and ductility in bone. At coarser, micrometer-scale dimensions though, toughness in bone can arise through extrinsic mechanisms that impede the extension of cracks (Fig. 4.6). The most notable example is when a crack encounters a weak interface in its path, causing it to deflect from the plane of maximum tensile stress and often delaminate along this interface. As noted above, this is a frequent occurrence for cracks propagating in human cortical bone in the transverse direction when they encounter osteons; the more mineralized osteonal interfaces (cement lines) then provide a preferred deflected crack path. Indeed, such deflections, and more potent twists, of the crack path can serve to elevate the toughness by a factor of two or more (Fig. 4.6a). Constrained microcracking can also increase the toughness by dilating a region around a developing macroscopic crack, which compresses the crack; this mechanism though has only a small effect in shielding the crack from the applied stresses ($\sim 0.05\ \mathrm{MPa{\cdot}m^{1/2}}$) but is important as it results in several other phenomena which are critical to the health of the bone. It is thought that the microcracks can signal the remodeling of bone, by severing the canaliculi which act as “communication links” between the osteocytes; moreover, the presence of a zone of microcracks ahead of a growing crack tip can lead to the creation of uncracked-ligament bridges which can carry load that otherwise would be used to propagate the crack. Additionally, many of the microcracks themselves can be bridged by collagen fibrils which span their surfaces (Fig. 4.6d); this again represents a relatively small shielding effect for an isolated microcrack ($\sim 0.1\ \mathrm{MPa{\cdot}m^{1/2}}$) but taken cumulatively for an array of microcracks can have a significant effect in restraining the microcrack damage from converting into a macrocrack in the bone.

In comparison to bone, alligator gar scales employ much simpler mechanisms to enhance their resistance to fracture. As the alligator gar scale only contains mineralized collagen fibers, tubules as well as the mineral matrix, the crack generally will propagate across the tubules in dry fish scale (Fig. 4.7a and c), whereas in the more realistic wet gar scales, cracks generally propagate in a relatively undeflected manner (Fig. 4.7b and d). Here the mechanism of toughening has a larger intrinsic character. Specifically, the presence of water acts as a “plasticizer” by forming hydrogen bonds between the collagen and water molecules; this results in fibrillar sliding of the collagen fibrils which provides source of “plasticity” in the tissue, hence generating some measure of ductility.

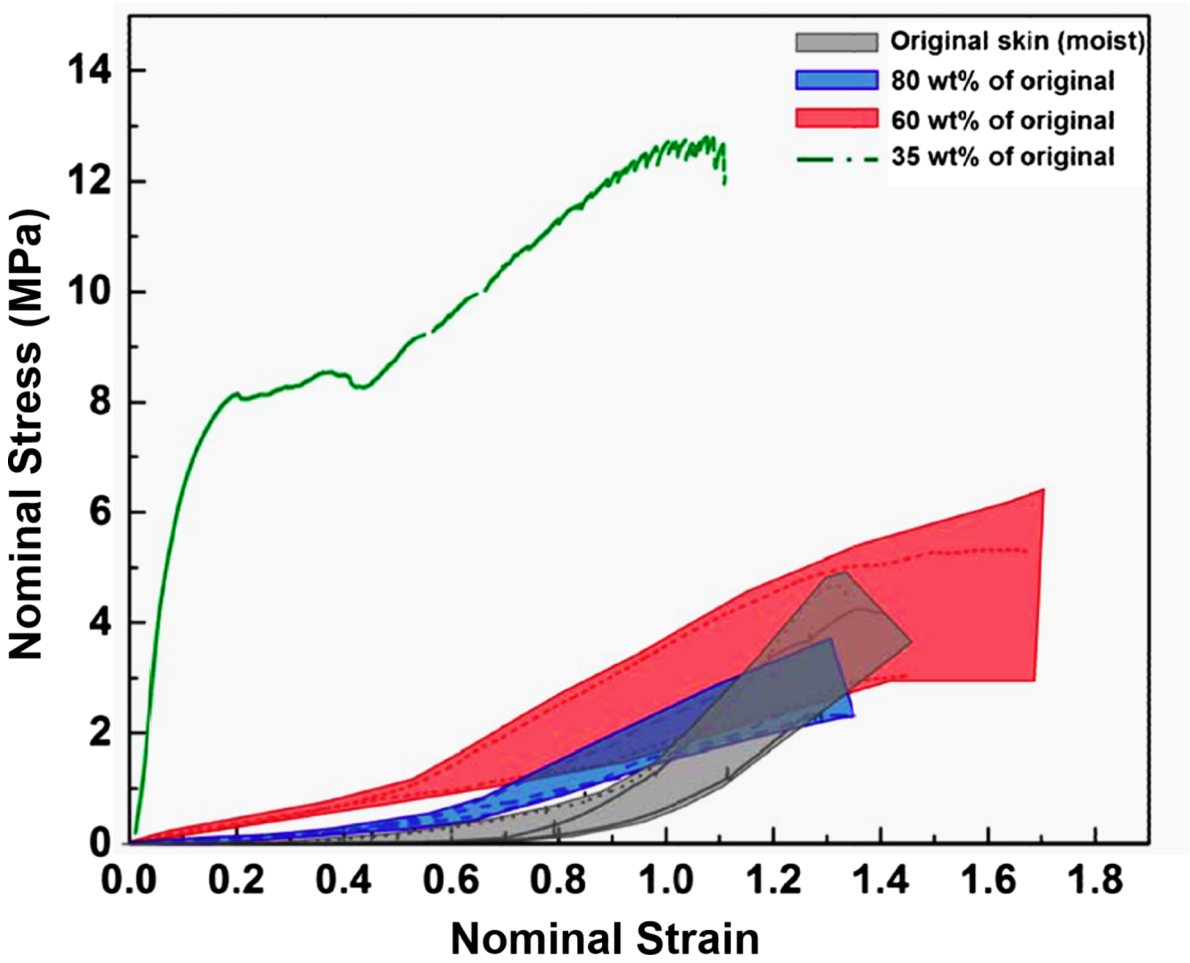

Fig. 4.3. Mechanical response rabbit of skin, as a function of hydration. The grey curve band shows the stress-strain behavior of fresh skin; as the skin loses water, the weight of the collagen decreases, and it becomes gradually stiffer. The stress-strain curves of the skin shown correspond to water contents of 80%, 60% and 35 wt% of fresh skin (from Yang et al. [3]).

4.4. Gradient formation: Fish skin and elasmoid scales

Elasmoid scales can be more flexible than ganoid (bony) fish scales, because from fish skin to the outer layer of elasmoid scale, there is a complete protective gradient structural system. Szewciw and Barthelat [105] recently studied the fish skin and showed that it contains a cross-lamellar arrangement of collagen fibers, as shown in Fig. 4.8. The collagen fibers in the skin are also curvy and have a 24–31% straightening strain.

It is interesting that the tensile strength of fish scales without the external highly mineralized layer is higher than the intact scale. This was first observed by Yang et al. [15] and later confirmed by Sherman et al. [106] and Liu et al. [107]. This is counterintuitive because the mineral provides additional resistance to penetration. However, the mineral operates optimally under compression and has a much lower tensile than compressive strength. Therefore, it contributes little to the tensile strength. The tensile strength of the composite with a mineral-rich surface is therefore lowered by the mineral. Cracks readily develop when the full scale is stretched in tension. Fig. 4.9 shows these differences for arapaima (Fig. 4.9a) and carp (Fig. 4.9b) fish. The dashed lines in both plots represent the response of the collagenous layer alone and are above those of the equivalent full scale containing the mineral plus collagenous layer.

Zimmerman et al. [75] investigated the toughening mechanisms in the fish scales of the *Arapaima gigas*, the large fish found in Amazon waters, specifically by examining the scales during *in situ* tensile testing in the X-ray synchrotron using SAXS. Thirteen small-angle X-ray diffraction measurements were taken until the sample exhibited a linear curve up to a strain of 0.1 (Fig. 4.10b). Five representative SAXS patterns taken during the tensile testing are shown in Fig. 4.10a. Similar to that seen in the skin measurements (Fig. 4.1e), the arcs represent the orientations of the collagen fibrils. Typically, two groups of orientations of collagen fibers, one of which aligns close to the tensile direction (orientations from i to v) and the other forming a large angle with the tensile direction (orientations from I to V), were investigated. The plot of the integrated intensity *vs*. the distance q from the center of SAXS pattern (q is equal to $2\pi/d$, where d is the collagen characteristic d-spacing) illustrates that the collagen fibrils close to the tensile direction are stretched and aligned or rotated towards the tensile direction, while the ones away from tensile direction delaminate or separate (see

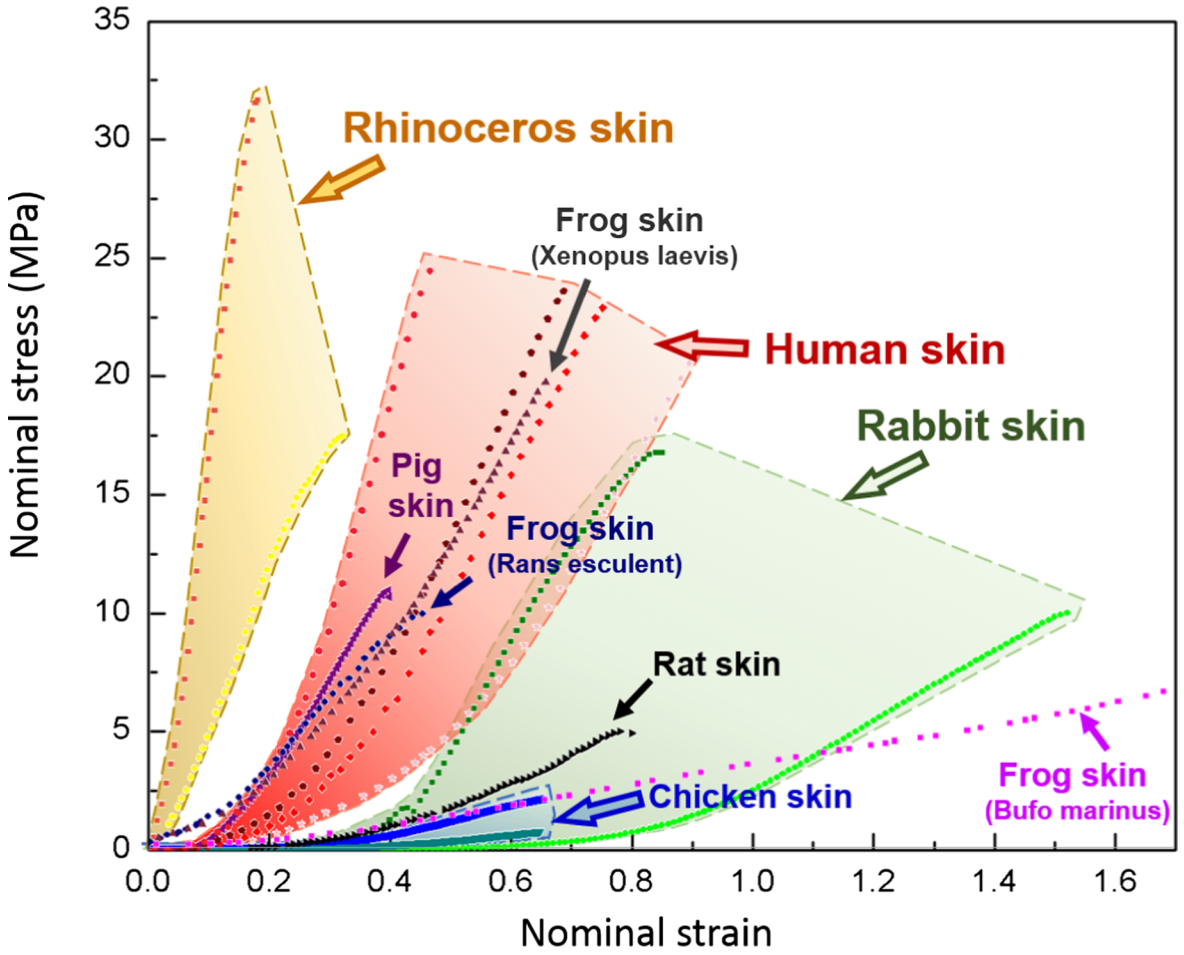

Fig. 4.4. Uniaxial tensile stress-strain curves of skin samples from different animals. Data are shown for the skin of rhinoceros [56], humans [103], pig and rabbit [3], rat [102], frog skin [57] and chicken.

inset of Fig. 4.10c); the latter is apparent in the images as the arcs become dimmer (decreasing intensity) and essentially disappear. Fig. 4.11 summarizes these four mechanisms of adaptive structural reorientation observed during the tensile testing of these arapaima fish scales: rotation, stretching, tensile opening and sympathetic lamella rotation. The collagen fibrils close to the tensile direction rotate towards the tensile direction through interfibrillar shear and get stretched. The rotation of the collagen away from the tensile direction is due to gaps opening between the collagen fibrils, thereby increasing the angle from ψ_0 to ψ_1, in one half of the tear. These angles, shown in Fig. 4.11c, represent the rotation associated with the separation of the collagen layers; ψ_1 and ψ_2 result from the splitting. By rotating towards the tensile direction of loading, the collagen fibrils are able to carry more of the load applied to the fish scale; this active mechanism provides a means by which nature effectively enhances the fracture resistance of the scale.

4.5. Comparison and summary of mineralized and non-mineralized collagenous materials

The toughening mechanisms active in collagenous materials can be summarized according to whether the tissue is non-mineralized (or with low mineral content) or is highly mineralized. Fig. 4.12a illustrates the toughening mechanisms in skin [108]. Since the collagen fibers are curvy and have multiple orientations, while being stretched the fibers rotate toward the tensile direction and straighten. During this stage, the strain in the fibers increases but with minimal increase in stress; subsequently, the collagen fibers experience stretching, rotation, sliding and delamination. This corresponds to the linear region. A crack will not initially propagate in skin because it becomes blunt from the excessive inelasticity created by the stretching and re-alignment of the collagen fibers; eventually fracture will occur when the sliding of fibers is so extensive that they separate. They subsequently curl back (after failure) because of residual stresses in the structure. This mechanism of straightening, stretching, rotation and separation of the collagen fibrils represents a very potent form of toughening which confers the remarkable tear resistance that is characteristic of skin. This has similarities with the mechanism of deformation of the Bouligand structure.

It is worth noting that although non-mineralized collagenous materials, such as skin, resist fracture because they display ductility (strain to failure) from extensive inelastic deformation mechanisms, toughness can also be generated in tissues with limited ductility,

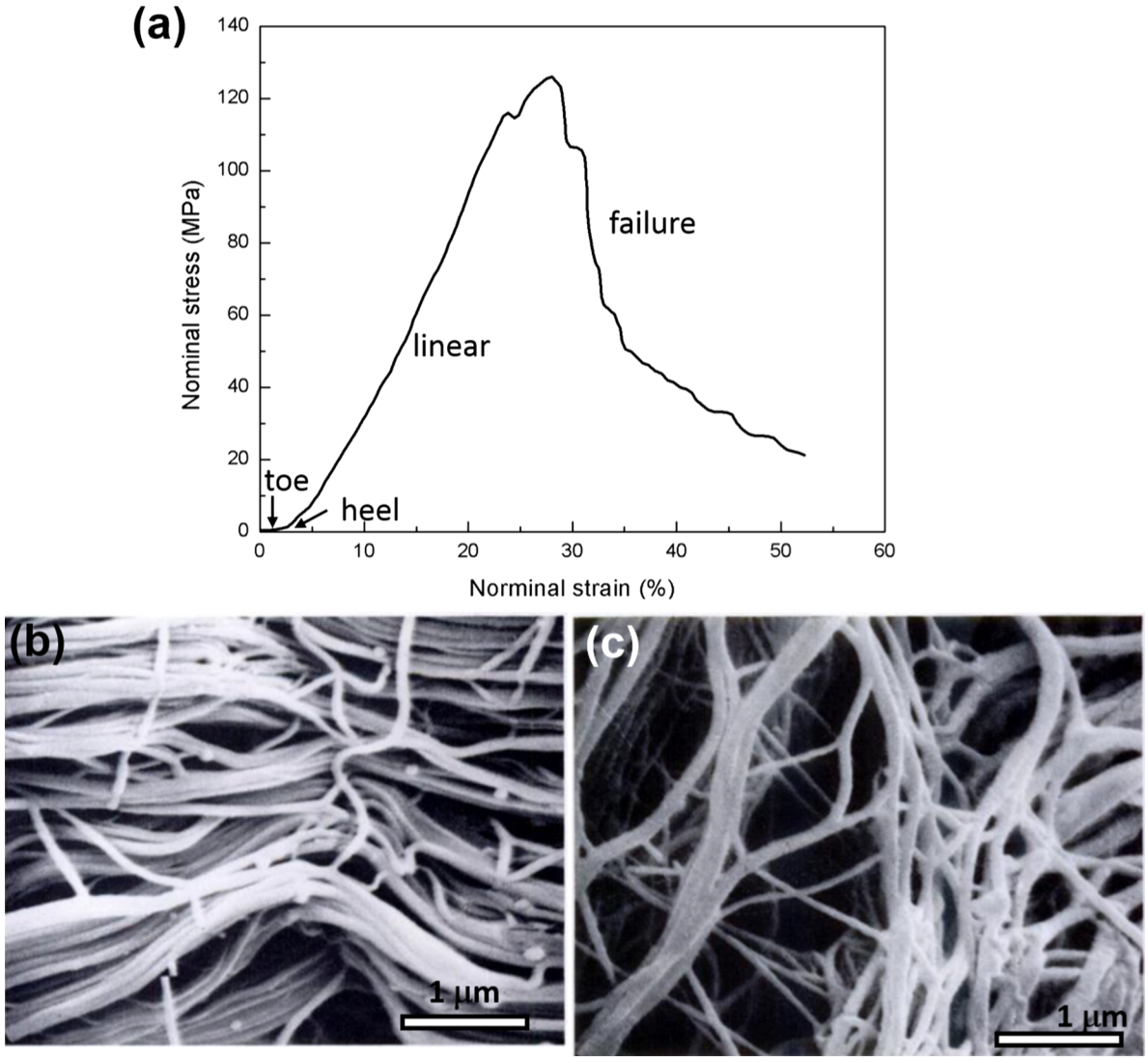

Fig. 4.5. Tension behavior of the ligament. (a) uniaxial tensile stress-strain curve of a ligament (re-calculated from Ref. [104]; (b and c) anterior cruciate ligament before and after tension test.

as in the case of mineralized collagenous tissue such as bone. Indeed, Nature is particularly adept at this. In Fig. 4.12b, the processes of toughening are separated in terms of intrinsic (plasticity) *vs.* extrinsic (shielding) mechanisms. The intrinsic mechanisms are invariably associated with nanoscale phenomena which occur ahead of the crack tip; they principally involve plasticity mechanisms that can inhibit damage and/or absorb energy by enlarging the plastic zone. Extrinsic mechanisms are quite different; they are generally micrometer-scale mechanisms that operate at or behind the crack tip, (as noted above) to reduce (shield) the local stresses and strains actually experienced at the crack tip via such processes as crack deflection and bridging. Indeed, toughening in many natural materials such as bone, involves the generation of both intrinsic and extrinsic mechanisms, which is a prime reason for their structural integrity.

5. Protective function of the structural combination developed in nature

As discussed above, biological collagenous materials are toughened by a variety of mechanisms; furthermore, in nature the actual hierarchical architecture of the material provides additional supportive and protective functions. An important characteristic of natural materials is that these configurations usually contain gradients in structure, composition or properties [109], such as a hard outer protective surface and an inner flexible energy-absorptive component for impact or penetration resistance; examples are natural dermal armors such as fish scales and alligator osteoderms. Several examples of the design and configurations of the collagenous materials are discussed below.

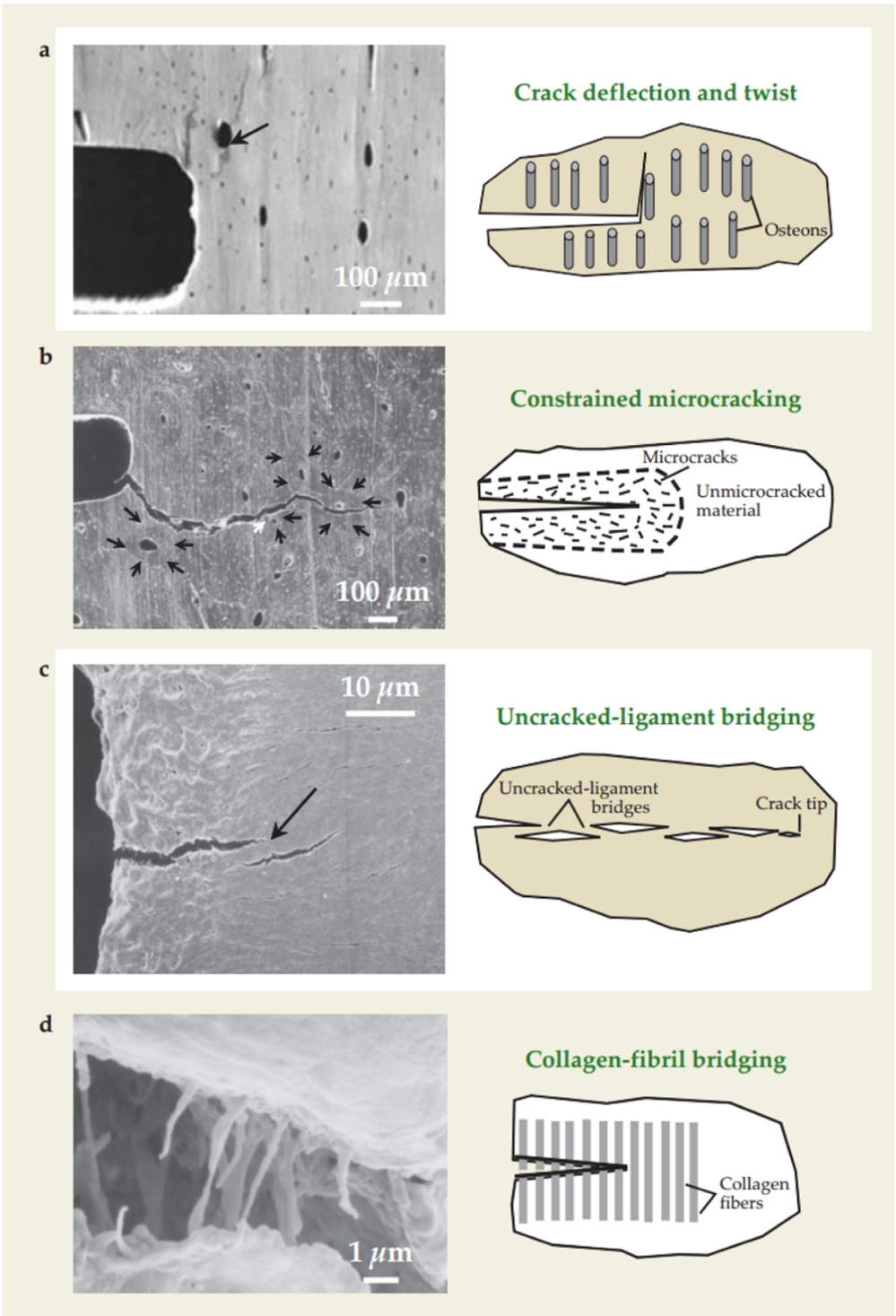

Fig. 4.6. Toughening mechanisms in human bone; showing (a) crack deflection/twist, (b) constrained microcracking, (c) uncracked-ligament bridging, and (d) collagen-fibril bridging (adapted from Refs. [11,98]. All these mechanisms are extrinsic toughening mechanisms that operate at fairly coarse length-scales (typical $>$ 1 μm) to "shield" the tip of any incipient crack from the applied stresses; the most potent mechanisms in bone are crack deflection and bridging.

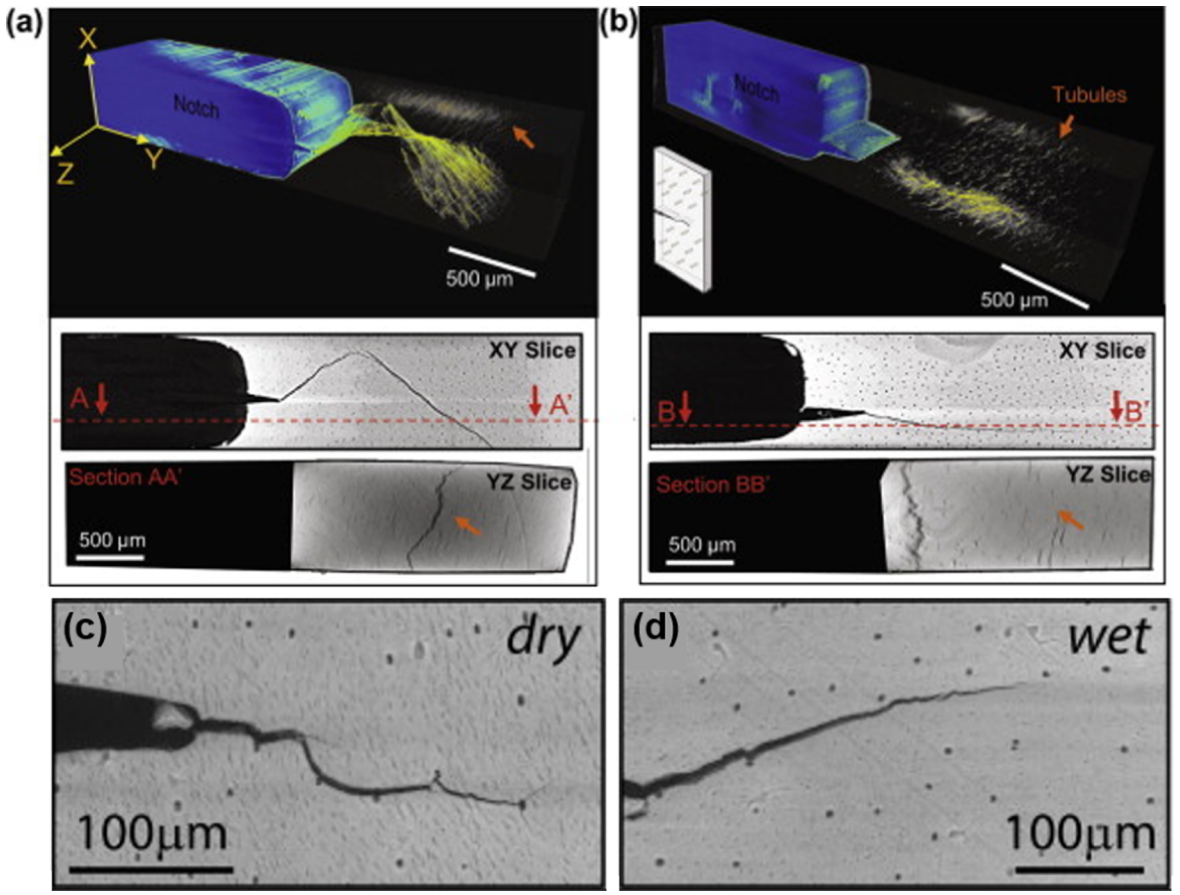

Fig. 4.7. Crack paths in fish scales visualized in 3-D with synchrotron X-ray computed micro-tomography; in (a) dry and (b) wet alligator gar fish scales. (a) Top: tomographs showing the path of the crack taking a twisting route through the dry sample's thickness (left); (b) crack in the wet sample propagates relatively straight (top right). (Colors of green define the cracks and blue the pre-crack and notch.) Bottom images are 2-D slices of the crack path reinforcing the twisted and straight paths, respectively, for dry and wet conditions, with blue representing the pre-crack and notch. The bottom images are 2-D slices of the crack path again showing the twisted and straight paths, respectively, in dry and wet scales. SEM images of crack paths in dry (c) and wet (d) condition. Whereas the crack paths in the wet scale are relatively straight and seemingly uninfluenced by microstructural features such as tubules and collagen fibers, cracks in the dry scale always follow the tubules. This is attributed to plastic deformation around the tubules in the wet condition, decreasing their stress concentration. In dry samples, the stress concentration in the surrounding of tubules acts to attract the crack [14], similar to behavior in tooth dentin.

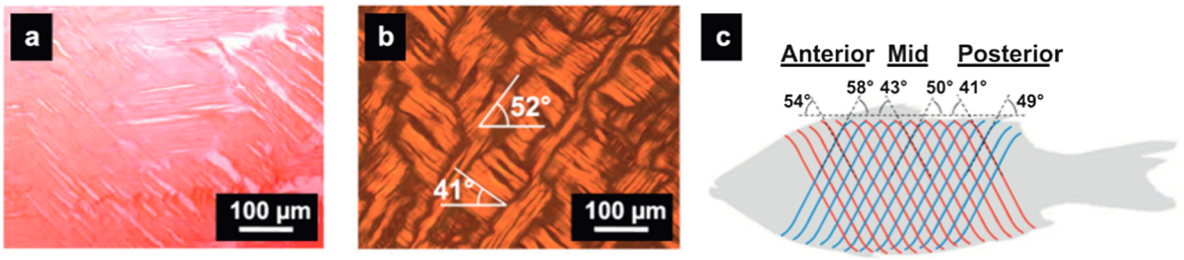

Fig. 4.8. Collagen arrangement in stained sagittal sections of striped bass skin in (a) standard and (b) digital image correlation modes; (c) schematic drawing of arrangement of the collagen fibrils in bass skin [105].

5.1. Design of bone with compact outside and spongy inside

Bone is composed of a compact (cortical) outer layer with a spongy (trabecular) layer inside. Reilly and Burstein [110] and Carter et al. [80] characterized the tensile and compressive behavior of cancellous bone and found that although it exhibits poor tensile behavior, it absorbs significantly more energy under compressive loads (Fig. 5.1a). Indeed, the estimated energy absorption of vertebrae is markedly greater than that of patella (Fig. 5.1b), not because of the differences in the sizes of the bone but because less

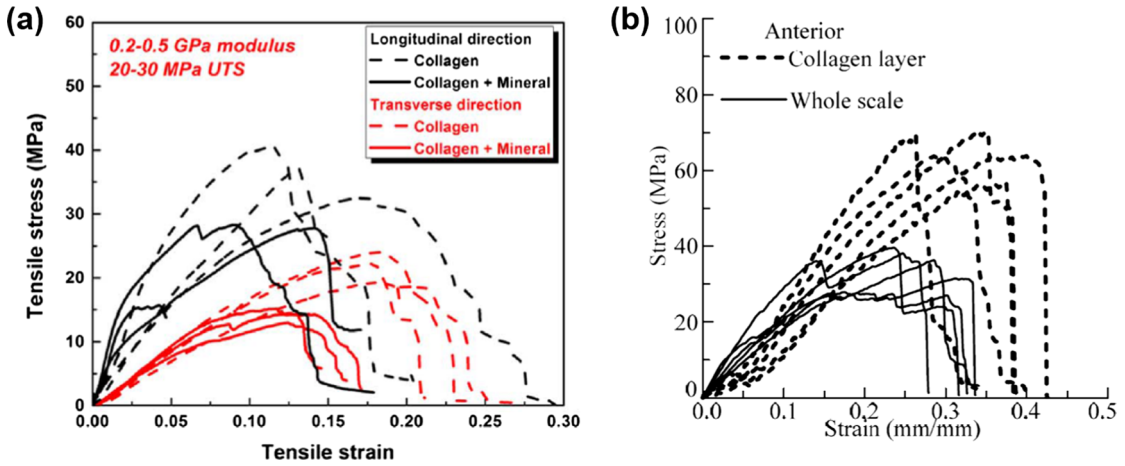

Fig. 4.9. Uniaxial tensile stress-strain curves for elasmoid fish scales; showing differences between collagen layers and the whole scale of (a) arapaima gigas [15,106] and (b) grass carp [107].

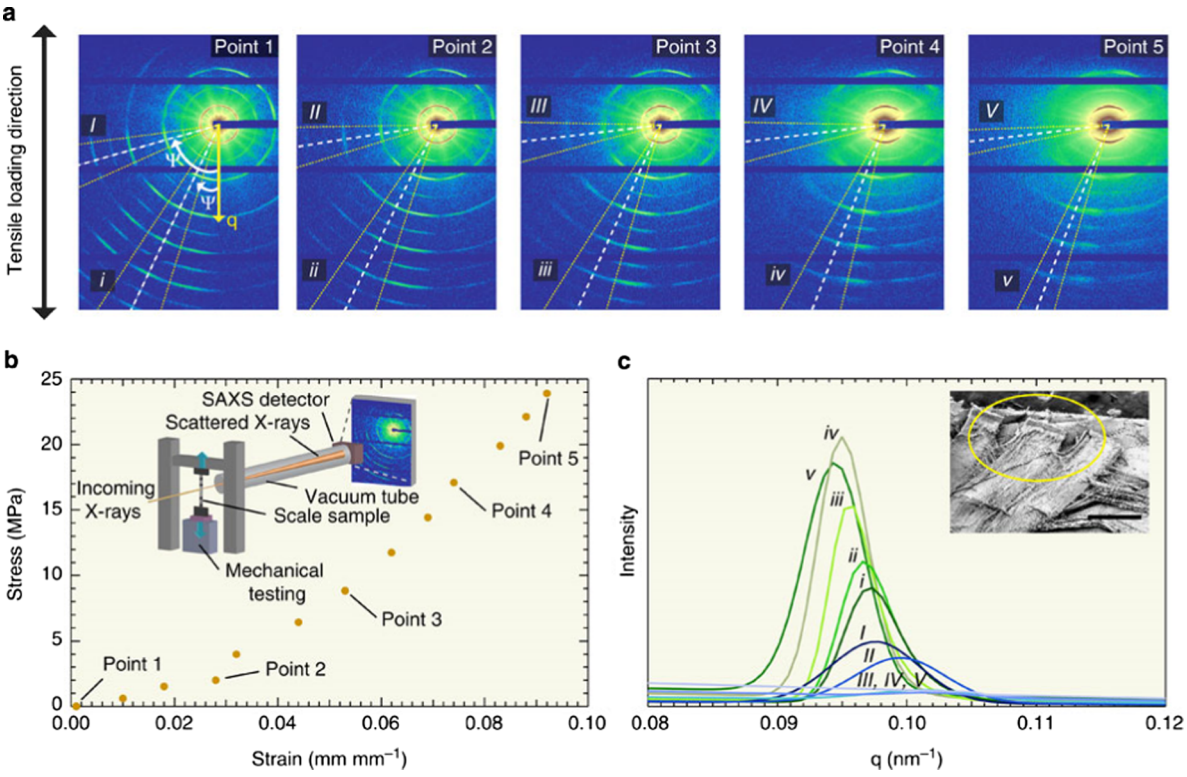

Fig. 4.10. Small-angle X-ray scattering of arapaima fish scale. (a) SAXS spectra at five strain levels during *in situ* mechanical testing of an arapaima fish scale (see inset of (b)). The stress-strain curve (*i.e.*, tissue stress *vs.* tissue strain) is shown in (b) with the five representative data points highlighting which diffraction patterns are shown. (c) The 2-D diffraction patterns (typically at the arcs (i–v) and (I–V)) were analyzed and translated to 1-D intensity *vs.* q which is in the reciprocal relationship of the d-spacing of the collagen. Clearly, collagen fibrils strained from i to v show a the negative shift in q, the increase in intensity indicates more fibrils have aligned to the loading direction; in contrast, the other set of data (I to V) show a compressive strain and the peak disappears at higher strain indicating interfibrillar separation (see inset, scale bar, 500 μm) [75].

energy is absorbed by cancellous bone in tension than in compression. Compact bone exhibits much more energy dissipation in compression than cancellous bone at a strain of 0.04; however, during the 0.04–0.5 range, cancellous bone continuously dissipates energy under compressive load which can reach as much as that of the compact bone at a strain of 0.5 (Fig. 5.1c). In light of this, it is of pertinent to study the mechanical behavior of the entire bone, and in particular to determine the origin of its toughness properties.

In this regard, the strength and toughness of small bones, specifically wild-type rat and mouse femurs, have been quantitatively assessed by Ritchie et al. [91] using notched samples loaded with the posterior surface in tension and the anterior surface in

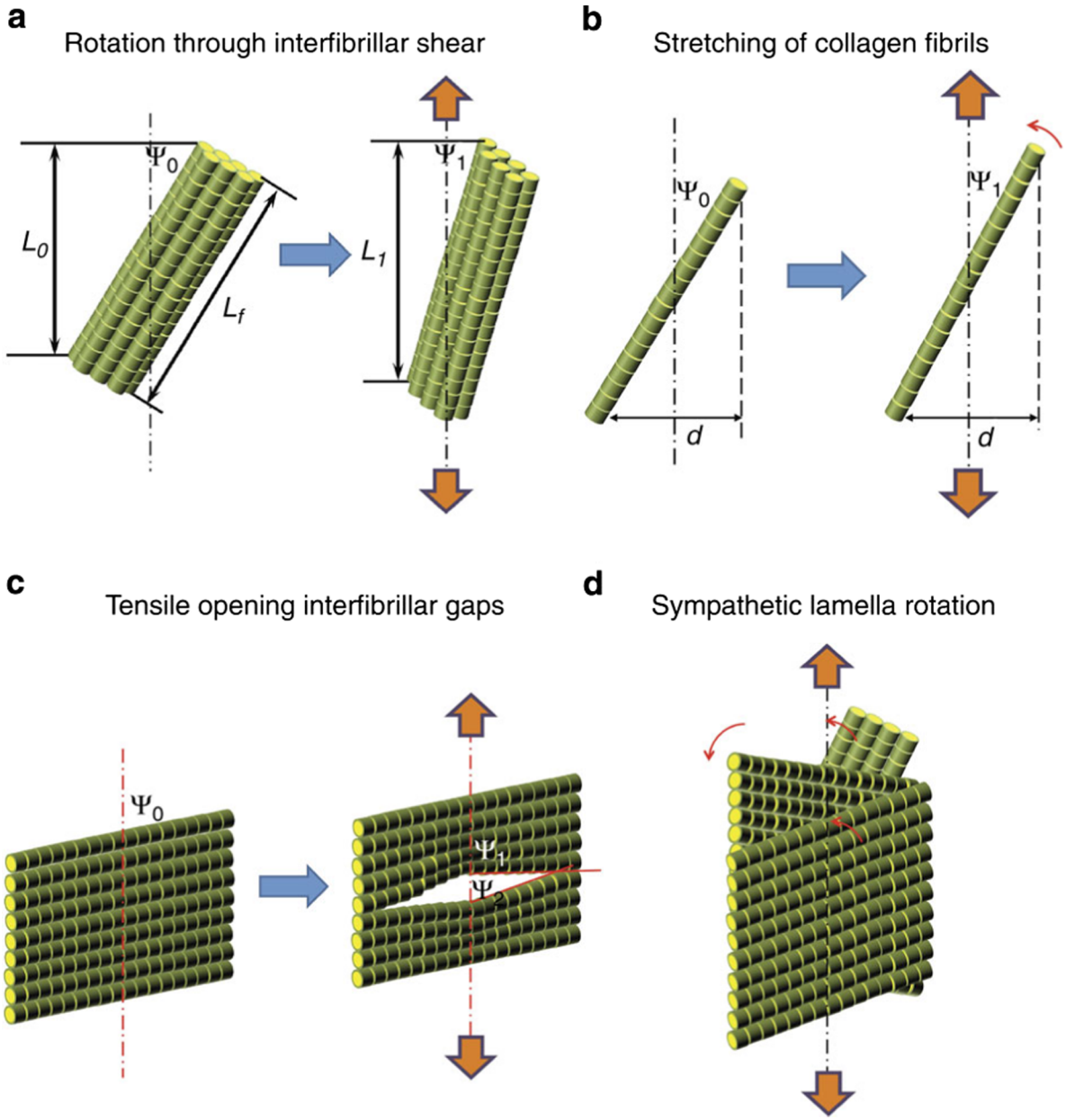

Fig. 4.11. The deformation and rotation phenomena of fibers in the arapaima fish scale's Bouligand-type structure; explained through four principal mechanisms. (a) Fibrillar rotation towards the tensile axis along with the interfibrillar sliding, fibrils with the length of L_f at an original orientation from the tensile axis of ψ_0 reorient to ψ_1 with a corresponding increase in projected length from L_0 before loading to L_1 under loading; (b) fibrillar rotation (from ψ_0 to ψ_1) can be caused by elastic stretching of the lamellae projected length d is assumed to remain unchanged. Other mechanisms within the Bouligand-type structure could be responsible for rotation away from the tensile axis. (c) Tensile separation of fibrils at an initial orientation of ψ_0 could force some fibrils to reorient toward the tensile axis (ψ_2), whereas others rotate away from them (ψ_1). Additionally, (d) sandwiched layer rotate away with the neighboring layers rotate toward the tension direction [75].

compression (Fig. 5.2a) under three-point bending. Cracks initiated by the notch first grew stably and then unstably, as shown by the *in situ* SEM images in Fig. 5.2c; the notch, stable crack growth and unstable cracking regions are labeled as well as the positions marked in the cross-section of the bone shown by the sketch at the top left. The following methods were used to determine the toughness values for small bones: (a) a "crack-initiation method" by determining the initial angle (θ_{init}) with the load (P_Q) with a 5% secant line in the load/displacement plot, (b) a "maximum-load method" by simply considering the maximum load as the instability, and (c) an "crack-instability method" analyzed by taking the load at fracture instability and the angle (θ_{inst}) when the crack was observed to be unstable from *in situ* SEM image (shown in Fig. 5.2). The latter two methods were recommended to evaluate the K_c toughness values of such small bone samples such as mouse femurs. By combining the compact with spongy (trabecular) bone, the

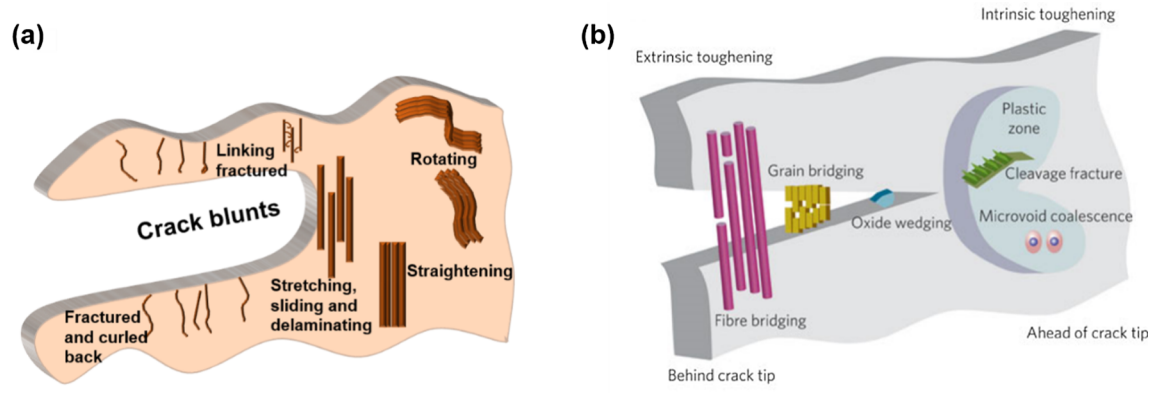

Fig. 4.12. Schematic illustrations of toughening mechanisms. Images illustrate the fracture mechanisms in (a) skin, in relation to those operating in (b) synthetic materials based on intrinsic toughening mechanisms that operate ahead of a crack tip to inhibit microstructural damage (these are motivated primarily by plasticity/inelastic mechanisms), and extrinsic toughening mechanisms that operate at, or behind, a crack tip to "shield" it from the applied driving forces [108].

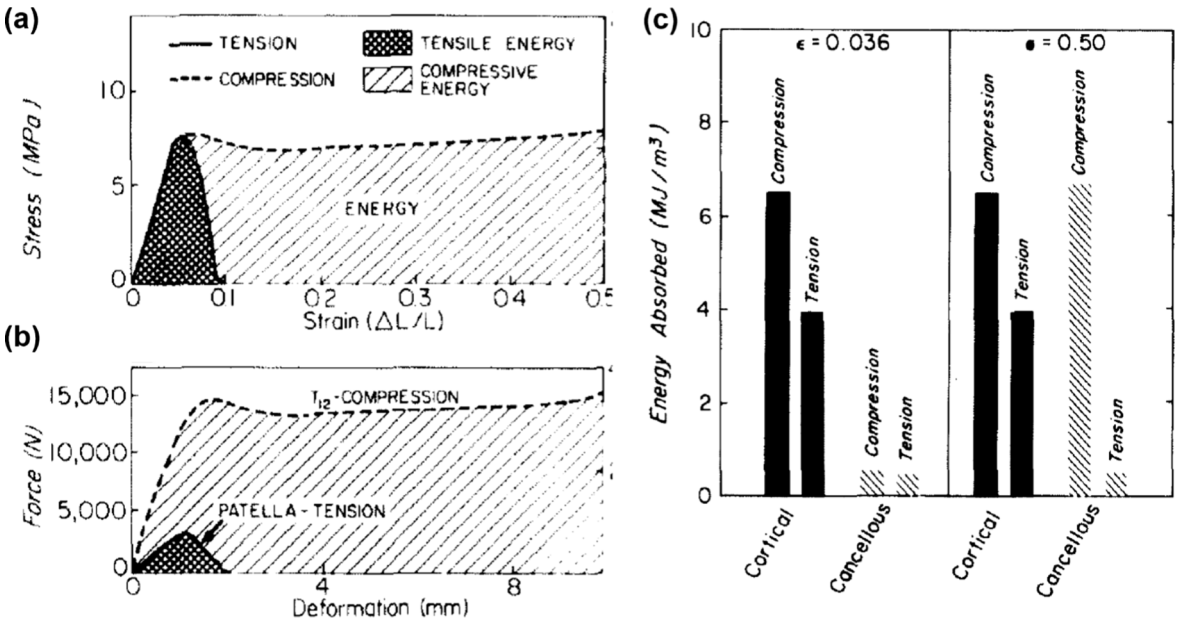

Fig. 5.1. Tensile and compressive constitutive behavior of bone. (a) The tensile and compressive stress-strain curves of cancellous bone with an apparent density of 0.4 g/cm^3, (b) The force-deformation curves for a compressive fracture of the twelfth thoracic vertebra and a tensile fracture of the patella, (c) the energy absorption capacity of cortical and cancellous bone at low strain (0.036) and high strain (0.50). Energy absorption for cortical bone was derived by Carter et al., [80], from the study of Reilly and Burstein [110].

bending stiffness, strength, and toughness of the rat and mouse femurs were evaluated to be 3.4 GPa, 158 MPa and 2.2–2.9 MPa.m$^{1/2}$, respectively, *i.e.*, superior to compact bone in the transverse direction (shown in Table 3.1) [91].

5.2. Fish scales with hard outer layers and tough inner layers

Being the natural dermal armor of the fish, fish scales invariably have a hard mineral-rich external layer on top of collagen-richer inner layers. The simple concept is that the hard outer layer resists penetration whereas the tougher underlayers act to absorb the extraneous deformation. The ganoid fish scales of the *Polypterus senegalus* are a good example; they have a harder hydroxyapatite (HAP)-based nanocomposite outer layer which comprises anisotropic rod-like HAP oriented approximately perpendicular to the surface plane (Fig. 5.3a) and a tough bony inner layer (Fig. 5.4). To understand the protective mechanisms generated by the ganoine outer layers, microscale pillars, prepared by using the focused ion beam (FIB) milling at different orientations to the HAP rods (shown in Fig. 5.3a), were tested using a micro-indenter [111]. It was found that cracks tended to propagate along the weak organic layers (Fig. 5.3b), because of the orientation-dependent properties of the ganoine layer [112]. Loading perpendicular to the surfaces and

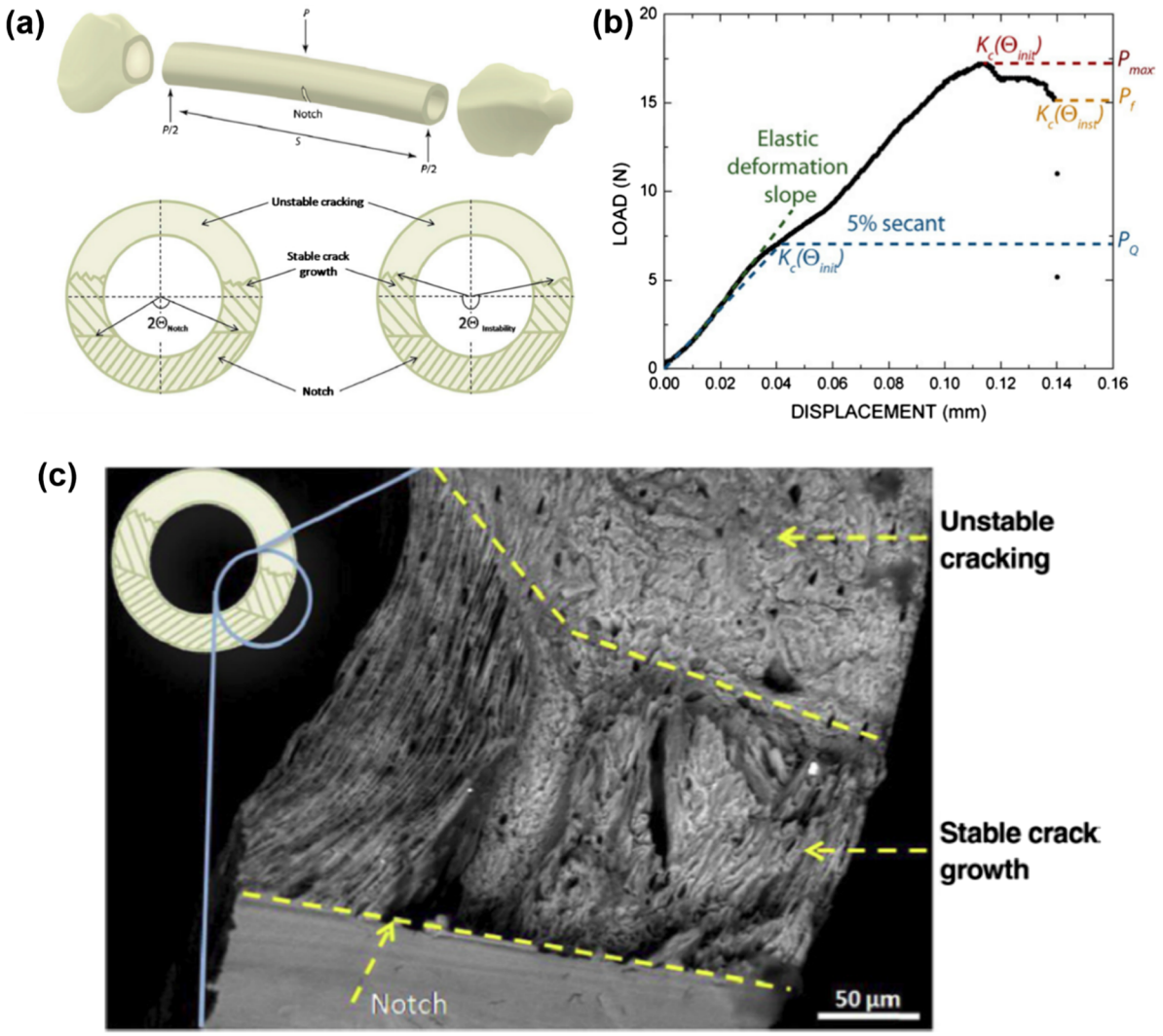

Fig. 5.2. Fracture toughness testing of small bone. (a) Schematic drawing showing how to prepare the small (mouse or rat) bone and test them to evaluate the fracture toughness. From the cross-section, one can see the notch region and the estimated predicted stable crack growth and unstable cracking regions. (b) Representative load-displacement curve for a sharply-notched bend specimen. Fracture toughness K_c is determined by the loads P_Q (intersection of the loading curve with a line that has a 5% lower slope than the elastic deformation slope), P_{max} (maximum load), and P_f (load at unstable fracture) (c) SEM image reflecting the schematic drawing in (a) and showing the machined notch, region of stable crack growth, and the region of unstable fracture, used to measure the crack size (half-crack angle) for the instability method of determining the fracture toughness. [91].

parallel to the rod-like HAP (at 0° in Fig. 5.3) yields the highest strength and stiffness, confirming the protective mechanisms of the ganoid scales; in the other two orientations (45° and 90° in Fig. 5.3), the ganoine shows strain hardening. Due to the irregular shape of the HAP crystals, interlocking between the crystal rods as well as inter-crystal friction can play an important role in the toughening mechanisms for the ganoine layer.

The interface between such hard outer layers and the tougher inner layers is often graded to avoid any singularity at a sharp interface between dissimilar materials. The inner layers (isopedine and bone) have considerably lower hardness, with a clear gradient character in the structure. Another strategy, employed in the scale of the alligator gar, is to have a rough zig-zag patterned interface between the outer layer and the inner layer, which can impede cracks from propagating through the interface from the ganoine into the inner boney layer (Fig. 5.4a). Nanoindentation results reveal a relatively sharp drop in the hardness from the ganoine (~3.5 GPa) to the bony layer (~1 GPa) which confirms the protective and toughening functions of the two layers [Chen et al. [74]]. From the mapping of the reduced modulus, one can see a sharp modulus change (green data in the mapping images, ~ 50 GPa) at the interface between two layers which indicates the very steep graded nature of the interface.

By comparison, the arapaima fish scale presents a considerably lower modulus and hardness and more mildly graded variation from the outer to the inner layer, as shown in Fig. 5.4d. The nano-hardness of the arapaima's outer layer is ~1.5 GPa and is similar to that of the inner collagenous layer of alligator gar scale, whereas in the inner layer of arapaima scale, which has a Bouligand

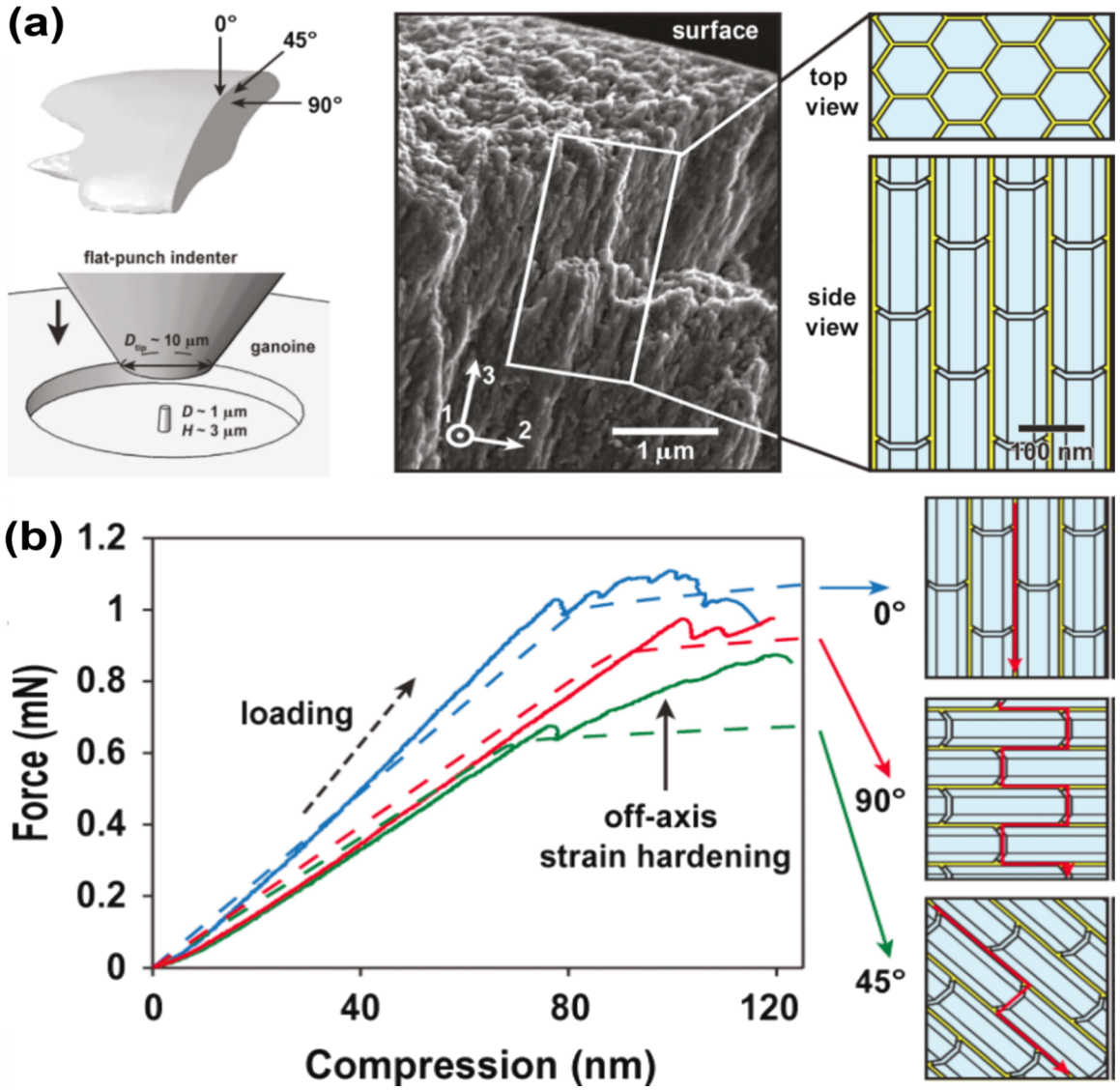

Fig. 5.3. Structure and properties of ganoine scales. (a) The morphology of ganoine scale with a structure containing mineral rods, ~100 nm in diameter, as a function of the loading direction and the indenter dimensions. (b) Typical force-displacement curves of the mineral rods in different orientations to the loading direction in the scale [111].

structure, the nano-hardness is ~0.5 GPa. Besides the obvious reduction in hardness from the outer to inner layers due to the decrease of the mineral content, the variation of the properties (hardness and reduced modulus in Fig. 5.4e and f) in the inner Bouligand structural layer additionally indicates a change in the orientations of collagen fibers from different (collagen) lamellae. [74].

To understand how the hard outer layer combines with the tough inner layer to protect fish such as the bass, Zhu et al. [96] investigated the deformation of a fish scale during a puncture test. The fish scale was put on a substrate, that mimics fish flesh, and was penetrated by a sharp steel stylet which simulated a predator's tooth. The force-displacement curve (Fig. 5.5a), as well as the deformation on both outer and inner surfaces (Fig. 5.5c), were recorded to simulate the process of the protection generated by the fish scales. Schematic drawings indicating the sequence of penetration events are shown in Fig. 5.5b. From the force-displacement curve, it is apparent that there are three stages marked by load drops indicating the deformation processes. The first stage is the elastic linear region due to the flexibility of the fish scale. During this stage, the outer layer is slightly damaged but the inner layer remains intact. However, after the initial penetration of the outer layer, the punching process enters the second stage at which the lower collagen layer starts to become damaged. As the tip of the puncture reaches the inner surface, the force-displacement shows a clear drop, and the penetration process reaches the third stage in which the puncture penetrates through the whole fish scale. Every drop in the force curve indicates a toughening mechanism, such as delamination of the fish scale. The function of the softer layer is to absorb the excess energy from the penetration and to restrict the harder surface layer, which exhibits some cracking, from complete fracture. This can

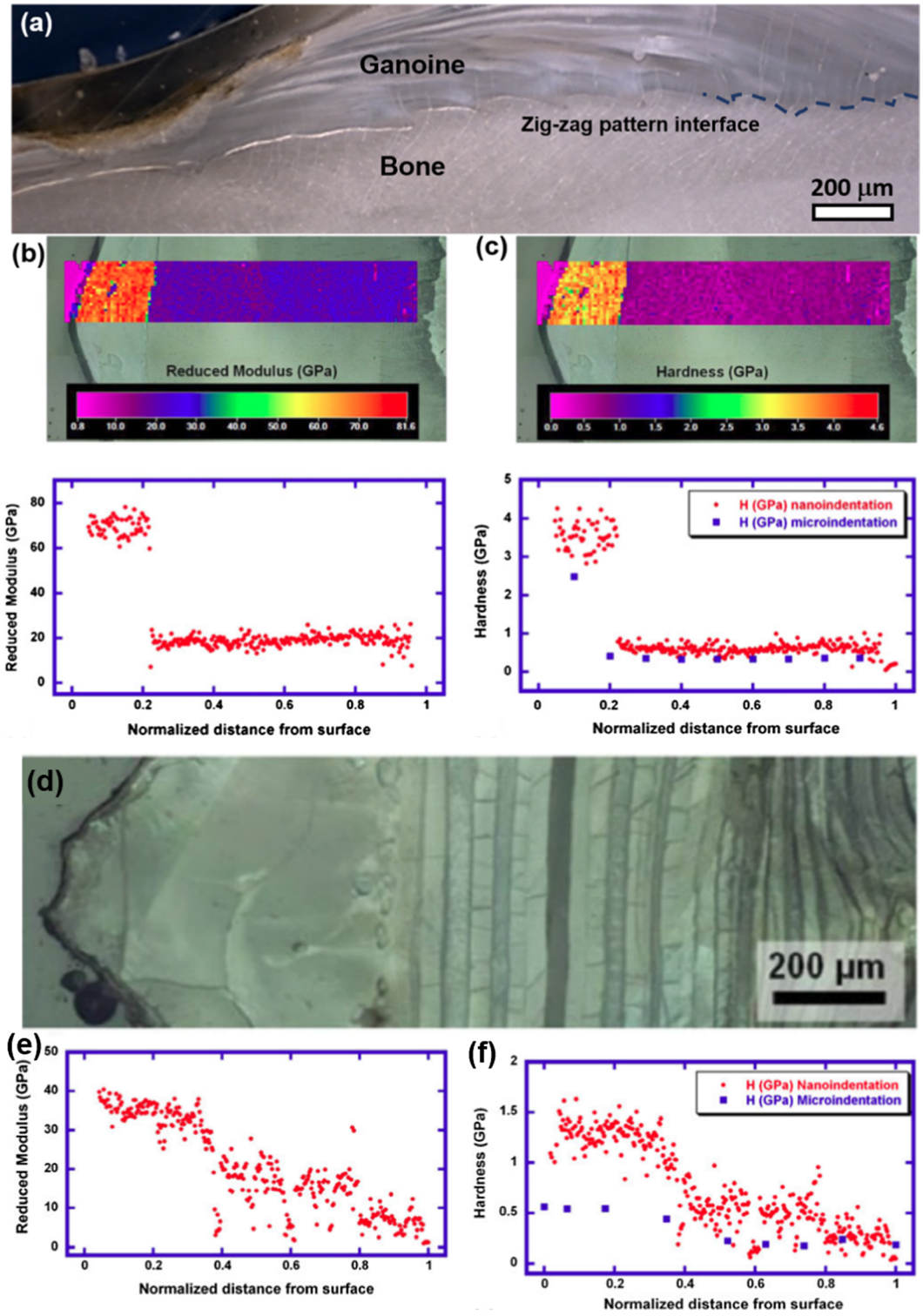

Fig. 5.4. Hard and soft layers in (a–c) alligator gar fish scales and (d–f) gradient in hardness and stiffness in the arapaima fish scales [74]. (a) Optical morphology of partial alligator gar fish scale with outer ganoine and inner bony layers showing a zig-zag pattern along the interface. (b) Reduced modulus measured on the cross-section of gar scale from the outer to inner layers (c) Nano-hardness, as well as micro-hardness, of the gar scale from outer to inner layers. (d) A cross-sectional optical micrograph indicating the region where nanoindentation was performed on the scale; (e) gradients in the reduced modulus, and (f) hardness through the thickness of the scale.

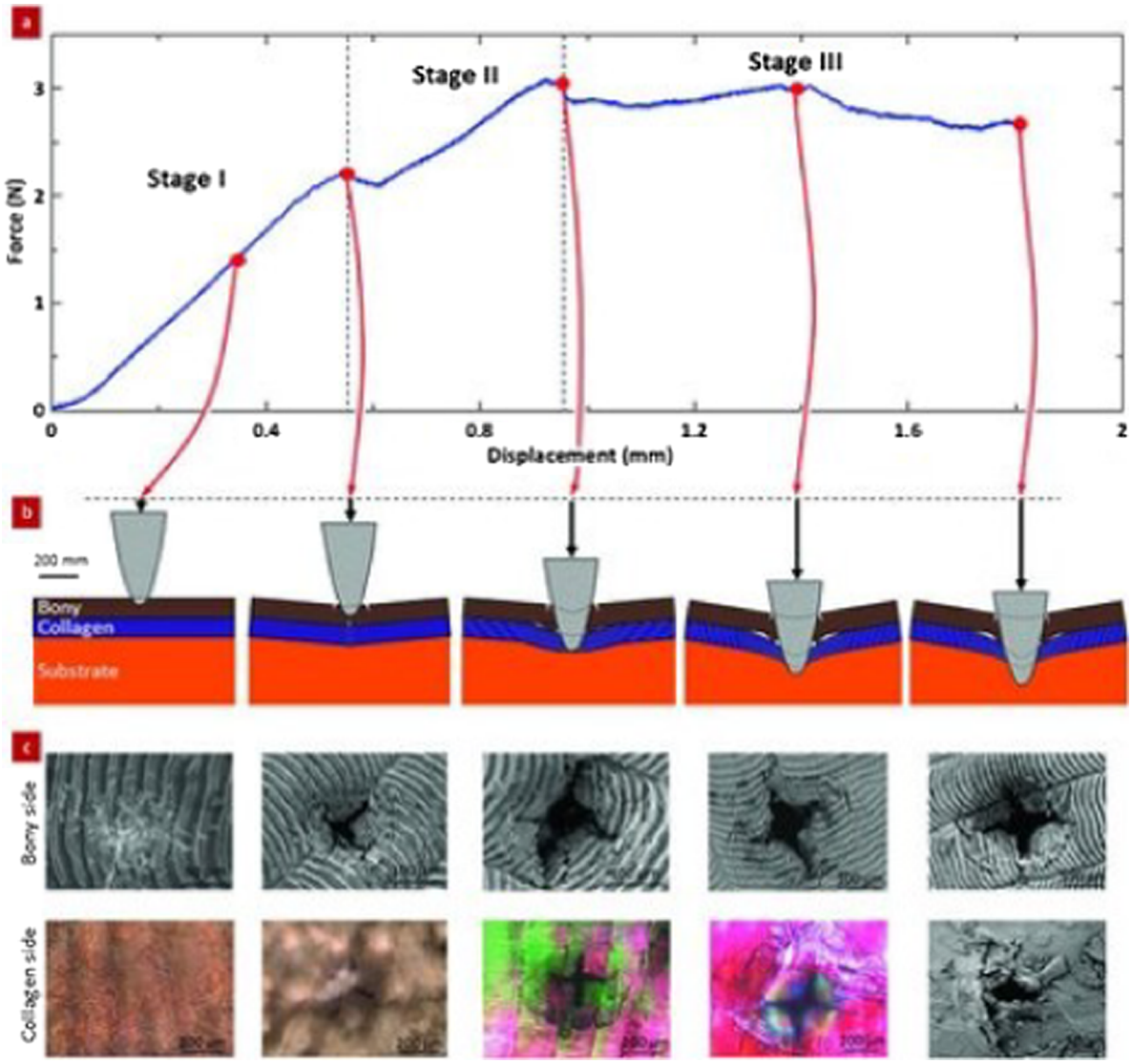

Fig. 5.5. Force-displacement curve and the deformation of a bass fish scale during a penetration test; (a) Load-displacement curve of the striped bass scale from the penetration of a sharp needle simulating a tooth (with a root radius of 25 μm). Three stages are shown during the deformation: I, elastic deflection of the scale, II, fracture of mineralized layer, and III, penetration of the collagen lamellae, (b) schematic drawing showing how the structure is damaged by the indentation load during the test, (c) characterization of the deformations (top-view) in the scale during the puncture test (from Zhu et al., [96]).

be seen in the sequence of photographs in Fig. 5.5 where the cracks (four, at 90°) do not propagate into the lower scale.

5.3. *Overlapping mechanism of fish scales*

Penetration testing on individual bass fish scales with different substrates has also been examined (Fig. 5.6a) [113]. For a single scale, (~4 N) it was found that the substrate stiffness had no significant effect on the penetration force (Fig. 5.6b). The penetration test was also conducted on the overlapped fish scales of half of the body of the bass, as well as on the descaled fish, as shown for comparison in Fig. 5.6c. Compared to the individual fish scale only, the overlapped fish scales on the fish body act to enhance the puncture resistance of the skin to the individual fish scale by a factor of four without any decrease in the penetration displacement. The scales clearly stiffen the skin, with the effect of decreasing the amount of deflection upon puncture [113]. Thus, the dermal armor of fish effectively provides protective toughening through the synergistic mechanisms of a hard mineralized outer layer, a tougher, more deformable collagenous inner layer, and the presence of overlapping scales.

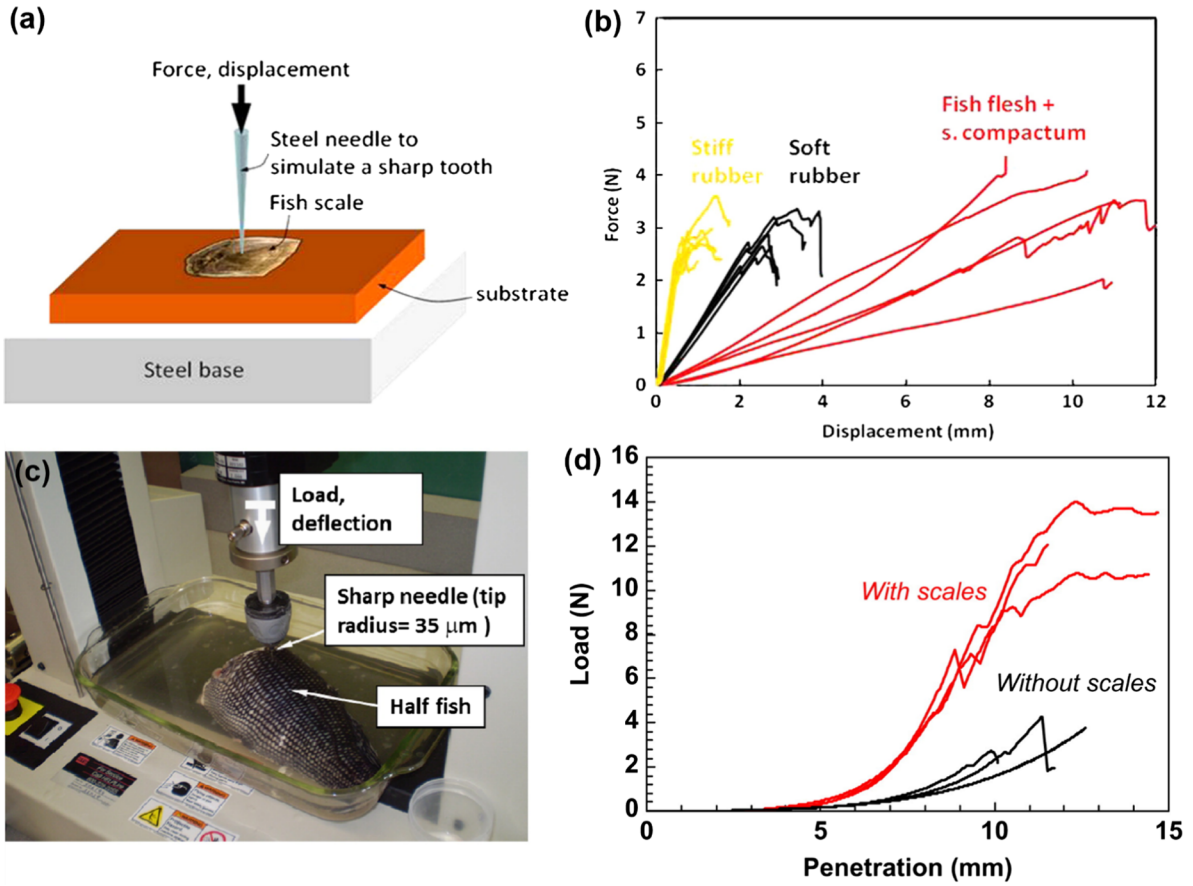

Fig. 5.6. Comparison of the penetration on a single scale and overlapped scales of the bass fish; showing (a) puncture tests setup on individual scales, (b) force–deflection curves for puncture tests using three different substrates, (c) puncture tests setup on a half-striped bass; (d) force–displacement curves showing that the scales increase the puncture resistance of the skin by four to five times [113].

6. Bioinspiration and biomedical (or tissue engineering) applications

Collagen is the most important protein in organisms and principally in vertebrates. It is approximately 25% of the dry weight of animals. The use of collagen-based glue dates to early history, and it has the advantage of being thermoplastic, *i.e.*, to soften as it is heated, releasing the glued parts. Thus, this may be considered as the first utilization of this important protein. The first group to identify its structure was that of Wychoff et al. [114]. Since that time, the arrangements and structural hierarchy of collagen have inspired contemporary researchers seeking novel solutions to materials problems. At the same time, there are a number of important biomedical applications of collagens. We will briefly review both aspects in the sections that follow.

6.1. Bioinspired and biomedical application at nano-, micro- and macro-levels

Collagen is biocompatible and biodegradable and is therefore well suited as a scaffold that will gradually dissolve away when implanted in the body as the host cells and structure are reconstructed. It can also be seeded with cells from the host, such as chondroblasts, osteoblasts and fibroblasts. One of the most important and successful applications of collagen was the development in the 1980s of artificial skin by Yannas and coworkers [115–120] and Burke et al. [121]. Indeed, the insertion of tissue-engineered skin into humans is nowadays a well-developed procedure. Commercially available names are Integra, Alloderm and Oasis. These engineered skin tissues incorporate a growing number of functionalities, through melanocytes, capillary networks, sensory innervation [122,123]. The terms autograft, allograft and xenograft are used to designate skin that is originally from the host, another human, or a non-human, respectively (*xeno* means “foreigner” in Greek). Collagen is also used in tooth repair, wound repair, artificial blood vessels, bone substitute, dermal filler and stent coating.

There has also been a significant effort devoted to synthesizing collagen, although it has only been partially successful. However, the amino-acid sequence and triple chain of the molecules have been synthetically produced. The length of the natural molecules is ~300 nm, but the average length of synthetic collagen is generally much smaller (~40 nm) [124], although strands longer than 400 nm have been produced more recently. For example, in 2011, Hartgerink’s group [125] added ‘sticky’ ends to the collagen

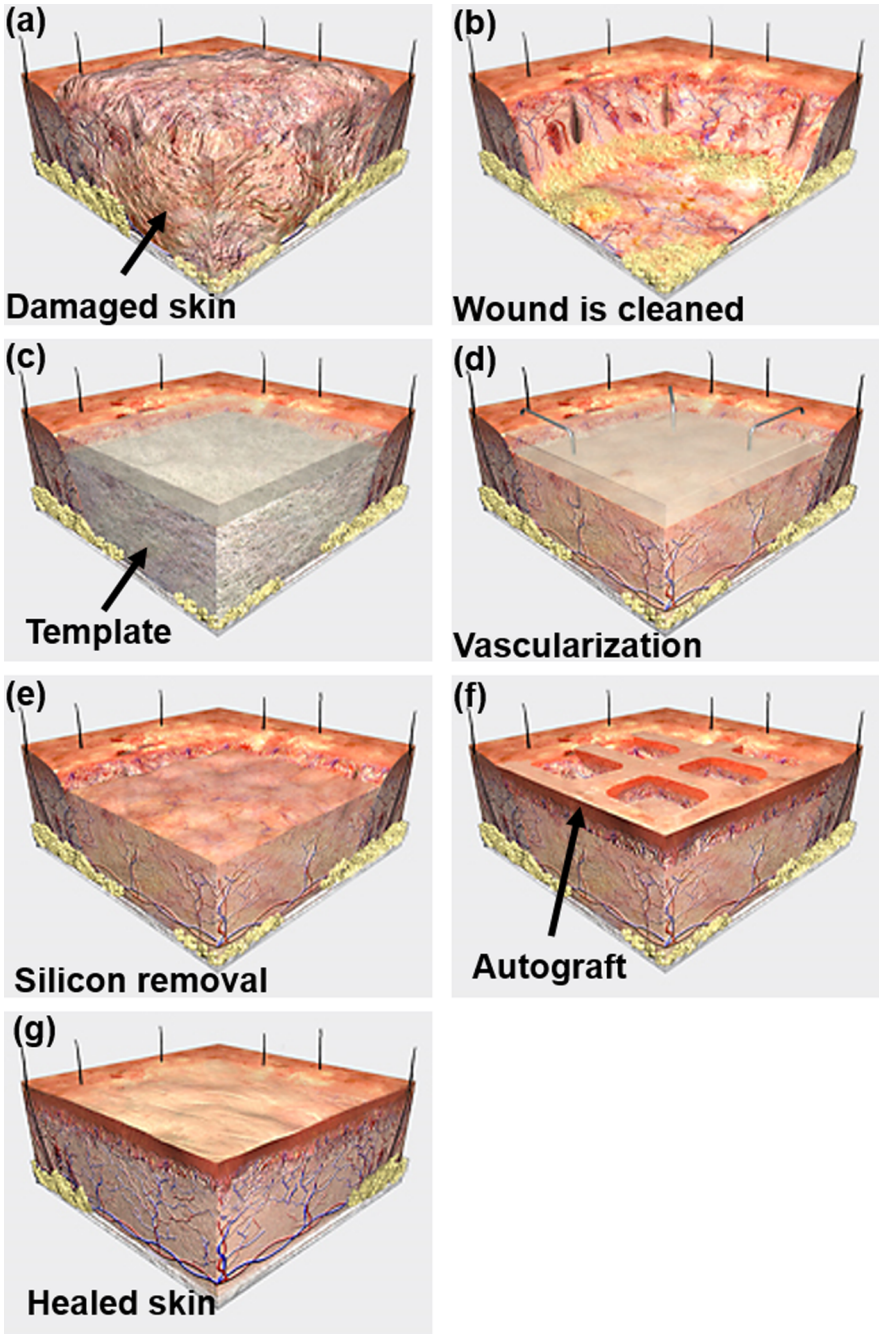

Fig. 6.1. Integra dermal regeneration procedure for repairing the skin from damage; (a) damaged skin; (b) damaged skin tissue excised (removed); (c) insertion of Integra biomaterial; (d) vascularization of implant over 7–14 days; (e) removal of top silicone layer, as the biomaterial is bio-resorbed and replaced by the organism; (f) insertion of array of connected strips of autograft, (h) growth of autograft covering surface (adapted from Integra website). (http://www.ilstraining.com/idrt/idrt/brs_it_04.html).

molecules so that they form long arrays, in a similar manner in which heads and tails in natural collagen molecules connect, with a 40 nm gap. This approach can create longer strands through self-assembly, as positively charged ends link to negatively charged ones.

Natural collagen, however, is still the choice for most biomedical applications. The majority of collagen originates from bovine, porcine and piscine sources. To eliminate the possibility of rejection though, it has to be denatured to remove all cells; if it has not been completely denatured, *i.e.*, the cells were not destroyed, unwanted immune responses by the host can be triggered. To date, there have been two basic methods reported to produce the substitutive collagenous biomaterials [126,127]:

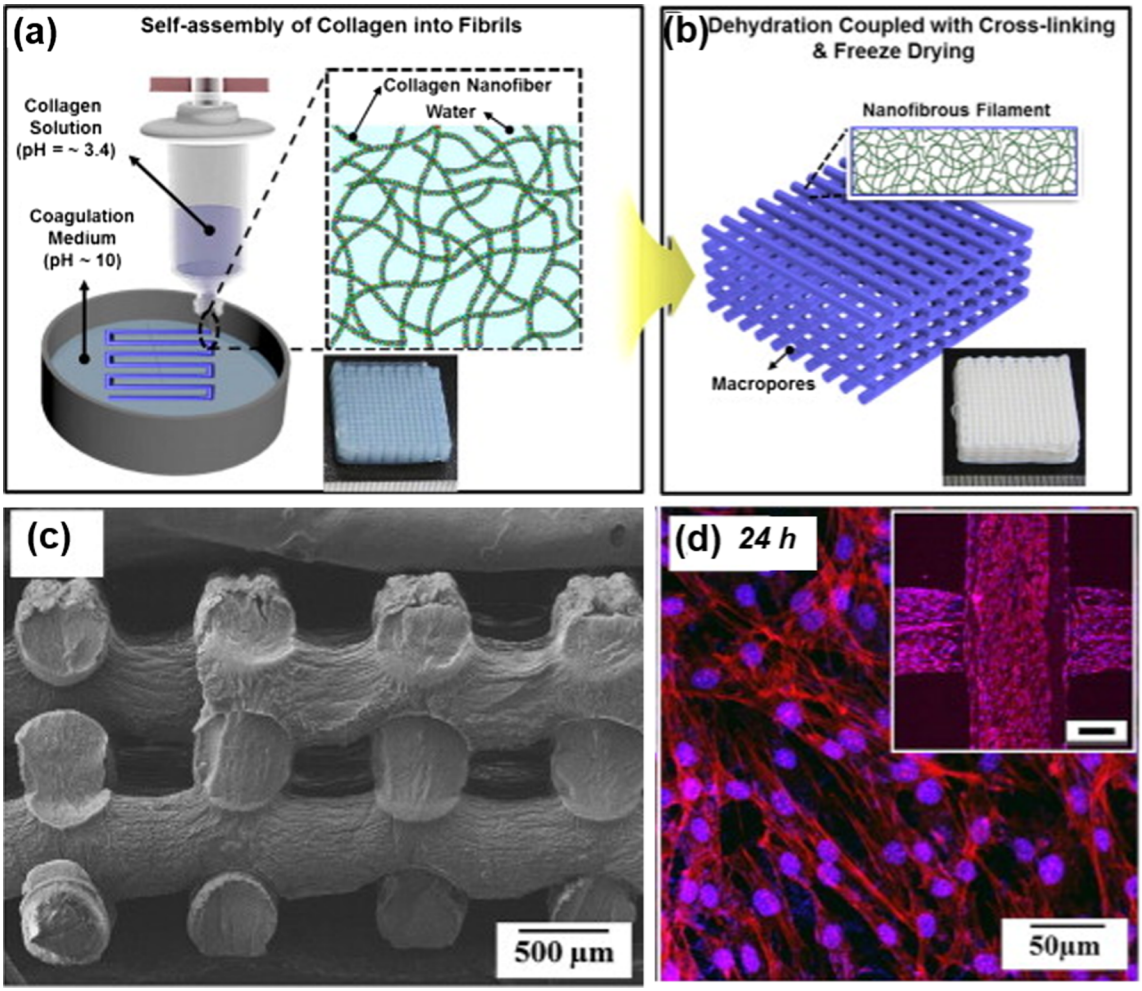

Fig. 6.2. (a and b) Schematic drawing shows the self-assembly-inspired 3-D plotting for the production of macro/nano-porous collagen scaffolds comprised of nanofibrous collagen filaments; (c) cross-linked 3-D deposition of collagen filaments, (d) cells attached on the macro/nano-porous collagen scaffolds after 24 hr of culturing (adapted from Shin et al., [134]).

1. Retaining the original size of the tissue while removing all the cells. This is accomplished by flash freezing (which forms ice crystals in the cells), by high pressure or through chemical means.
2. Creating a collagen solution with other molecules such as glycosaminoglycans (GAG), elastin or chitosan. This collagen can then be extracted by acid solution or by equivalent techniques.

The prime use of collagen has been with skin regeneration which is an important field in medicine such that a number of procedures have been developed to achieve this. We describe below the Integra procedure, developed by Yannas and coworkers [118], which consists of creating two layers: a surface layer of silicone rubber covering main body consisting of a collagen-GAG scaffold. The sequence is shown in Fig. 6.1. The original wound/burn is shown in (a). The damaged skin is excised (removed), the wound is cleaned (b) and the graft is inserted (c). After a few (7–14) days, vascularization sets into the collagen-GAG scaffold (d). The silicone layer protects the tissues of the body from bacteria and eliminates fluid loss; it also acts as a barrier against infection but can eventually be removed (e). An autograft (from the same organism) is placed on the collagen-GAG layer (f), which is bio-resorbed and replaced by tissue form the host. The autograft then grows to cover the entire surface (g).

To date, collagen scaffolds have found considerable application in tissue engineering for biomedical applications. There are a number of sources from which it can be extracted. Collagen scaffolds have favorable properties, specifically, low immunogenicity, porous structures for cellular growth, biocompatibility and biodegradability. However, a considerable deterrent has been that collagen scaffolds have low mechanical strength [128].

The principal human sources of collagen are peripheral nerve tissue or the placenta. However, collagen from other species such as bovine, porcine or sheep are commonly used. Collagen from fish skin and bones has also been found to be an excellent source. Of course, the material has to be denatured in order to eliminate any possibility of rejection by the host. Some advanced materials engineering techniques have been applied with success, namely, electro-spinning [129], lyophilization (freeze casting) [130], and

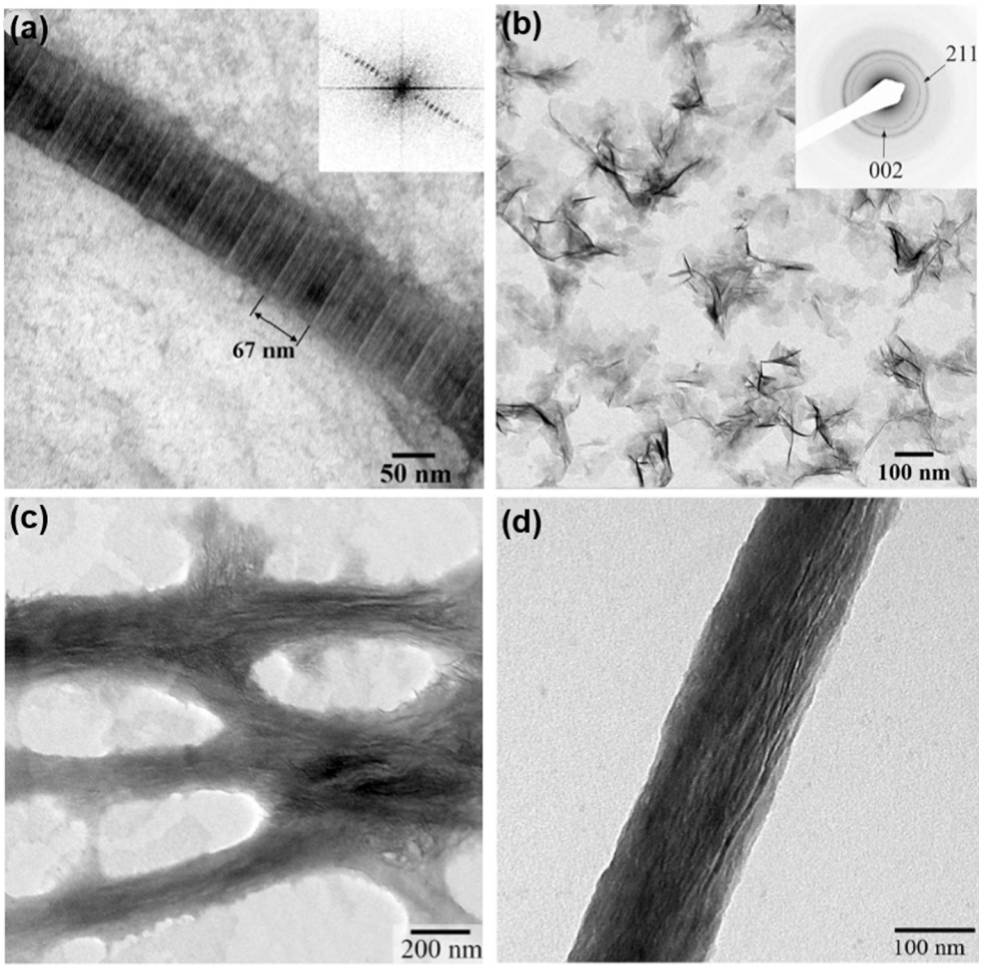

Fig. 6.3. Bioinspired minerialization of the collagen (a) a collagen fibril; (b) mineral particle obtained by mineralization process; (c) a region of mineralized collagen fibrils with both amorphous and crystalline mineral phases; (d) high magnification image of a mineralized collagen fibril. (adapted from Deshpande and Beniash, [135].

additive manufacturing [131–133]. Pure collagen recovered from the source is weak and therefore cross-linking has been applied to increase its strength. However, this creates problems of toxicity. In order to overcome these problems and to impart collagen scaffolds with mechanical strength, the use of natural biopolymers such as silk fibroin, chitosan, hyaluronic acid and alginate has been successfully implemented. Synthetic polymers have also been blended with collagen to produce more robust scaffolds; most notable are polycaprolactone (PCL), polylactic acid (PLA), poly ethyl glycol (PEG), polyglycolic acid (PGA), polylactic-co-glycolic acid (PLGA), and polyvinyl alcohol (PVA). Many of these are bioresorbable which is naturally a desirable characteristic.

One of the best examples of the medical use of synthetic collagen are macro/nano-porous collagen scaffolds, in particular comprised of nanofibrous collagen filaments (Fig. 6.2a and b) as these can more closely mimic the hierarchical structure of the native tissue. These can be made using a combination of 3-D plotting and a collagen self-assembly process. The macro/nano-structure of the gelled porous collagen scaffolds are structurally stabilized by a dehydration process coupled with chemical cross-linking, as shown in Fig. 6.2c, which allows the cells to attach, as shown in Fig. 6.2d [134].

At the nano-scale, collagen can also be synthesized into mineralized fibrils. Deshpande and Beniash [135] applied poly L-aspartic acid to reconstruct mineralized collagen fibrils; they further studied the deposition and growth of the crystals co-aligned with the collagen fibril axes by using transmission electron microscopy and electron diffraction. Initial mineral deposits formed in the fibrils lacked any long-range crystallographic order yet transformed into crystals with time; the shape and organization of these amorphous deposits were similar to the crystals found in the mature mineralized fibrils (Fig. 6.3). The collagen alone did not affect mineral formation and poly L-aspartic acid was found to inhibit mineralization in a concentration-dependent manner.

At the micro- to macro-scale, collagen has been blended with minerals, such as HAP, tricalcium phosphate (TCP, $Ca_3(PO_4)_2$), or silicate. These additions provide enhanced stiffness to the scaffold. For example, collagen produced by electrospinning with PLLA has been impregnated with HAP by Ngiam et al. [136] to generate scaffolds with improved capture characteristics for osteoblasts, which is important for bone grafts.

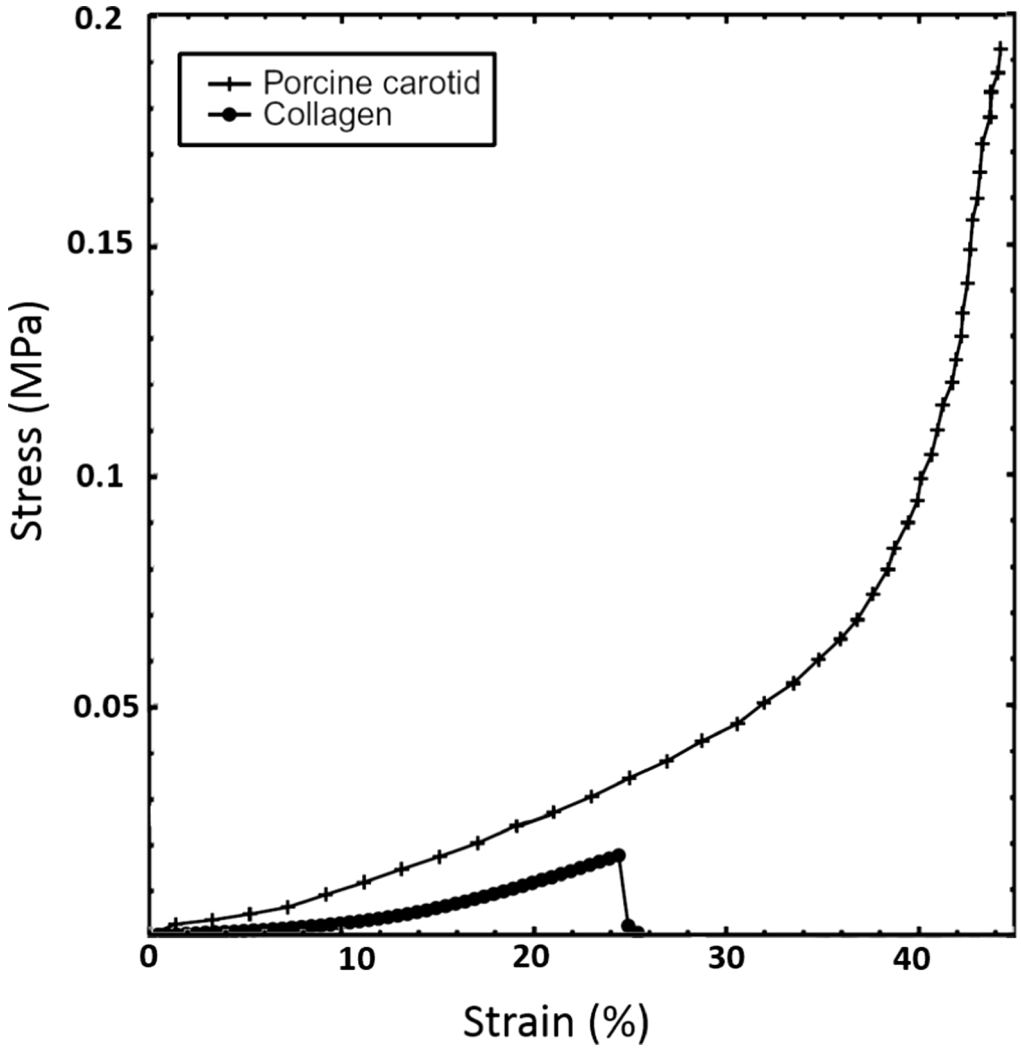

Fig. 6.4. Comparison between mechanical response of porcine carotid artery and collagen- hydrogel scaffold. Note the much lower strength of the scaffold (adapted from Meghezi et al. [137]).

Going farther into synthetic materials, the ubiquitous carbon nanotubes and graphene have been incorporated into collagen scaffolds with positive results. We note here that collagen hydrogel scaffolds have been fabricated and assembled as possible vascular grafts [137]. As with other collagen-based scaffolds, the goal is for the graft to be completely incorporated into the host tissue; however, the mechanical strength of the collagen hydrogel is much lower than the carotid artery into which it is intended to be grafted on (Fig. 6.4). This is not surprising since the great majority of the gel − 99.8 wt% – is water. The solution in the fabricated procedure has a collagen concentration of 2 g/L; the mixture is then poured into a mold and left to gel before a culture medium is introduced to cause the mixture to gel into a tubular mold, which is then inserted into a bioreactor. The stiffness of the construct increases with a resultant decrease in stress relaxation during the process.

For stiffer grafts, such as the ones used in bone and teeth, a hybrid construct of collagen has been assembled by using freeze casting such that TCP can be produced with additive manufacturing [130]. Fig. 6.5 shows how this composite is made by using a combination of 3-D printing and freeze-drying methods to design heterophasic constructs for osteoblastic differentiation of dental pulp stem cells (DPCs). Inspired by the anisotropic microstructure of native bone tissue, the resulting designed constructs consisted of a 3-D printed β-TCP scaffold with interconnected porosity resembling the bone mineral phase; this was designed to fulfill the mechanical function of bone, but additionally embedded with a collagenous matrix to mimic the bone extracellular matrix to support dental pulp stem cells adhesion, proliferation and osteogenic differentiation.

Collagen has also been extracted from fish scales and mixed with alginate to form porous scaffolds [138]. By investigating different molecular weights of collagen, these authors researchers obtained a structure that was optimized for mechanical, physicochemical, and biological properties for skin regeneration. Fig. 6.6a and b shows the porosity at two magnifications; Fig. 6.6c is a florescence image of the scaffold after one day of exposure to live NHDF-neo cells. After 7 days (Fig. 6.6d), there is a marked increase in cellular activity, demonstrating that this scaffold has excellent biocompatible properties.

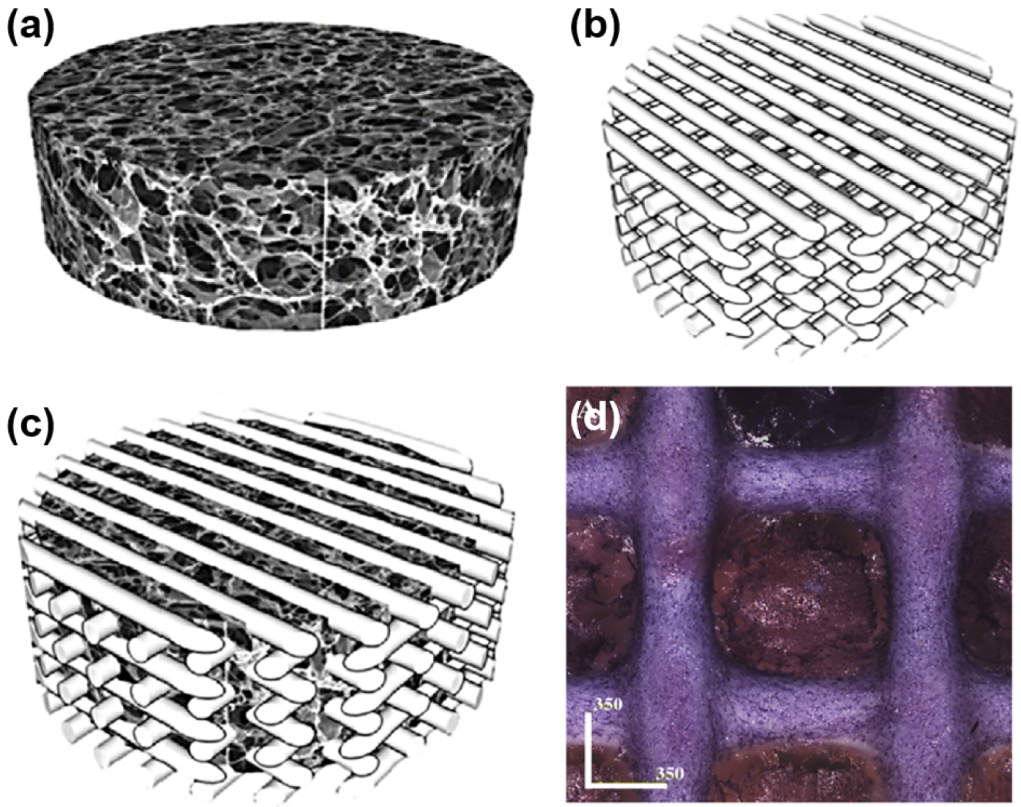

Fig. 6.5. Schematic representation of β-TCP/collagen hybrid composite constructed by combining (a) freeze-dried collagen matrix and (b) 3D-printed β-TCP scaffold. (c) The resulting structure; (d) dental pulp cells were cultured onto 3-D printed β-TCP/Col-TCP construct after three weeks (adapted from Fahinpour et al., [130]).

6.2. Bioinspired applications at constructive levels

There have been numerous attempts to mimic fish scales as a synthetic material, *e.g.*, for lightweight armor, to achieve materials which display both flexibility and penetration resistance. This is achieved in natural fish scales by several mechanisms. Due to their high mineral content (Table 3.1), the individual ganoid scales do not have much flexibility, and so the degree of imbrication is relatively high (0.78) to ensure the global flexibility through the connection mechanism. *P. senegalus* fish has ganoid scales, each of which contains a peg and socket for interlocking with others scales [13]. Due to the different shapes of the scales at the head and tail regions, the allowable motions between two adjacent scales can vary (Fig. 6.7a–h). The scales can be interlocked by the pegs and sockets to form a row (Fig. 6.7j) and overlapped from the sides; Fig. 6.7i shows such overlapping of the two rows of fish scales. As the fish needs to bend with extreme curvature during swimming, both of the interlocking and overlapping mechanisms contribute to such mobility. With the interlocking system, the scales are fully in contact and provide protective function. Although the interlock and overlap restrict the bending and rotating motion, the large anterior process enables relative sliding, resulting in more flexibility [139]. The pronounced shape features of the scales at the head region can provide more protection while the simpler shape of the tail scales enable more motion.

By mimicking the overlapping mechanism of the elasmoid scales on the striped red mullet (*Mullus surmuletus*) skin, Funk et al. [140] fabricated a bioinspired synthetic fish skin for the protection of the soft materials shown in Fig. 6.8. They used a low-modulus elastic mesh to hold the rigid and plastic scales, thus mimicking the lightweight fish skin on which the scales can rotate and interact with adjacent scales. Fig. 6.8a and b shows, respectively, the plane and cross-sectional views of the roll-up natural and synthetic fish skin, where the connection, overlapping degree and interaction among the natural and synthetic fish scales can be clearly seen. The synthetic skin was fabricated with 690 scales (Fig. 6.8c). By characterizing the mechanical response of the synthetic fish skin anisotropically, with and without scales, via in-plane deformation (Fig. 6.8d–h), flexure and indentation, some understanding of the skin itself and the interaction between the fish scales on the skin during deformation was developed. For example, in in-plane deformation tests (Fig. 6.8e), the skin showed a relatively soft and strain-stiffening response in the longitudinal direction yet exhibited a higher stiffness with the presence of the scales (Fig. 6.8d). A simple model was established to describe the behavior of such materials with the intent to guide the design of new engineering scaled skins (Fig. 6.8g and h).

Browning et al. [141] also developed micromechanical models of overlapped fish scales which were employed to measure the mechanical response to blunt and penetrating indentation loading. Due to the mineral contents and hierarchical structures of

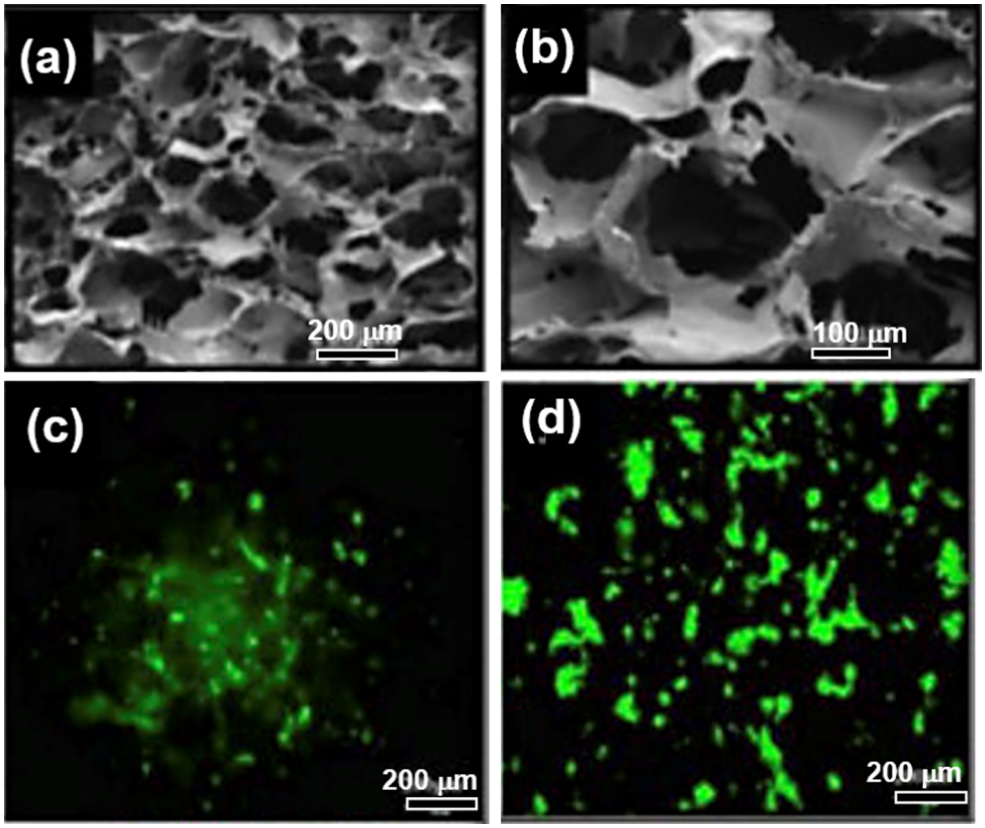

Fig. 6.6. (a and b) SEM micrographs at two magnifications of a scaffold prepared from fish skin collagen and alginate; (c) florescence microscopy image of scaffold after 1-day exposure to cell proliferation in culture; (d) same after 7 days. Notice: green fluorescence from cells (Adapted from Chandika et al. [138]).

different fish scales, they exhibit various flexibilities themselves; however, Nature tunes the arrangement of fish scales including the aspect ratio and degree of imbrication according to the flexible level of a single scale to provide protective functions. The overlapping scales distribute the stresses across a large volume of material and provide penetration resistance.

In light of this, Rudykh et al. [142] fabricated a composite with layered stiff plates and soft matrix by using a multi-material 3-D printer and aligned the plates with different angles (the series with angles of 10°, 20°, 30°, 45°) to the surface in the matrix, in a way to mimic the overlap of the fish scales on the fish (Fig. 6.9). By performing three-point bend tests on the series of the biomimetic overlapped plates, these authors researchers were able to show how the scales and the matrix combine to resist failure through deformation mechanisms of matrix shearing and plate bending. The inter-plate matrix shearing mainly occurred for low indentation depths, especially at large inclination angles (*i.e.*, 30–45°), while the localized plate bending mechanism was more important at small inclinations of penetration (*e.g.*, at 10–20°). They confirmed that mechanisms of matrix shearing led to a lower resistance to failure than mechanisms dominated by plate bending, and further claimed that this represented a new metric for materials performance by incorporating the conflicting properties of penetration resistance and flexibility. However, Nature has long appreciated that careful selection of the materials for the scales and the matrix, with suitable graded interfaces, can provide designs optimized for protection against the penetration as well as preserving flexibility.

7. Conclusions

Nature has developed a vast suite of biological systems with widely different functionalities which are now the basis of scientific endeavor in the search for innovative designs and strategies for new and advanced engineering material systems. In this paper, we have reviewed biological collagenous materials, including skin, bone, arteries, tendon and fish scales, by illustrating their architectures and mechanical response, including stiffness, deformation and toughening mechanisms, across multiple length-scales; we have also briefly discussed how these natural systems have become the basis for bioinspired synthetic materials, such as artificial skin. In the examples described in this work, one consistent and recurrent design motif is that these natural materials often comprise a hard external layer (to resist penetration or wear) with a tougher, more ductile internal base (to adsorb the excess deformation), which is achieved by varying the proportion of soft phase, *e.g.*, collagen, *vs.* hard phase, *e.g.*, HAP mineral. The variants of these multi-

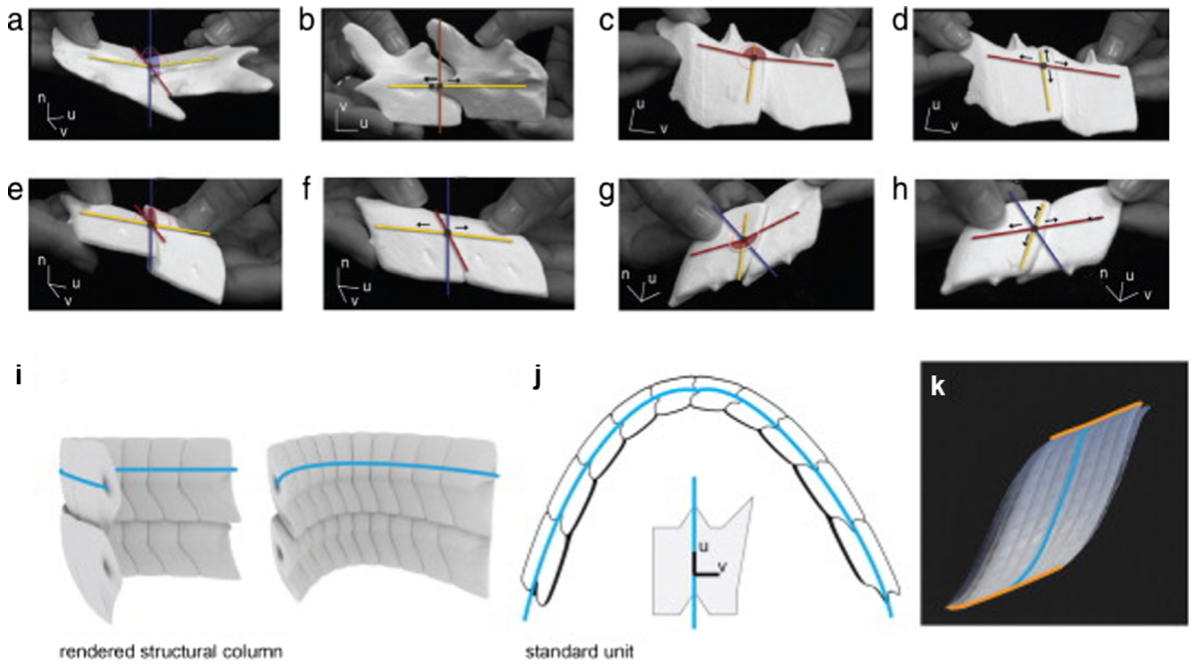

Fig. 6.7. Synthetic biomimetic scales inspired by ganoid fish scale. Scales inspired by *P. senegalus* and the connection and allowable motions between adjacent biomimetic scales. The movement of the adjacent scales includes (a) rotation around the *u*-axis, (b) translation along the *u*-axis, (c) rotation around the *n*-axis, and (d) translation along the *v*-axis. Tail region scales: (e) rotation around the *u*-axis, (f) translation along the *u*-axis, (g) rotation around the *n*-axis and (h) translation along the *v*-axis. (i) The scales can be organized in a 3-D arrangement within two overlapping rings. (j) Schematic drawing shows how the scales join and interlock with each other to form the curved and connected curvature, (k) 3-D printed joined scales forming a large mimicked piece which fits the curvature of the fish [139].

level architectural designs, as well as the salient deformation and toughening mechanisms, are seldom exactly the same in the myriad of biological systems, which provides a continuous source of biomimetic opportunities for the development of new bioinspired materials. Features are pervasive, however; several are listed below:

1. By varying the mineral content in the formation of various nano- to micro-scale structural entities, such as collagen fibers, osteons, pores and tubules, collagenous materials are designed to utilize numerous multiscale mechanisms to develop specific combinations of mechanical properties tailored to their prevailing target functions. These mechanisms include adaptive reorientations, stretching, sliding and rotation of fibrils and fibers at nano- to micro-scale dimensions, by breaking and reforming bonds, all processes that act to promote inelasticity and ductility.
2. Based on the specific hierarchical architectures of collagenous materials at micro and macro length-scales, the collagen fibers/fibrils can be arranged to form different structures with differing mineral contents to achieve either stiffness, strength, ductility, toughness or combinations of these mechanical properties. These structures can display a required mechanical performance with resistance to failure from the development of inelasticity and intrinsic toughening mechanisms, *e.g.*, through fibrillar sliding, straightening and rotation (to carry increased loads), and fibrous or layered separation, and also by corresponding extrinsic toughening mechanisms to “shield” incipient cracks from the applied loading through such mechanisms as constrained microcracking, crack deflection and crack bridging.
3. Collagen is an important biomaterial which is employed in skin grafting, wound healing, tooth repair, wound care and repair, artificial blood vessels, bone substitute, dermal filler, and stent coating. It is currently obtained from organisms, but in the future synthetic collagen will inevitably be developed.
4. There have been few successes in the form of bioinspired structural materials to date, but certainly one exception has been the development of lightweight armor based on the Nature’s design of fish scales. At the macro structural length-scale, fish scales use overlapping mechanisms to protect the fish body yet retain flexibility, with hard outer and tough inner layers. These natural concepts have been successfully modeled and duplicated in artificial materials. However, if the complete suite of mechanisms and functions of the collagenous material could ever be mimicked at multiple length-scales from near atomistic to near macro-scale dimensions in a synthetic material, it may well lead to new lightweight, tear- and fracture-resistant materials with unprecedented mechanical performance.

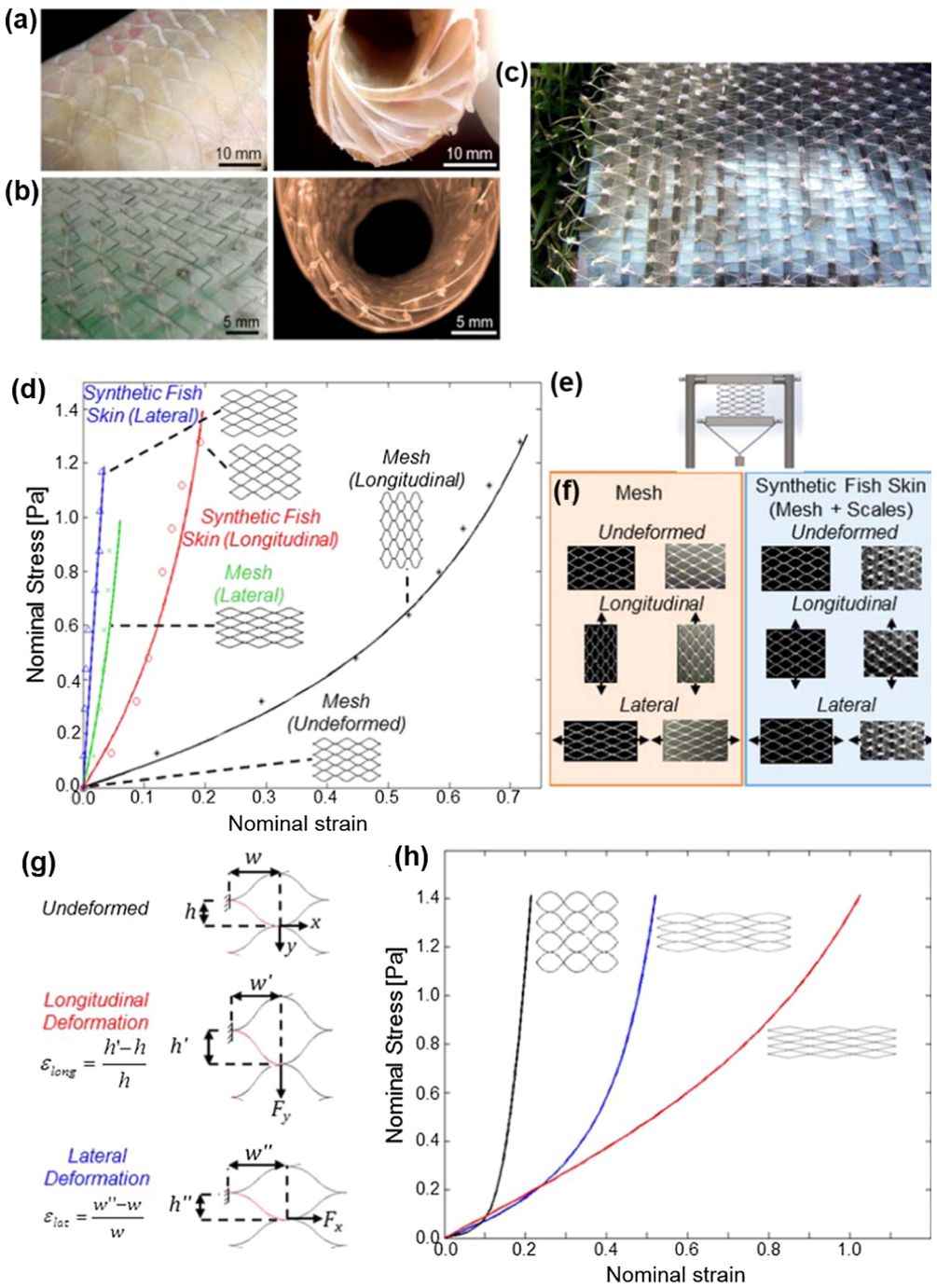

Fig. 6.8. Synthetic fish skin inspired by mullet fish (a–c) and its mechanical response for in-plane deformation (d–h). (a) Striped red mullet (*Mullus surmuletus*) skin and (b) a bioinspired material, modeled after this skin, when undeformed (left) and undergoing flexure (right). (c) The bioinspired fish skin specimen was fabricated in the form of 690 scales and covered an area of ~26,000 mm^2. (d) Experimental (discrete data points) and theoretical (solid curves) of the tensile stress-strain response of the synthetic fish skin and components. The bioinspired fish skin under lateral and longitudinal tension is colored blue and red, respectively, while the lateral and longitudinal response of the mesh only is colored green and black, respectively. (e) Experimental tension setup. (f) Model predictions (images at left) compared to experimental observation (photographs at right) of the elastic mesh under tension for the mesh only and the synthetic fish skin (mesh and scales). (g) Free-body diagram used to model the tensile deformation of the elastic mesh. Because of the periodic configuration of the mesh, responses were calculated for a unit cell as shown in red and then tiled appropriately. (h) Predictions for the longitudinal (horizontal in the figure) stress-strain responses of meshes with different geometries (initial, undeformed geometries shown in the insets) [140].

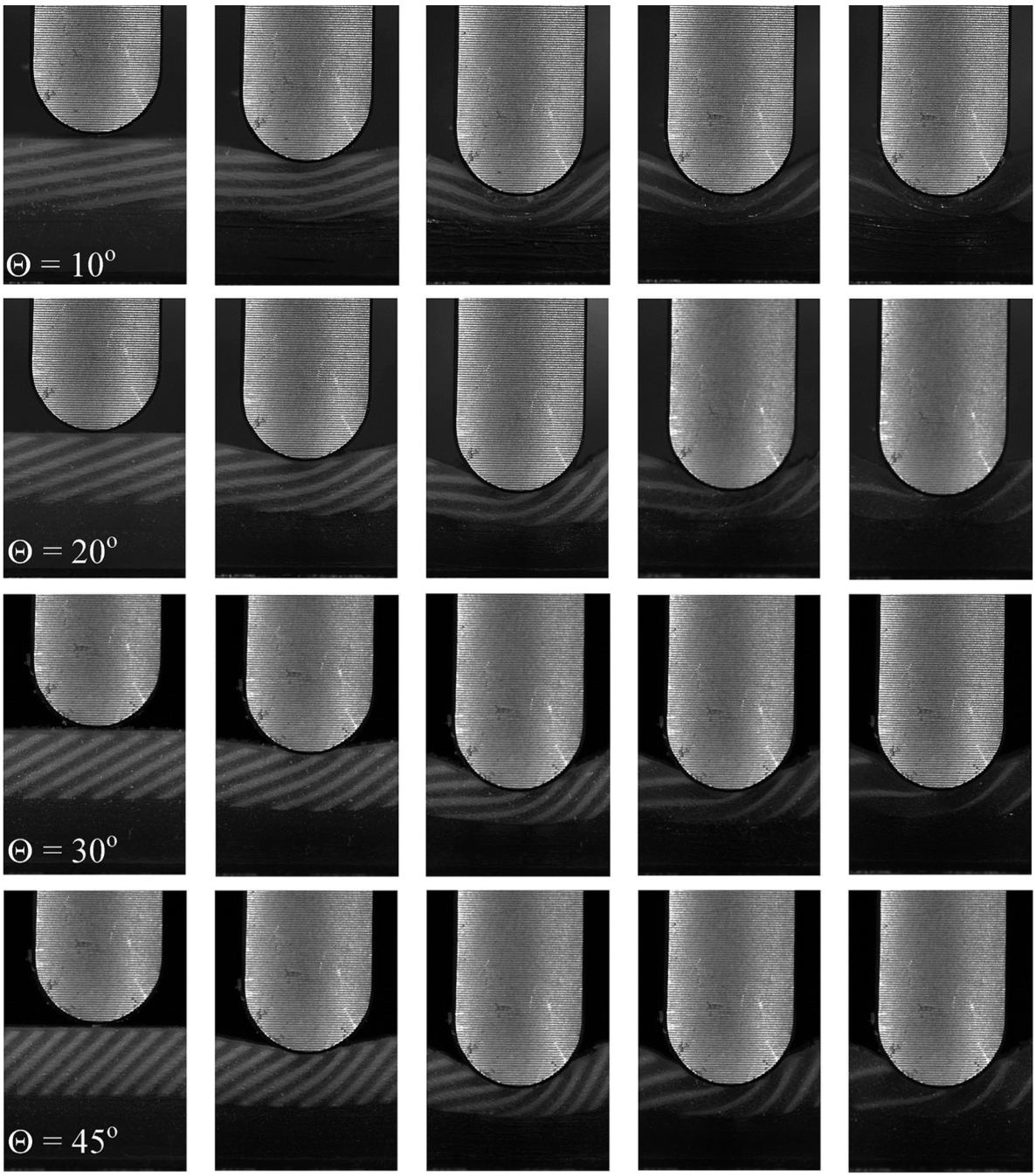

Fig. 6.9. Penetration of a composite comprised of bioinspired fish scales; showing deformation of a soft matrix and stiff plates at different angles to the surface by an indenter with a semi-spherical extremity simulating a tooth. The angles are 10°, 20°, 30°, and 45° in rows (1) to (4) – from top to bottom, respectively [142].

Acknowledgments

This work was supported by the Multi-University Research Initiative under grant no. AFOSR-FA9550-15-1-0009 from the Air Force Office of Scientific Research to the University of California Riverside, specifically through subcontracts to the University of California at San Diego and at Berkeley. W.Y. sincerely acknowledges ETH internal funding from Andre Studart Group.

Competing interests statement

The authors declare that they have no competing interests.

References

[1] Dyer DE, Dunn JA, Thorpe SR, Bailie KE, Lyons TJ, McCance DR, et al. Accumulation of Maillard reaction products in skin collagen in diabetes and aging. J Clin Invest 1993;91(6):2463–9.
[2] Shergold OA, Fleck NA. Mechanisms of deep penetration of soft solids, with application to the injection and wounding of skin. Proc Roy Soc Lond A: Math Phys Eng Sci 2004;460(2050):3037–58.
[3] Yang W, Sherman VR, Gludovatz B, Schaible E, Stewart P, Ritchie RO, et al. On the tear resistance of skin. Nat Commun 2015;27(6):6649.
[4] Sherman VR, Tang Y, Zhao S, Yang W, Meyers MA. Structural characterization and viscoelastic constitutive modeling of skin. Acta Biomater 2017;53:460–9.
[5] Sasaki N, Odajima S. Elongation mechanism of collagen fibrils and force-strain relations of tendon at each level of structural hierarchy. J Biomech 1996;29(9):1131–6.
[6] Silver FH, Freeman JW, Seehra GP. Collagen self-assembly and the development of tendon mechanical properties. J Biomech 2003;36(10):1529–53.
[7] Basser PJ, Schneiderman R, Bank RA, Wachtel E, Maroudas A. Mechanical properties of the collagen network in human articular cartilage as measured by osmotic stress technique. Arch Biochem Biophys 1998;351(2):207–19.
[8] Kääb MJ, Ito K, Rahn B, Clark JM, Nötzli HP. Effect of mechanical load on articular cartilage collagen structure: a scanning electron-microscopic study. Cells Tissues Organs 2000;167(2–3):106–20.
[9] Rho JY, Kuhn-Spearing L, Zioupos P. Mechanical properties and the hierarchical structure of bone. Med Eng Phys 1998;20(2):92–102.
[10] Fratzl P, Gupta HS, Paschalis EP, Roschger P. Structure and mechanical quality of the collagen–mineral nano-composite in bone. J Mater Chem 2004;14(14):2115–23.
[11] Ritchie RO, Buehler MJ, Hansma P. Plasticity and toughness in bone. Phys Today 2009;62(6):41–7.
[12] Ikoma T, Kobayashi H, Tanaka J, Walsh D, Mann S. Physical properties of type I collagen extracted from fish scales of Pagrus major and Oreochromis niloticas. Int J Biol Macromol 2003;32(3):199–204.
[13] Bruet BJ, Song J, Boyce MC, Ortiz C. Materials design principles of ancient fish armour. Nat Mater 2008;7(9):748–56.
[14] Yang W, Gludovatz B, Zimmermann EA, Bale HA, Ritchie RO, Meyers MA. Structure and fracture resistance of alligator gar (Atractosteus spatula) armored fish scales. Acta Biomater 2013;9(4):5876–89.
[15] Yang W, Sherman VR, Gludovatz B, Mackey M, Zimmermann EA, Chang EH, et al. Protective role of Arapaima gigas fish scales: structure and mechanical behavior. Acta Biomater 2014;10(8):3599–614.
[16] Rubin MA, Jasiuk I, Taylor J, Rubin J, Ganey T, Apkarian RP. TEM analysis of the nanostructure of normal and osteoporotic human trabecular bone. Bone 2003;33(3):270–82.
[17] Nair AK, Gautieri A, Chang S-W, Buehler MJ. Molecular mechanics of mineralized collagen fibrils in bone. Nat Commun 2013;4:1724.
[18] Launey ME, Buehler MJ, Ritchie RO. On the mechanistic origins of toughness in bone. Ann Rev Mater Res 2010;40:25–53.
[19] Kadler KE, Holmes DF, Trotter JA, Chapman JA. Collagen fibril formation. Biochem J 1996;316(1):1–11.
[20] Parry DA. The molecular fibrillar structure of collagen and its relationship to the mechanical properties of connective tissue. Biophys Chem 1988;29(1):195–209.
[21] Gautieri A, Buehler MJ, Redaelli A. Deformation rate controls elasticity and unfolding pathway of single tropocollagen molecules. J Mech Behav Biomed Mater 2009;2(2):130–7.
[22] Alexander B, Daulton TL, Genin GM, Lipner J, Pasteris JD, Wopenka B, et al. The nanometre-scale physiology of bone: Steric modelling and scanning transmission electron microscopy of collagen–mineral structure. J R Soc Interface 2012;9(73):1774–86.
[23] Orgel JP, Irving TC, Miller A, Wess TJ. Microfibrillar structure of type I collagen *in situ*. Proc Natl Acad Sci 2006;103(24):9001–5.
[24] Nudelman F, Pieterse K, George A, Bomans PH, Friedrich H, Brylka LJ, et al. The role of collagen in bone apatite formation in the presence of hydroxyapatite nucleation inhibitors. Nat Mater 2010;9(12):1004–9.
[25] Gao H. Application of fracture mechanics concepts to hierarchical biomechanics of bone and bone-like materials. Int J Fract 2006;138(1–4):101.
[26] Gupta HS, Seto J, Wagermaier W, Zaslansky P, Boesecke P, Fratzl P. Cooperative deformation of mineral and collagen in bone at the nanoscale. Proc Natl Acad Sci 2006;103(47):17741–6.
[27] Scott JE, Thomlinson AM. The structure of interfibrillar proteoglycan bridges ('shape modules') in extracellular matrix of fibrous connective tissues and their stability in various chemical environments. J Anat 1998;192(03):391–405.
[28] Buehler MJ, Keten S, Ackbarow T. Theoretical and computational hierarchical nanomechanics of protein materials: deformation and fracture. Prog Mater Sci 2008;53(8):1101–241.
[29] Sherman VR, Yang W, Meyers MA. The materials science of collagen. J Mech Behav Biomed Mater 2015;31(52):22–50.
[30] Diamant J, Keller A, Baer EL, Litt M, Arridge RG. Collagen; ultrastructure and its relation to mechanical properties as a function of ageing. Proc Roy Soc Lond B: Biol Sci 1972;180(1060):293–315.
[31] Markenscoff X, Yannas IV. On the stress-strain relation for skin. J Biomech 1979;12(2):127–9.
[32] Comninou M, Yannas IV. Dependence of stress-strain nonlinearity of connective tissues on the geometry of collagen fibres. J Biomech 1976;9(7):427–33. (27(01): 100–112).
[33] Lanir Y. Structure-strength relations in mammalian tendon. Biophys J 1978 Nov 1;24(2):541–54.
[34] Jenkins JT. A mechanical model for mammalian tendon. J Appl Mech 1975;42(4):755–8.
[35] Freed AD, Doehring TC. Elastic model for crimped collagen fibrils. J Biomech Eng 2005;127(4):587–93.
[36] Kastelic J, Palley I, Baer E. A structural mechanical model for tendon crimping. J Biomech 1980;13(10):887–93.
[37] Meyers MA, Chen PY. Biological materials science: biological materials, bioinspired materials, and biomaterials. Cambridge University Press; 2014.
[38] Yang L, van der Werf KO, Dijkstra PJ, Feijen J, Bennink ML. Micromechanical analysis of native and cross-linked collagen type I fibrils supports the existence of microfibrils. J Mech Beh Biomed Mater 2012;6:148–58.
[39] Eppell S, Smith B, Kahn H, Ballarini R. Nano measurements with micro-devices: mechanical properties of hydrated collagen fibrils. J R Soc Interface 2006;3(6):117–21.
[40] Rigozzi S, Stemmer A, Müller R, Snedeker JG. Mechanical response of individual collagen fibrils in loaded tendon as measured by atomic force microscopy. J Struct Biol 2011;176(1):9–15.
[41] Yang L. Mechanical properties of collagen fibrils and elastic fibers explored by AFM PhD. thesis Enschede (The Netherlands): University of Twente; 2008.
[42] van der Rijt JAJ, van der Werf KO, Bennink ML, Dijkstra PJ, Feijen J. Micromechanical testing of individual collagen fibrils. Macromol Biosci 2006;6(9):697–702.
[43] Buehler MJ. Molecular nanomechanics of nascent bone: fibrillar toughening by mineralization. Nanotechnology 2007;18(29):295102.
[44] Sasaki N, Odajima S. Stress-strain curve and Young's modulus of a collagen molecule as determined by the X-ray diffraction technique. J Biomech 1996;29(5):655–8.
[45] Holzapfel GA, Gasser TC, Ogden RW. A new constitutive framework for arterial wall mechanics and a comparative study of material models. J Elast Phys Sci Sol 2000;61(1–3):1–48.
[46] Holzapfel GA. Collagen in arterial walls: biomechanical aspects. Collagen. Boston (MA): Springer; 2008. p. 285–324.

[47] Meek KM. The cornea and sclera. Collagen. Boston (MA): Springer; 2008. p. 359–96.
[48] Meek KM, Knupp C. Corneal structure and transparency. Prog Ret Eye Res 2015;1(49):1–6.
[49] Komai Y, Ushiki T. The three-dimensional organization of collagen fibrils in the human cornea and sclera. Invest Ophthalmol Vis Sci 1991;32(8):2244–58.
[50] Hassell JR, Birk DE. The molecular basis of corneal transparency. Exp Eye Res 2010;91(3):326–35.
[51] Jablonski NG. Skin: a natural history. Univ of California Press; 2013.
[52] Thorpe CT, Spiesz EM, Chaudhry S, Screen HRC, Clegg PD. Equine Vet J 2015;47:137–40.
[53] Thorpe CT, Birch HL, Clegg PD, Screen HR. The role of the non-collagenous matrix in tendon function. Int J Exp Pathol 2013;94:248–59.
[54] Thorpe CT, Udeze CP, Birch HL, Clegg PD, Screen HRC. Specialization of tendon mechanical properties results from interfascicular differences. J R Soc Interface 2012;9:3108–17.
[55] Martini FH. Fundamentals of anatomy and physiology. 6th ed. New Jersey (USA): Prentice Hall; 2004. p. 182–207.
[56] Shadwick RE, Russell AP, Lauff RF. The structure and mechanical design of rhinoceros dermal armour. Philosoph Trans Roy Soc Lond B: Biol Sci 1992;337(1282):419–28.
[57] Schwinger G, Zanger K, Greven H. Structural and mechanical aspects of the skin of Bufo marinus (Anura, Amphibia). Tissue Cell 2001;33(5):541–7.
[58] Rigby BJ, Hirai N, Spikes JD, Eyring H. The mechanical properties of rat tail tendon. J Gen Physiol 1959;43(2):265–83.
[59] Starborg T, Kalson NS, Lu Y, Mironov A, Cootes TF, Holmes DF, et al. Using transmission electron microscopy and 3-D View to determine collagen fibril size and three-dimensional organization. Nat Protoc 2013;8(7):1433–48.
[60] Provenzano PP, Vanderby R. Collagen fibril morphology and organization: implications for force transmission in ligament and tendon. Matrix Biol 2006;25(2):71–84.
[61] Gupta HS, Messmer P, Roschger P, Bernstorff S, Klaushofer K, Fratzl P. Synchrotron diffraction study of deformation mechanisms in mineralized tendon. Phys Rev Lett 2004;93(15):158101.
[62] Weiss JA, Gardiner JC. Computational modeling of ligament mechanics. Crit Rev Biomed Eng 2001;29(3):303–71.
[63] Amiel D, Frank C, Harwood F, Fronek J, Akeson W. Tendons and ligaments: A morphological and biochemical comparison. J Orthop Res 1983;1(3):257–65.
[64] Hall SJ. Basic biomechanics. Boston (MA): McGraw-Hill; 2007.
[65] Chen PY, Toroian D, Price PA, McKittrick J. Minerals form a continuum phase in mature cancellous bone. Calcif Tissue Int 2011;88(5):351–61.
[66] Clark GL, Parker EA, Schaad JA, Warren WJ. New measurements of previously unknown large interplanar spacings in natural materials. J Am Chem Soc 1935;57(8). 1509–1509.
[67] Weiner S, Price PA. Disaggregation of bone into crystals. Calcif Tissue Int 1986;39(6):365–75.
[68] Schwarcz HP, McNally EA, Botton GA. Dark-field transmission electron microscopy of cortical bone reveals details of extrafibrillar crystals. J Struct Biol 2014;188(3):240–8.
[69] Landis WJ, Song MJ, Leith A, McEwen L, McEwen BF. Mineral and organic matrix interaction in normally calcifying tendon visualized in three dimensions by high-voltage electron microscopic tomography and graphic image reconstruction. J Struct Biol 1993;110(1):39–54.
[70] McNally E, Nan F, Botton GA, Schwarcz HP. Scanning transmission electron microscopic tomography of cortical bone using Z-contrast imaging. Micron 2013;1(49):46–53.
[71] Reznikov N, Bilton M, Lari L, Stevens MM, Kröger R. Fractal-like hierarchical organization of bone begins at the nanoscale. Science 2018;360(6388):eaao2189.
[72] Koester KJ, Ager JW, Ritchie RO. The true toughness of human cortical bone measured with realistically short cracks. Nat Mater 2008;7(8):672–7.
[73] Yang W, Chen IH, Gludovatz B, Zimmermann EA, Ritchie RO, Meyers MA. Natural flexible dermal armor. Adv Mater 2013;25(1):31–48.
[74] Chen PY, Schirer J, Simpson A, Nay R, Lin YS, Yang W, et al. Predation versus protection: fish teeth and scales evaluated by nanoindentation. J Mater Res 2012;27(1):100–12.
[75] Zimmermann EA, Gludovatz B, Schaible E, Dave NK, Yang W, Meyers MA, et al. Mechanical adaptability of the Bouligand-type structure in natural dermal armour. Nat Commun 2013 Oct;15(4):2634.
[76] Bouligand Y. Sur une architecture torsadée répandue dans de nombreuses cuticules d'Arthropodes. C R Acad Sci 1965;261:3665–8.
[77] Giraud MM, Castanet J, Meunier FJ, Bouligand Y. The fibrous structure of coelacanth scales: a twisted 'plywood'. Tissue Cell 1978 Jan 1;10(4):671–86.
[78] Quan H, Yang W, Schaible E, Ritchie RO, Meyers MA. Novel defense mechanisms in the armor of the scales of the "living fossil" Coelacanth fish. Adv Funct Mater 2018;28:1804237.
[79] Crowninshield RD, Pope MH. The response of compact bone in tension at various strain rates. Ann Biomed Eng 1974;2(2):217–25.
[80] Carter DR, Schwab GH, Spengler DM. Tensile fracture of cancellous bone. Acta Orthop Scand 1980;51(1–6):733–41.
[81] Bowman SM, Zeind J, Gibson LJ, Hayes WC, McMahon TA. The tensile behavior of demineralized bovine cortical bone. J Biomech 1996;29(11):1497–501.
[82] Schmid F, Sommer G, Rappolt M, Schulze-Bauer CA, Regitnig P, Holzapfel GA, et al. In situ tensile testing of human aortas by time-resolved small-angle X-ray scattering. J Synchrotron Radiat 2005;12(6):727–33.
[83] Gasser TC, Ogden RW, Holzapfel GA. Hyperelastic modelling of arterial layers with distributed collagen fibre orientations. J R Soc Interface 2006;3(6):15–35.
[84] Agna JW, Knowles Jr. HC, Alverson G. The mineral content of normal human bone. J Clin Investig 1958 Oct;37(10):1357.
[85] Wright TM, Hayes WC. Fracture mechanics parameters for compact bone—effects of density and specimen thickness. J Biomech 1977;10(7):419–30.
[86] Bonfield W, Grynpas MD, Young RJ. Crack velocity and the fracture of bone. J Biomech 1978;11(10–12):473–9.
[87] Behiri JC, Bonfield W. Crack velocity dependence of longitudinal fracture in bone. J Mater Sci 1980;15(7):1841–9.
[88] Behiri JC, Bonfield W. Fracture mechanics of bone—the effects of density, specimen thickness and crack velocity on longitudinal fracture. J Biomech 1984;17(1):25–34.
[89] Behiri JC, Bonfield W. Orientation dependence of the fracture mechanics of cortical bone. J Biomech 1989;22(8–9):863869–7872.
[90] Norman TL, Vashishth D, Burr DB. Mode I fracture toughness of human bone. Adv Bioeng 1991;20:361–4.
[91] Ritchie RO, Koester KJ, Ionova S, Yao W, Lane NE, Ager JW. Measurement of the toughness of bone: a tutorial with special reference to small animal studies. Bone 2008;43(5):798–812.
[92] Mack RW. Bone a natural two-phase material Tech Mem Biomech Lab Berkeley: University of California; 1964.
[93] Sweeney AW, Byers RK, Kroon RP. Mechanical characteristics of bone and its constituents. Mech Eng 1965;87(12):62.
[94] Burstein AH, Zika JM, Heiple KG, Klein LE. Contribution of collagen and mineral to the elastic-plastic properties of bone. J Bone Joint Surg Am. 1975;57(7):956–61.
[95] Wright TM, Vosburgh F, Burstein AH. Permanent deformation of compact bone monitored by acoustic emission. J Biomech 1981;14(6):405–9.
[96] Zhu D, Ortega CF, Motamedi R, Szewciw L, Vernerey F, Barthelat F. Structure and mechanical performance of a "modern" fish scale. Adv Eng Mater 2012;14(4):B185–94.
[97] Dastjerdi AK, Barthelat F. Teleost fish scales amongst the toughest collagenous materials. J Mech Behav Biomed Mater 2015;31(52):95–107.
[98] Nalla RK, Kinney JH, Ritchie RO. Effect of orientation on the *in vitro* fracture toughness of dentin: the role of toughening mechanisms. Biomaterials 2003;24(22):3955–68.
[99] Vashishth D. Rising crack-growth-resistance behavior in cortical bone: implications for toughness measurements. J Biomech 2004;37(6):943–6.
[100] Kendall K. Thin-film peeling-the elastic term. J Phys D Appl Phys 1975;8(13):1449.
[101] Murcia S, McConville M, Li G, Ossa A, Arola D. Temperature effects on the fracture resistance of scales from Cyprinus carpio. Acta Biomater 2015;1(14):154–63.
[102] Haut RC. The effects of orientation and location on the strength of dorsal rat skin in high and low speed tensile failure experiments. J Biomech Eng 1989;111(2):136–40.
[103] Annaidh AN, Bruyère K, Destrade M, Gilchrist MD, Otténio M. Characterization of the anisotropic mechanical properties of excised human skin. J Mech Behav Biomed Mater 2012;5(1):139–48.
[104] Kennedy JC, Hawkins RJ, Willis RB. Danylchuck KD. Tension studies of human knee ligaments. Yield point, ultimate failure, and disruption of the cruciate and tibial collateral ligaments. J Bone Joint Surg Am Vol 1976;58(3):350–5.

[105] Szewciw L, Barthelat F. Mechanical properties of striped bass fish skin: Evidence of an exotendon function of the stratum compactum. J Mech Behav Biomed Mater 2017;1(73):28–37.
[106] Sherman VR, Quan H, Yang W, Ritchie RO, Meyers MA. A comparative study of piscine defense: the scales of Arapaima gigas, Latimeria chalumnae and Atractosteus spatula. J Mech Behav Biomed Mater 2017;1(73):1–6.
[107] Liu P, Zhu D, Wang J, Bui TQ. Structure, mechanical behavior and puncture resistance of grass carp scales. J Bionic Eng 2017;14(2):356–68.
[108] Ritchie RO. The conflicts between strength and toughness. Nat Mater 2011;10(11):817–22.
[109] Liu ZQ, Meyers MA, Zhang Z, Ritchie RO. Functional gradients and heterogeneities in biological materials: design principles, functions, and bioinspired applications. Prog Mater Sci 2017;88:467–98.
[110] Reilly DT, Burstein AH. The elastic and ultimate properties of compact bone tissue. J Biomech 1975;8(6). 393IN9397-6IN11405.
[111] Han L, Wang L, Song J, Boyce MC, Ortiz C. Direct quantification of the mechanical anisotropy and fracture of an individual exoskeleton layer via uniaxial compression of micropillars. Nano Lett 2011;11(9):3868–74.
[112] Wang L, Song J, Ortiz C, Boyce MC. Anisotropic design of a multilayered biological exoskeleton. J Mater Res 2009;24(12):3477.
[113] Zhu D, Szewciw L, Vernerey F, Barthelat F. Puncture resistance of the scaled skin from striped bass: collective mechanisms and inspiration for new flexible armor designs. J Mech Behav Biomed Mater 2013;31(24):30–40.
[114] Wyckoff RW, Corey RB, Biscoe J. X-ray reflections of long spacing from tendon. Science 1935;82:175–6.
[115] Yannas IV, Burke JF. Design of an artificial skin I. Basic design principles. J Biomed Mater Res 1980;14(1):65–81.
[116] Yannas IV, Burke JF, Gordon PL, Huang C, Rubinstein RH. Design of an artificial skin II: Control of chemical composition. J Biomed Mater Res 1980;14(2):107–31.
[117] Yannas IV. Use of artificial skin in wound management. In: Dineeneditor. The surgical wound. 1981. p. 170–91.
[118] Yannas IV, Burke JF, Warpehoski M, Stasikelis P, Skrabut EM, Orgill D, et al. Prompt, long-term functional replacement of skin. Trans Am Soc Artif Int Org 1981;27:19–22.
[119] Yannas IV, Burke JF, Orgill D, Skrabut EM. Wound tissue can utilize a polymeric template to synthesize a functional extension of skin. Science 1982;215(4529):174–6.
[120] Yannas IV, Lee E, Skrabut EM, Murphy GF. Synthesis and characterization of a model extracellular matrix which induces partial regeneration of adult mammalian skin. Proc Natl Acad Sci 1989;86(3):933–7.
[121] Burke JF, Yannas IV, Quinby Jr. WC, Bondoc CC, Jung WK. Successful use of a physiologically acceptable artificial skin in the treatment of extensive burn injury. Ann Surg 1981;194(4):413–28.
[122] Heimbach DA, Luterman AR, Burke JO, Cram A, Herndon DA, Hunt JO, et al. Artificial dermis for major burns. A multi-center randomized clinical trial. Ann Surg 1988;208(3):313.
[123] Parenteau-Bareil R, Gauvin R, Berthod F. Collagen-based biomaterials for tissue engineering applications. Materials 2010;3(3):1863–87.
[124] Kotch FW, Raines RT. Self-assembly of synthetic collagen triple helices. Proc Natl Acad Sci 2006;103(9):3028–33.
[125] O'Leary LE, Fallas JA, Bakota EL, Kang MK, Hartgerink JD. Multi-hierarchical self-assembly of a collagen mimetic peptide from triple helix to nanofibre and hydrogel. Nat Chem 2011;3(10):821.
[126] Caliari SR, Weisgerber DW, Ramirez MA, Kelkhoff DO, Harley BA. The influence of collagen–glycosaminoglycan scaffold relative density and microstructural anisotropy on tenocyte bioactivity and transcriptomic stability. J Mech Behav Biomed Mater 2012;1(11):27–40.
[127] Murphy GF, Orgill DP, Yannas IV. Partial dermal regeneration is induced by biodegradable collagen-glycosaminoglycan grafts. Lab Invest 1990;62:305–13.
[128] Dong C, Lv Y. Application of collagen scaffold in tissue engineering: Recent advances and new perspectives. Polymers 2016;8(2):42.
[129] Yu CC, Chang JJ, Lee YH, Lin YC, Wu MH, Yang MC, et al. Electrospun scaffolds composing of alginate, chitosan, collagen and hydroxyapatite for applying in bone tissue engineering. Mater Lett 2013;15(93):133–6.
[130] Fahimipour F, Dashtimoghadam E, Rasoulianboroujeni M, Yazdimamaghani M, Khoshroo K, Tahriri M, et al. Collagenous matrix supported by a 3D-printed scaffold for osteogenic differentiation of dental pulp cells. Dent Mater 2018;34(2):209–20.
[131] Ye X, Zhou Y, Sun Y, Chen J, Wang Z. Structure and infrared emissivity of collagen/SiO_2 composite. Appl Surf Sci 2008;254(18):5975–80.
[132] Heinemann S, Coradin T, Worch H, Wiesmann HP, Hanke T. Possibilities and limitations of preparing silica/collagen/hydroxyapatite composite xerogels as load-bearing biomaterials. Compos Sci Technol 2011;71(16):1873–80.
[133] Lin YC, Tan FJ, Marra KG, Jan SS, Liu DC. Synthesis and characterization of collagen/hyaluronan/chitosan composite sponges for potential biomedical applications. Acta Biomater 2009;5(7):2591–600.
[134] Shin KH, Kim JW, Koh YH, Kim HE. Novel self-assembly-induced 3D plotting for macro/nano-porous collagen scaffolds comprised of nanofibrous collagen filaments. Mater Lett 2015;15(143):265–8.
[135] Deshpande AS, Beniash E. Bioinspired synthesis of mineralized collagen fibrils. Cryst Growth Des 2008;8(8):3084–90.
[136] Ngiam M, Liao S, Patil AJ, Cheng Z, Yang F, Gubler MJ, et al. Fabrication of mineralized polymeric nanofibrous composites for bone graft materials. Tissue Eng Part A 2008;15(3):535–46.
[137] Meghezi S, Drouin B, Mantovani D. Collagen hydrogel-based scaffolds for vascular tissue regeneration: mechanical and viscoelastic characterization. Characterization of polymeric biomaterials. 2017. p. 397–439.
[138] Chandika P, Ko SC, Oh GW, Heo SY, Nguyen VT, Jeon YJ, et al. Fish collagen/alginate/chitooligosaccharides integrated scaffold for skin tissue regeneration application. Int J Biol Macromol 2015;1(81):504–13.
[139] Duro-Royo J, Zolotovsky K, Mogas-Soldevila L, Varshney S, Oxman N, Boyce MC, et al. MetaMesh: A hierarchical computational model for design and fabrication of biomimetic armored surfaces. Comput Aided Des 2015;31(60):14–27.
[140] Funk N, Vera M, Szewciw LJ, Barthelat F, Stoykovich MP, Vernerey FJ. Bioinspired fabrication and characterization of a synthetic fish skin for the protection of soft materials. ACS Appl Mater Interfaces 2015;7(10):5972–83.
[141] Browning A, Ortiz C, Boyce MC. Mechanics of composite elasmoid fish scale assemblies and their bioinspired analogues. J Mech Behav Biomed Mater 2013;31(19):75–86.
[142] Rudykh S, Ortiz C, Boyce MC. Flexibility and protection by design: Imbricated hybrid microstructures of bio-inspired armor. Soft Matter 2015;11(13):2547–54.

Wen Yang is a project scientist in Department of Nanoengineering at the University of California, San Diego, and affiliated with Lawrence Berkeley National Laboratory. She is the managing editor of Materials Science and Engineering C, Elsevier. She received her Ph.D. degree in Materials Physics and Chemistry in Northeastern University in China and continued her postdoctoral research at University of California, San Diego and ETH Zurich, Switzerland (Swiss Federal Institute of Technology in Zurich). Her research focuses on biological and bioinspired materials, specifically on the relationship between structural characterization, mechanical behavior and toughening mechanisms of the materials.

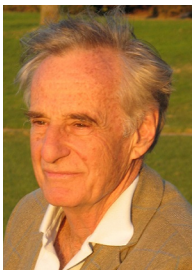

Marc A. Meyers is Distinguished Professor of Materials Science at the University of California, San Diego. His research field is the mechanical behavior of materials. Within this field, he has focused on three areas: dynamic behavior of materials, nanocrystalline materials, and biological materials. In the dynamic behavior of materials, the unifying theme is the high rate at which events occur. He initiated this work in 1972 and has dedicated forty-five uninterrupted years to it, unifying it by emphasizing the fundamental physical and chemical phenomena. This has been defined in his now classic book, Dynamic Behavior of Materials (1994, ~3000 citations in Google scholar). He is the co-author of Mechanical Metallurgy, Mechanical Behavior of Materials, Biological Materials Science (CUP, 2014), and approximately 450 papers. His honors include Fellow, TMS, APS, ASM, and Explorers Club as well as awards in the US (APS Duvall, ASM Albert White and Sauveur, TMS Mehl, Cohen and Educator, Acta Materialia Materials and Society, SMD/TMS Distinguished Engineer/Scientist and Service), Europe (Humboldt, DGM Heyn, and DYMAT Rinehart), and China (Lee Hsun). He was co-founder of the Center for Explosives Technology Research, New Mexico Tech, and of the EXPLOMET conference series (1980–2000), as well as Associate Director and Director of the UCSD Institute for Mechanics and Materials, where he co-organized four summer schools. He co-chaired the first three Pan American Materials Conferences, which he co-founded. He is the author of four fiction books and of River of Doubt, commemorating the Roosevelt-Rondon Scientific Expedition in the Amazon.

Robert O. Ritchie is the Chua Distinguished Professor of Engineering in the Materials Science & Engineering Department at the of Berkeley, and Faculty Senior Scientist at the Lawrence Berkeley National Laboratory. He holds M.A., Ph.D. and Sc.D. degrees in physics/materials science from Cambridge. He is known for his research on the fracture of materials, with current interests focused on bioinspired materials, the degradation of bone, and fracture in multi-component alloys. He is a Fellow of the Royal Society and of the U.K. Royal Academy of Engineering, the U.S. National Academy of Engineering, the Russian Academy of Sciences and the Royal Swedish Academy of Engineering Sciences.